

UC San Diego

UC San Diego Electronic Theses and Dissertations

Title

Planar Josephson junctions and arrays by electron beam lithography and ion damage

Permalink

<https://escholarship.org/uc/item/01f048zn>

Author

Cybart, Shane A.

Publication Date

2005

Peer reviewed|Thesis/dissertation

UNIVERSITY OF CALIFORNIA, SAN DIEGO

Planar Josephson Junctions and Arrays
by Electron Beam Lithography and Ion Damage

A dissertation submitted in partial satisfaction of the
requirements for the degree Doctor of Philosophy
in
Materials Science and Engineering

by

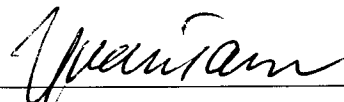
Shane A. Cybart


Committee in charge:


Professor Robert C. Dynes, Chairman
Professor Michael J. Sailor
Professor Yuan Taur
Professor Charles Tu
Professor Edward T. Yu

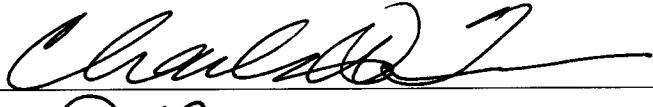
2005

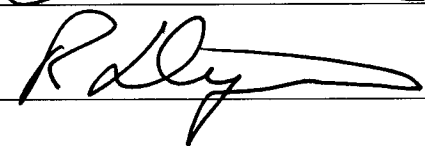
The dissertation of Shane A. Cybart is approved, and
it is acceptable in quality and form for publication on
microfilm:










_____ Chairman

University of California, San Diego

2005

TABLE OF CONTENTS

Signature Page	iii
Table of Contents	iv
List of Figures	vi
Acknowledgements	xii
Vita, Publications, and Fields of Study	xiv
Abstract	xv
1 Introduction	1
2 Background	3
2.1 Historical Background	3
2.2 Coherent Phenomena in Superconductors	3
2.3 Superconductors in Magnetic Fields	5
2.4 Josephson Junctions	7
2.4.1 The RCSJ Model	9
2.4.2 The Effect of an AC Bias on Josephson Junctions	11
2.4.3 The Josephson Penetration Depth	13
2.4.4 The Effect of Magnetic Field on the Supercurrent	15
2.4.5 Proximity Coupling	17
2.4.5.1 Ion Damage SN'S Junctions	18
2.4.5.2 SS'S Junctions	20
2.4.6 Series Arrays of Josephson Junctions	20
2.4.6.1 The Josephson Arbitrary Waveform Generator	21
2.4.7 The DC SQUID	24
2.4.7.1 Superconducting Quantum Interference Filters (SQIF)	25
2.5 Superconducting Materials	26
2.5.1 $\text{YBa}_2\text{Cu}_3\text{O}_{7-\delta}$	27
2.5.2 MgB_2	29
2.5.3 Ion Damage in Superconductors	29
2.5.3.1 Ion Damage in $\text{YBa}_2\text{Cu}_3\text{O}_{7-\delta}$	30
2.5.3.2 Ion Damage in MgB_2	31
3 Device Fabrication	32
3.1 HTS Thin Films	32
3.1.1 HTS Substrates	32
3.1.2 Growth of HTS Materials by Laser Ablation	34
3.1.3 Thermal Co-Evaporated HTS Thin Films	37

3.1.3.1	Film Morphology	39
3.1.3.2	Electrical Transport Properties	41
3.2	MgB ₂ Thin Films Grown by HPCVD	44
3.3	Mask Design	46
3.4	Pattern Photolithography	47
3.5	Argon Ion Milling	47
3.6	Lift-off and Gold Removal	48
3.7	Tri-layer Structure	50
3.8	Electron Beam Lithography	51
3.9	Reactive Ion Etching	56
3.10	Ion Damage	58
3.10.1	Simulations	60
3.11	Electron Beam Proximity Effect	62
4	Measurements	67
4.1	Resistance vs. Temperature	71
4.2	Current-Voltage Characteristics	72
4.3	Differential Resistance	73
4.4	Modulation of the Critical Current in Magnetic Field	74
4.5	Shapiro Step Amplitude Dependence	75
4.6	Temperature Dependence of the Critical Current	75
5	YBa ₂ Cu ₃ O _{7-δ} Josephson Junctions	76
5.1	Single Junctions	76
5.2	Junction Pairs	87
5.3	Series Arrays of Junctions	91
6	MgB ₂ Josephson Junctions	99
7	DC Washer SQUID	103
8	Conclusion	106
	Bibliography	108

LIST OF FIGURES

2.1	Schematic diagram of a Josephson junction. The order parameters from the superconducting electrodes decay into the barrier and couple the wavefunctions together.	8
2.2	Equivalent circuit for a Josephson junction used in the RCSJ model.	9
2.3	$I - V$ characteristic for a non-hysteretic Josephson junction with small capacitance.	11
2.4	Shapiro steps in the $I - V$ characteristic for a non-hysteretic Josephson junction simultaneously biased with both ac and dc current . .	11
2.5	Shapiro step amplitude dependence as a function of ac bias.	12
2.6	3-dimensional representation of a Josephson junction. The current flow is along the x -axis, and the width of the barrier lies along the y -axis.	13
2.7	Two dimensional cross-section showing the current density in a long (a) and short (b) Josephson junction. Current in the electrodes is carried on the edges and penetrates a distance of λ_L into the interior. Inside of the barrier this screening length is λ_J	14
2.8	Critical current as a function of magnetic flux for a rectangular junction.	16
2.9	Spatial distribution of the supercurrent in a Josephson junction for different values of magnetic flux. One can see that at the minima in the sinc function in Figure 2.8 (integer values of Φ_0) that there is an equal amount of current in both directions. For half integer values of Φ_0 the net-current flow is in one direction but its magnitude is reduced as more oscillations traverse the junction [20].	17
2.10	Critical current dependencies for 3 ion-damage Josephson junctions of different lengths. The temperature dependant barrier length provides a better fit then the classical de Gennes model with and without “soft” boundary conditions [27].	19
2.11	$I - V$ characteristic for an ion-damaged Josephson junction fit with the RSJ model modified with a current dependant resistance [27]. .	20
2.12	Voltage-current characteristic for a junction array simultaneously ac and dc biased depicting optimum dc bias currents, $\pm I_0$ for selection of the output voltage polarity [30].	22
2.13	Example of dc voltage synthesis using a pulse driven waveform generator. The top curve is the ac bias drive signal, the middle is the binary bit stream and the bottom shows the instantaneous voltage across the junction [30].	22
2.14	2-level binary code used to generate the sine wave S' , the pulses in S_D represent the density of 1's and 0's in the bit stream [30].	23
2.15	Circuit diagram for a dc SQUID.	24

2.16	Modulation of the current-voltage characteristic for a dc SQUID the trace on the left shows how I_c changes with applied flux and the trace underneath shows the voltage modulation or “triangle wave” resulting [20].	24
2.17	Calculated magnetic field response of a serial SQIF [32].	26
2.18	Orthorhombic unit cell for $\text{YBa}_2\text{Cu}_3\text{O}_{7-\delta}$, showing the positions of the different atoms. The cell is usually described as three oxygen deficient perovskite cells stacked on top of each other.	28
2.19	Hexagonal structure of MgB_2	29
2.20	Resistivity as a function of temperature for a single $\text{YBa}_2\text{Cu}_3\text{O}_{7-\delta}$ film after bombardment with 1 MeV Ne^+ ions at fluences of (0, 0.1, 2.5, 4.0, 10.0, 15.0, 20.0, and 22.0) $\times 10^{13}$ ions/cm ² [40].	31
2.21	Resistivity as a function of temperature for a MgB_2 film bombarded with various fluences of 2 MeV alpha particles [41].	31
3.1	Schematic representation of the PLD system used at UCSD.	35
3.2	Orientation of the sample holder (heater) with respect to the plume for conventional (a) and off-axis PLD (b.)	36
3.3	1 μm^2 STM image of a $\text{YBa}_2\text{Cu}_3\text{O}_{7-\delta}$ film grown by PLD. The growth spirals are visible and the height of the terraces correspond to a single unit cell (11.7 Å).	37
3.4	Schematic diagram of the Thewa thermal co-evaporation system for the deposition of YBCO and other RBCO compounds [44].	38
3.5	SEM pictures of the different grades of YBCO films, (a) M-type, (b) S-type, and (c) E-type [44].	40
3.6	(a) AFM image of a 600 nm YBCO film on MgO, (b) average surface roughness of the same film [44].	41
3.7	Cryoscan for a 2” wafer of 100 nm $\text{YBa}_2\text{Cu}_3\text{O}_{7-\delta}/\text{CeO}_2/\text{Al}_2\text{O}_3$, depicting the critical current density in units of MA/cm ² for 5 x 5 mm ² regions.	42
3.8	Resistance vs. temperature measurement of a Thewa co-evaporated 100 nm thick YBCO thin film on CeO_2 buffered r-plane sapphire substrate. The T_c of this film is 86 K and the residual resistivity is 17 $\mu\Omega\text{cm}$ The inset shows the transition width to be about 0.5 K.	43
3.9	Resistance vs. temperature measurement of a Thewa co-evaporated 100 nm thick NdBCO thin film on CeO_2 buffered r-plane sapphire substrate. The T_c of this film is 71 K and the residual resistivity is approximately 300 $\mu\Omega\text{cm}$ The inset shows the transition width to be about 5 K.	43
3.10	SEM pictures of MgB_2 films grown on sapphire (left) and SiC (right), both feature hexagonal growth columns [50].	44
3.11	AFM picture of an MgB_2 films grown on SiC and a surface profile of the same film [50].	45
3.12	Temperature dependence of the resistivity of an MgB_2 film.	45

3.13	Sixteen bridge photolithographic graph mask dark lines(blue) represent the circuit areas and light lines(green) are EBL alignment marks. 16 bridges are located within a $90\ \mu\text{m} \times 90\ \mu\text{m}$ central region of the mask.	46
3.14	(a)Ge film evaporated on top of a lift-off over hang created using a chlorobenzene soak. The film is discontinuous at the resist edge preventing it from being pulled off when the resist is removed. (b) Cross-section showing the extent of the overhang.	49
3.15	Central region of the sixteen bridge photolithographic graph mask dark lines showing the region where the contact was removed via chemical or dry etching.	50
3.16	Cross-section showing the components of the tri-layer implant mask.	50
3.17	Microscope picture showing a cracked tri-layer mask. The circuit pattern is visible underneath the cracked resist/Ge layers.	51
3.18	The effect of 60 Hz environmental noise on lines written with EBL.	52
3.19	Hole burned in the PMMA layer in point scan mode to test and adjust the focus and astigmatism.	55
3.20	Central region of the 16-Bridge mask showing 5 lines (junctions) scribed across each bridge.	56
3.21	Grass after RIE etching of the tri-layer.	58
3.22	Etched tri-layer mask depicting the 7° tilt used to prevent channeling.	59
3.23	Sample holder designed to prevent misalignment. The center of the wafer contains a ramp with a 7° tilt. The lines scribed by EBL are aligned parallel with the ramp and the wafer is implanted at 0°	59
3.24	Implantation simulation of a 400 nm space junction pair. The contour scale is the base ten log of the number of displacements for cm^3	61
3.25	Exposure vs. distance data for single line writing demonstrating the electron beam proximity effect. Distance is measured from the center of the line. The solid line is a double Gaussian fit.	63
3.26	Illustration of the pattern for writing 100 parallel lines and compensation rectangles at each end of the lines (not to scale).	64
3.27	SEM pictures of the 100-line array with 500 nm period. (a), (b), (c) The pictures of the left end, middle, and the right end of the line array of a sample with both compensation rectangles written. (d), (e), (f) The pictures of the corresponding parts of the line array of a sample with only right compensation triangle written.	66
3.28	SEM pictures of the 100-line array with 250 nm period. (a) The middle part, (b) the right end of the line array. A compensation rectangle has been written by the right end.	66
4.1	Top of the cryogenic dip probe built for this dissertation.	68
4.2	Sample and thermometer bonded in a 44 pin J-lead chip carrier.	69

4.3	Flux trapping in a single junction measured at 71.0 K without any magnetic shielding.	70
4.4	Schematic diagram for resistance-temperature measurements.	72
4.5	Schematic diagram for current-voltage measurements.	73
4.6	Schematic diagram for the measurement of differential resistance.	74
5.1	$I-V$ characteristic at 63 K showing a fit with (a) the RSJ model, and (b) the RSJ model with thermal rounding and a current dependant resistance.	77
5.2	$I-V$ characteristics measured for the same junction at five temperatures. From top to bottom : 75.6 K, 76.9 K, 77.8 K, 78.5 K, 79.7 K. The junction's barrier undergoes a transition from weak coupling to strong coupling with decreasing temperature.	78
5.3	Flux-flow $V-I$ characteristics from the same junction in Figure (5.2). The solid lines are fits of the form $V \propto I^n$, where the exponent n is related to vortex motion in the weaklink.	79
5.4	Critical current and normal resistance vs. temperature for the same junction from Figure 5.2. The inset shows the $I_c R_n$ product as a function of temperature. It has a peak where the junction transitions from RSJ-like to strongly coupled.	80
5.5	Six junctions from the same chip. The legend labels the curves from top to bottom. The parameters of J7, J3, J4, and J6 are nearly identical.	81
5.6	Critical current vs. temperature, near T_c the data have a $(1 - T/T_c)^3$ dependance. At lower temperatures it follows a $(1 - T/T_c)^2$ dependance.	81
5.7	Shapiro steps in a junction's $I-V$ characteristics for different applied 10 GHz RF powers, measured at 77.7 K. The y -axis has been offset for clarity.	82
5.8	Bessel-like dependencies of the critical current ($n = 0$), and the first two Shapiro steps. The inset shows the full range of the data.	82
5.9	Fraunhofer pattern demonstrating the dc Josephson effect. The two curves show the hysteresis for sweeps of increasing and decreasing field.	83
5.10	$I-V$ characteristic with and without an applied flux of Φ_0	84
5.11	$I_c R_n$ vs. temperature for the same junction before and after a 2 hour anneal at 100°C.	85
5.12	$I_c R_n$ vs. R_n showing a substantial increase in $I_c R_n$, for constant R_n	86
5.13	$I-V$ characteristics before and after the anneal. The resistance is the same and the critical current is increased by a factor of two. After the anneal the $I-V$ characteristic retains its RSJ-like shape.	86

5.14	The SEM picture of a junction pair after ion damage. A, B, and C denote the photoresist mask, the $\text{YBa}_2\text{Cu}_3\text{O}_{7-\delta}$ bridge, and the sapphire substrate, respectively. (b) Schematic drawing of the junction pair and measurement configuration.	88
5.15	Oscilloscope pictures of the current voltage characteristics of junction 1 (curve A), junction 2 (curve B, and the pair in series (curve C) without (a) and with (b) 12 GHz microwave radiation.	88
5.16	$I-V$ characteristics at 71 K for a 150 nm spaced junction pair with 13 GHz microwave radiation. A and B were measured using the central electrode and C is measured across the pair.	89
5.17	Implantation simulation	90
5.18	SEM picture of an etched tri-layer mask used for creation of a 100 junction array. The slits are 50 nm wide with a spacing of 231.7 nm.	91
5.19	(a) Top view and 47° tilt of a tri-layer mask patterned so that ion damage can reduce the bridges electrical width from 4 to 2 μm	92
5.20	$I-V$ characteristics for 3 different ten junction arrays measured at 78.0 K, 77.3 K and 84.0 K for A, B, and C respectively.	92
5.21	$I-V$ characteristics for 4 temperatures for sample C, fit with a modified RSJ model.	93
5.22	Ten junction array $I-V$ characteristics measured at 77.4 K, with and without 15 GHz microwave radiation (a). Shapiro steps are visible at 0.31 mV, 10 times the voltage expected for a single junction at this frequency. Differential resistance (b) measurements going to zero verify that the steps are vertical, implying all junctions are locked to the 15 GHz signal.	94
5.23	Dependance of the critical current for a ten junction array on microwave power.	95
5.24	Resistance vs. temperature for samples A and C. The electrodes in both films superconduct at 87 K. The reduction in T_c is 6.5 K for the higher dose (sample A) and 1 K for the lower dose (sample C). The inset zooms in on the transition for the lower dose sample.	95
5.25	Critical current modulation in magnetic field for samples A (a) 78.0 K, B (b) 76.0 K, and C (c) 82.9 K.	96
5.26	(a) $I-V$ characteristic for a 50 junction array measured at 71.8 K with and without 20 GHz microwave radiation. (b) Differential resistance measurements do not reach zero due to non-uniform junction parameters.	98
6.1	(a) $I-V$ Characteristics for a single junction measured at 37.2 K, with and without 12 GHz microwave radiation. (b) Microwave power dependance of the critical current and 1st-order Shapiro step.	100

6.2	(a) Single junction critical current(circles)and resistance (triangles) temperature dependencies. The dashed and solid lines are fits with $I_c \propto (T - T_c)^2$ and $I_c \propto (T - T_c)^3$ respectively. (b) The same data shown for a temperature range near T_c	101
6.3	(a) $I - V$ Characteristics for a 20 junction array measured at 37.5 K, with and without 12 GHz microwave radiation. (b) Differential resistance vs. voltage measured under the same radiation.	102
7.1	Mask used to fabricate DC washer SQUIDs. The zoomed region shows the two arms of the SQUID the lines crossing them represent the EBL defined slits in the tri-layer mask to define the junctions. The square in the hole of the washer is an alignment mark which is exposed during EBL and damaged with the junctions so that it does not superconduct.	104
7.2	(a) $I - V$ characteristic of a dc SQUID fabricated from two 10-junction series arrays connected in parallel. (b) Modulation of the voltage at 115 μA in magnetic field.	105

Acknowledgements

I would like to express my thanks and gratitude to Bob Dynes for teaching me how to be a scientist and trusting me with many important project decisions that other students don't get the chance to make. He gave me the opportunity to try my own ideas even if he knew they wouldn't work. His dedication to his lab is unwavering; somehow he always found time for me, despite his busy schedule.

I am grateful to my committee Professors Michael J. Sailor, Yuan Taur, Charles Tu and Edward T. Yu for taking their time to evaluate my work.

I would like to thank Harold Weinstock for funding this project as well as my tuition. He gave me the opportunity to travel around the world to interact with other scientists in my field. I value our conversations about superconductivity and his advice on my career.

There are a lot of people who have helped make this dissertation possible, but first and foremost I would like to thank Postdoctoral Scholar Ke Chen for teaching me the secrets of device processing, measurements, a lot about junctions, and even a little Chinese. His expertise in electron beam lithography was paramount to the success of this project. I also received a lot of help from a truly outstanding cast of undergraduate research assistants: "Diao" Sam Lee and Jenny "Bear" Hsiung helped with device processing and etching and Charles "Chuck C." Cheung and Ed Wu performed work on computer simulations and data analysis.

I am thankful to have had the opportunity to work with many other outstanding scientists during my time as a graduate student:

Dr. Olivier Bourgeois for teaching me thermal evaporation and measurement techniques. Dr. Winfried Teizer for teaching me about EBL and the some good tips on making beer and sausage. Dr. Louisa Bochacheva for helping me with measurements and data analysis. Fellow graduate students Ofer Naamen and Hikari Kimura for helpful discussions. Visiting Professors Judy Wu, Horst Rogalla, Rich Barber and Siu Chan. Collaborators John Talvacchio, Horst Rogalla, and Sam

Benz. Xiaoxing Xi, Qi Li, and Yi Cui from Penn State for providing us with high quality MgB₂ films.

I would also like to thank the following staff members at UCSD:

Cathy Reddicono and Gary Doran for their help in making sure the bills were paid on time. Charlotte Lauve for her help with everything related to the matsci program. Larry Grissom and Ryan Anderson of the Integrated Technologies Laboratory for setting up equipment for me at a moments notice and great advice on device processing. Allen White and George Kassabian of the Physics Electronics Shop for all of the custom electronics used in this work. Don Johnson of the Campus Research Machine Shop for his help on vacuum systems and dip probes. Andy Pommer for teaching me how to use a Lathe and a Bridgeport, UCSD misses him. Paul Redgate and Lester Brooks for building maintenance. Jeff Phillips for keeping my helium Dewars full. Bryan Hill and Lee Davenport for outstanding IT support.

Furthermore I would like to thank Dr. Vaman and Ratna Naik for giving me research experience as an undergrad which helped prepare me for graduate school. Bill and Tiffany Yuhasz, Eric Scroggins, and Chris VandeBerg for being good friends and helping out at a moments notice. Mutsumi Murayama for her support and for keeping me company in the lab on many of my late night quests to obtain data.

My parents and my family for support and encouragement. Especially my sister Kim for visiting often and never letting me feel too far away from home.

And finally my dearest friend Yang Yang Li (Mao Yang) for showing me what life is like on the other side of the world and sharing my fondest memories of graduate school.

VITA

2000	B.S. Physics, University of Michigan-Dearborn
2001	M.S. University of California, San Diego
2005	Ph.D. University of California, San Diego

PUBLICATIONS

- S. A. Cybart, K. Chen, Y. Cui, Qi Li, X. X. Xi, and R. C. Dynes, “**Planar MgB₂ Josephson junctions and series arrays via nanolithography and ion damage**” *Applied Physics Letters*, to be published January, 2006.
- S. A. Cybart, K. Chen, and R. C. Dynes, “**Planar YBa₂Cu₃O_{7- δ} ion damage Josephson junctions and arrays**” *IEEE Transactions on Applied Superconductivity*, **15**, p. 241, June, 2005.
- K. Chen, S. A. Cybart, and R. C. Dynes, “**Fabrication of identical sub-100 nm closely spaced parallel lines using electron beam lithography**” *Journal of Vacuum Science and Technology B.*, **23**, p. 1887, October 2005.
- K. Chen, S. A. Cybart, and R. C. Dynes, “**Study of closely spaced YBa₂Cu₃O_{7- δ} Josephson junction pairs**” *IEEE Transactions on Applied Superconductivity*, **15**, pp. 149, June, 2005.
- K. Chen, S. A. Cybart, and R. C. Dynes, “**Planar YBa₂Cu₃O_{7- δ} Josephson junctions and arrays via nanolithography and ion damage**” *Applied Physics Letters*, **85**, pp. 2853, October, 2004.

FIELDS OF STUDY

- Major Field: Materials Science and Engineering
- Studies in Solid State Electronics.
Professors Yuan Taur and S.S. Lau
 - Studies in Microwave Systems and Circuits.
Dr. Donald Lie
 - Studies in Thermodynamics.
Professors Michael Kassner, Vitali F. Nesterenko and Joanna McKittrick
 - Studies in Condensed Matter Physics.
Professors Frances Hellman and Jorge Hirsch
 - Studies in Dislocatons and Defects.
Professor Sia Nemat-Nasser

ABSTRACT OF THE DISSERTATION

Planar Josephson Junctions and Arrays
via Electron Beam Lithography and Ion Damage

by

Shane A. Cybart

Doctor of Philosophy in Materials Science and Engineering

University of California, San Diego, 2005

Professor Robert C. Dynes, Chairman

In the years to come, the size and cost of cryo-coolers will get smaller and the demand for a VLSI high-temperature superconducting (HTS) Josephson junction technology will increase. One possible candidate to fill this need is the “ion-damage” Josephson junction. These junctions are fabricated by using ion bombardment to create localized narrow regions of defects in the plane of a thin film superconductor. These regions have a superconducting transition temperature lower than that of the bulk film and act as non-hysteretic Josephson junctions. The advantage of these junctions over other technologies is that they have no interfaces between different materials, and can be placed over 10 times closer to each other in comparison to competing techniques.

Individual junctions and multi-junction serial arrays were fabricated and characterized. Current-voltage characteristics were well described by the restively

shunted junction model at temperatures close to the critical temperature of the weak link. At lower temperatures the junctions became strongly coupled and exhibit flux flow characteristics. It is suggested that this is due to the barrier changing from non-superconducting to superconducting, which allows Abrikosov vortices to enter the junction. Junction arrays have flat giant Shapiro steps at N times the voltage predicted by the ac Josephson relation, where N is the number of junctions in the array. Modulation of the critical current was measured to observe the dc Josephson effect. Unlike other planar junction types these junctions do not exhibit flux-focusing effects in magnetic field measurements and are more comparable with classical sandwich type Josephson junctions. Low temperature (100°C) anneals substantially increased the critical current and operating temperature possibly from the recombination of vacancy-interstitial pairs formed during implantation. Junctions were also fabricated from the low temperature superconductor MgB_2 for comparisons with the HTS junctions and to show that this technology is not limited to HTS.

Overall it has been shown that this technique can be used to reproduce junctions with uniform resistances and critical currents. With a few innovations in materials and/or lithography, ion damage Josephson junctions may become common place in the medical, communications, and defense industries

Chapter 1

Introduction

The Josephson effect is the quantum mechanical tunneling of electron pairs between two weakly coupled superconductors. This was first described by Brian D. Josephson in 1962 in a series of papers [1–3] that earned him a share of the 1973 Nobel Prize in Physics along with Ivar Giaever and Leo Esaki. After Anderson and Rowell demonstrated the first Josephson junction at Bell Labs in 1963 [4], there has been a sustained effort in the study of the Josephson effect to investigate the fundamental physics and in the development of junctions with reproducible parameters for electronic devices.

Josephson junctions are the basic building blocks for most of the active superconducting devices. They have been used for a variety of applications such as magnetic field sensors, voltage standards, and high speed digital logic. The most sensitive sensor of magnetic field is a superconducting interference device (SQUID) magnetometer [5] with an energy resolution which is close to the quantum limit. The SQUID device consists of a junction pair connected in parallel and has been used to measure fields as small as a few femto Tesla (10^{-15} Tesla). They have found practical use in laboratory magnetometer systems, magnetocardiograms, magnetoencephalography and non-destructive evaluation, as well as a variety of laboratory studies. The ac Josephson effect has been used as a voltage standard for some time now [6]. More recently, these voltage standards have been based on

series arrays of junctions. The accuracy of these standards are unsurpassed and are used to define the volt. This comes about because the Josephson effect converts frequency, which is easily measured accurately, to voltage. These voltage standards have also been used as digital-to-analog converters with quantum accuracy and are highly coveted by the military for RADAR applications. Josephson digital logic was highly pursued by companies in the 80's because of the fast switching speeds but advances in semiconductors caused most companies to abandon Josephson logic. Research in quantum computing has renewed interest in using Josephson junctions for digital applications with the advent of rapid single flux quantum logic [7].

With the exception of SQUIDs all successful commercial applications of Josephson junctions have been fabricated from low temperature superconducting material to date. In 1986 the discovery of the high- T_c cuprates with transition temperatures above the boiling point of liquid nitrogen (77 K) spurred a large research effort in HTS (high temperature superconductor) junctions. To more fully take advantage of the HTS breakthrough, many techniques have been explored to develop a reliable and robust junction technology, but due to the complexity of the HTS materials a reliable junction technology has yet to be established.

This thesis builds on the thesis work of Andrew Katz [8] (UCSD) who demonstrated successful single junctions using a technology based on electron beam lithography and ion implantation. The goal was to study the physics and material parameters to this end. Chapter 2 provides background in superconductivity, Josephson junctions, and effects of ion implantation in superconductors. This is followed by a description of device fabrication and measurements. Chapters 5 through 7 is a collection of results from single junctions, junction arrays and SQUID devices. Finally, in the last chapter, conclusions are drawn and recommendations for further work are made.

Chapter 2

Background

2.1 Historical Background

In 1911 Kamerlingh Onnes discovered that electrical resistance of mercury wires abruptly dropped to zero when they were cooled below 4.2 K [9]. He named this phenomenon superconductivity and in the years to follow many other materials were found to exhibit this effect. Besides zero electrical resistance Meissner found superconductors are perfect diamagnets and expel magnetic field [10]. Phenomenological theories put forth by the Londons [11], and Ginsburg and Landau [12], described superconductivity in terms of electrodynamics and thermodynamics. This explained the observation of the Meissner effect and revealed that the transition from normal conductor to superconductor is a 2nd order phase transition which happens upon cooling below a temperature unique to the specific material called the critical temperature, T_c . For most conventional superconductors the mechanism of superconductivity is well understood in the context of a microscopic theory by Bardeen, Cooper, and Schrieffer (BCS theory) [13].

2.2 Coherent Phenomena in Superconductors

The effects observed in superconductors are a result of macroscopic coherence of the current carriers in the material. The motion of charge carriers in

normal matter can be described by the ordinary Schrödinger equation:

$$i\hbar\frac{\partial\psi}{\partial t} = H\psi \quad (2.1)$$

where ψ is the wave function of a particle,

$$\psi = |\psi(r, t)| \exp [i\theta(r, t)] \quad (2.2)$$

H is a Hamiltonian, θ is the phase of the wavefunction, and \hbar is Planck's constant. In the stationary state $|\psi|$ is constant because from quantum mechanics $|\psi|^2$ is proportional to the density of particles. H can be replaced by E and equation (2.1) takes the form,

$$\hbar\frac{\partial\theta}{\partial t} = -E \quad (2.3)$$

Equation (2.3) shows that the quantum behavior of a carrier is reduced to a function of its wavefunction's phase. In normal conductors, electrons obey Fermi-Dirac statistics and only two carriers can have the same energy; therefore the rate of phase change, $\frac{\partial\theta}{\partial t}$ can only be the same for two carriers. Macroscopic observables are determined by summing over a large number of particles and therefore phase information from the individual carriers is lost.

In superconductors, BCS theory shows that two electrons with opposite momentum and spin can interact with lattice phonons and form a bound pair called a Cooper pair. Cooper pairs obey Bose-Einstein statistics because the sum of two electrons' spin is an integer. Therefore many carriers may have the same energy. As a consequence, many of them at the Fermi surface can condense into a single collective state, the superconducting ground state. As a result their $\frac{\partial\theta}{\partial t}$ are identical. This results in macroscopic quantities that depend on phase, i.e. current.

Only electrons close to the Fermi surface can participate in pairing. Electrons with higher or lower energies remain unpaired and are called quasi-particles to distinguish them from the paired electrons in the superconducting state. It is energetically favorable for the pairs' wavefunctions, ψ to phase lock forming a superfluid condensate, which can be described by a single wave function commonly

called the order parameter, Ψ . There is phase coherence between the pairs over a length scale called the coherence length, ξ . In a volume of ξ^3 there are typically 10^6 pairs in this coherence volume for conventional superconductors (e.g. Nb, Pb). This coherence length is one of the two important length scales in superconductivity. The phase coherence leads to two important phenomena in superconductors, magnetic flux quantization and the Josephson effect.

The phase of the order parameter must be unique and single-valued, thus around a closed loop it must return to itself (modulo 2π). This condition requires any flux passing through the loop to be quantized to the values,

$$\Phi = n\Phi_0 \tag{2.4}$$

where n is an integer and Φ_0 is the flux quantum,

$$\Phi_0 = \frac{h}{2e} = 2.07 \times 10^{-15} \text{ Webers}$$

2.3 Superconductors in Magnetic Fields

Superconductors repel magnetic fields in the superconducting state as expected for a perfect conductor; however Meissner found that field was also expelled from a superconductor while undergoing its phase transition from normal to superconducting. This is contrary to what classical physics predicts, for a perfect conductor should trap the field inside [14]. In the superconducting case, the magnetic fields generate superconducting eddy currents that create an exactly opposing field that repels the flux making it a perfect diamagnet. Heinz and Fritz London showed that in a bulk superconductor, there is a length scale for these screening currents and over that length the magnetic field penetrates the surface and decays exponentially [11],

$$B = B_0 \exp \left[\frac{-x}{\lambda_L} \right]$$

where B is magnetic field, x is the distance from the surface and λ_L is the London penetration depth, a material specific constant. This screening length λ_L is the

second important length scale in superconductivity.

In the presence of a magnetic field the free energy of the normal state is lower and the superconductivity is quenched. This happens at a field called the thermodynamic critical field, H_c . This places a limit on the current that may be carried by a superconductor due to the magnetic fields induced by the current itself [14]. This limit is called the critical current, I_c .

The ratio of the two superconducting length scales is called the Ginsburg-Landau parameter [12].

$$\kappa = \frac{\lambda_L}{\xi}$$

This value plays an important role in how superconductors respond in magnetic fields. In typical classical clean elemental superconductors (Type I), $\lambda_L \sim 50$ nm and $\xi \sim 300$ nm resulting in $\kappa \ll 1$. In this case all magnetic field is expelled from the interior for fields below a critical field called H_{c1} and this is the Meissner effect. Fields in excess of H_{c1} quench superconductivity and return the material to its normal state. In superconductors where λ_L is larger than ξ or $\kappa > \frac{1}{\sqrt{2}}$, (Type II), Abrikosov showed that it is thermodynamically favorable for the superconductor to exist in a mixed normal and superconducting state [15]. For fields in excess of H_{c1} , the magnetic field penetrates the superconductor in the form of vortices where the magnetic field is confined. Vortices have a normal core with a radius of the order of ξ , where the field lines penetrate. The core is surrounded by superconducting shielding currents extending out for a distance of approximately λ_L . Due to the flux quantization in superconductors (equation 2.4), each vortex contains only one flux quantum, Φ_0 . If field is increased further beyond H_{c1} more vortices form to accommodate the additional flux. An additional increase to a field called H_{c2} causes the cores to overlap and the material reverts to its normal state [14]. Vortices in a superconducting current carrying wire or bridge (current density \mathbf{J}) experience a Lorentz force from the current,

$$\mathbf{F} = \mathbf{J} \times \frac{\mathbf{B}}{c} .$$

This force causes vortices to move transverse to the current. The time rate of change of the flux results in an electric field parallel to the current,

$$E = \frac{-1}{c} \frac{d\Phi}{dt}$$

and this acts like a resistive voltage [14].

It is energetically favorable for a vortex core to exist in a region in the material that is non-superconducting such as a defect or grain boundary. This acts like a force opposing the Lorentz force from current flow and is referred to as flux pinning. For high current applications in superconductivity, defects or pinning centers are sometimes introduced into the material to increase the critical current.

2.4 Josephson Junctions

The most significant phenomenon related to the phase coherence of the charge carriers in superconductors is its ability to carry a current at zero voltage, a supercurrent. A particularly interesting manifestation of this phenomenon occurs when two superconductors are weakly connected and a supercurrent flows in a similar fashion. This phenomenon is called the Josephson effect. If two superconductors are coupled through a weak barrier such as an insulator or normal metal (Figure 2.1) a supercurrent will flow in the absence of a potential difference (voltage) if there is a phase difference between the order parameters of the two superconductors. The difference between the phases of the two superconductors is defined as the Josephson phase,

$$\varphi \equiv (\theta_1 - \theta_2) . \quad (2.5)$$

The supercurrent in the simplest case is described by the first Josephson equation [1],

$$I_s = I_c \sin \varphi . \quad (2.6)$$

Where the critical current, I_c is the maximum supercurrent that the junction will sustain and is determined by junction geometry, temperature, and the materials

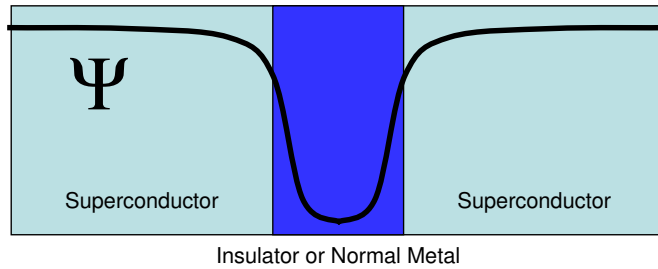


Figure 2.1: Schematic diagram of a Josephson junction. The order parameters from the superconducting electrodes decay into the barrier and couple the wavefunctions together.

of the weak link and electrodes, amongst other factors.

Furthermore if there is a potential difference between the two superconductors the phase difference changes with time and is described by the second Josephson equation [1],

$$\frac{\partial \varphi}{\partial t} = \frac{2e}{\hbar} V = \frac{2\pi}{\Phi_0} V \quad (2.7)$$

A simple derivation of this was put forth by Likharev [16]. Writing equation (2.3) for each of the superconductors and subtracting yields,

$$\hbar \frac{\partial \varphi}{\partial t} = E_2 - E_1 \quad (2.8)$$

The energy difference is between the cooper pairs of charge $2e$ in either side and can only exist in the presence of an electrochemical potential difference V . Thus $2eV$ can be substituted for the energy difference and we are left with the second Josephson equation. The second Josephson equation is exact and only depends on fundamental constants. If a dc voltage is applied across a junction the phase evolves with time at a frequency,

$$f = \frac{2e}{h} V . \quad (2.9)$$

This results in an ac supercurrent oscillating between the two superconductors at frequency f . The proportionality factor between voltage and frequency is referred to as the Josephson constant,

$$K_j \equiv \frac{2e}{h} = 483.597879 \frac{\text{THz}}{\text{V}} . \quad (2.10)$$

This forms the basis for the definition of the volt and the Josephson voltage standard. It is now a common voltage standard and the way the “volt” is maintained [6].

2.4.1 The RCSJ Model

An equivalent circuit model of a Josephson junction was put forth independently by Stewart [17] and McCumber [18]. They modeled the junctions as a resistor, capacitor, and a current source connected in parallel as in Figure 2.2. This is called the Resistive and Capacitive Shunted Junction model (RCSJ). In practice Josephson junctions are typically current biased and equating it to the currents through the three parallel elements yields,

$$I = \frac{V}{R_n} + C \frac{\partial V}{\partial t} + I_c \sin \varphi \quad (2.11)$$

The first term is the quasiparticle current in the finite voltage regime. The second term reflects the capacitance between the electrodes. The sinusoidal term represents the supercurrent from the first Josephson equation (2.6). Using equation (2.7) the voltage in the resistive and capacitive terms can be rewritten in terms of the Josephson phase.

$$I = \frac{\hbar C}{2e} \frac{\partial^2 \varphi}{\partial t^2} + \frac{\hbar}{2eR} \frac{\partial \varphi}{\partial t} + I_c \sin \varphi \quad (2.12)$$

Dividing by I_c , and introducing a new time variable,

$$\tau = I_c R_n \frac{2e}{\hbar} t = \omega_J R_n C$$

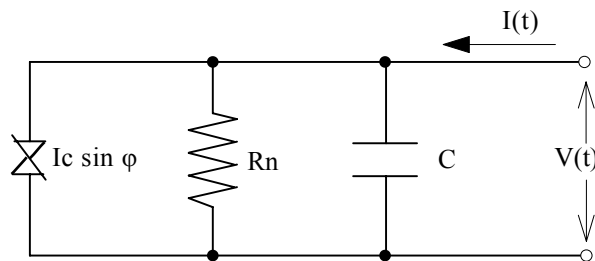


Figure 2.2: Equivalent circuit for a Josephson junction used in the RCSJ model.

equation (2.12) can be simplified to,

$$\frac{I}{I_c} = \beta_c \frac{\partial^2 \varphi}{\partial \tau^2} + \frac{\partial \varphi}{\partial \tau} + \sin \varphi \quad (2.13)$$

where β_c is the Stewart-McCumber damping parameter,

$$\beta_c = I_c R_n \frac{2e}{\hbar} R_n C = \omega_J R_n C$$

and ω_J is the Josephson frequency. In the case of non-hysteretic junctions, such as the ones studied in this thesis, the capacitance is small and the capacitive term may be omitted. In this limit equation (2.13) becomes a first order differential equation which can be written as,

$$\frac{\partial \varphi}{\partial t} = \frac{2e}{\hbar} I_c R_n \left[\frac{I}{I_c} - \sin \varphi \right] \quad (2.14)$$

In this form it is clear that for $I > I_c$ that the instantaneous voltage $\frac{\partial \varphi}{\partial t}$ is positive, but varies sinusoidally with φ . When $\sin \varphi$ is positive the supercurrent is in the direction of the bias current and the phase advances faster. When $\sin \varphi$ is negative the supercurrent is in the opposite direction of the bias and the phase advances slower. For currents just above I_c the voltage across the junction is a series of pulses of frequency,

$$f = \frac{2e}{h} V_{dc} \quad (2.15)$$

where V_{dc} is the time averaged dc voltage. These pulses have a maximum of $2 I_c R_n$ and area time integral exactly equal to the flux quantum such that,

$$\int V dt = \frac{h}{2e} = \Phi_0 \quad (2.16)$$

The time average dc voltage may be found by integrating equation 2.14,

$$\begin{aligned} V &= 0, & \text{for } I < I_c \\ V &= I_c R_n \sqrt{\left(\frac{I}{I_c}\right)^2 - 1}, & \text{for } I > I_c \end{aligned} \quad (2.17)$$

This results in a parabolic current-voltage characteristic at biases near I_c , and approaches Ohms law at higher biases (Figure 2.3).

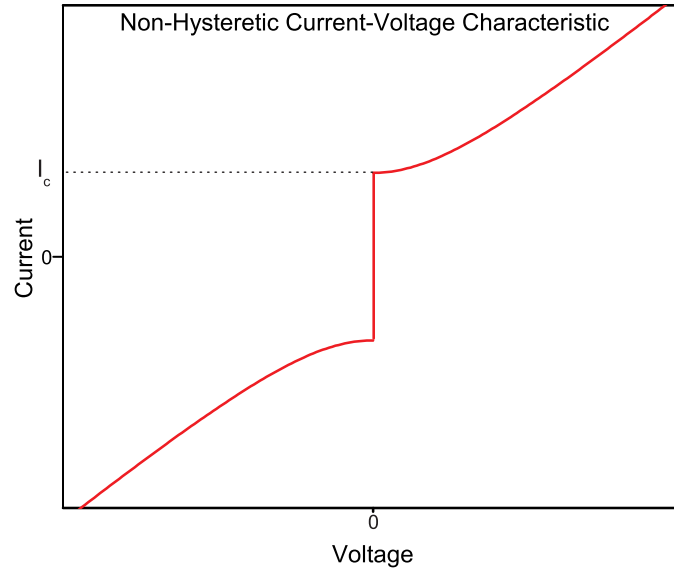


Figure 2.3: $I - V$ characteristic for a non-hysteretic Josephson junction with small capacitance.

2.4.2 The Effect of an AC Bias on Josephson Junctions

If a Josephson junction is biased with both ac and dc simultaneously, steps occur in the supercurrent (Figure 2.4) at the precise values,

$$V = \frac{nhf}{2e} \quad (2.18)$$

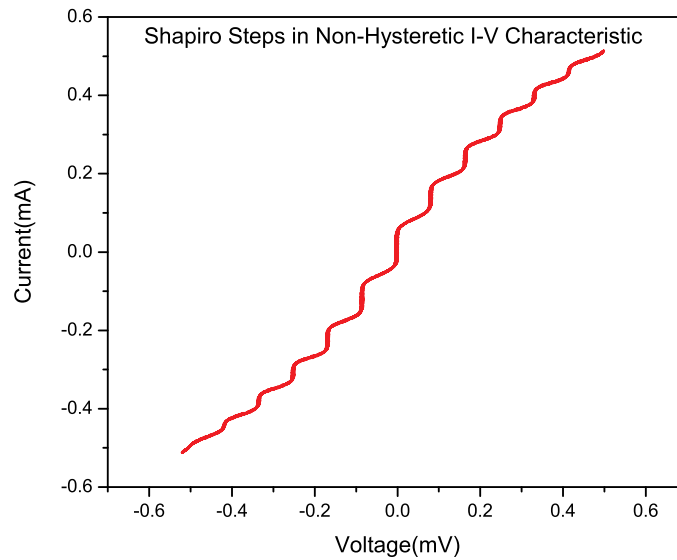


Figure 2.4: Shapiro steps in the $I - V$ characteristic for a non-hysteretic Josephson junction simultaneously biased with both ac and dc current

where f is the frequency of the ac bias and n is an integer. These were also predicted by Josephson in his famous paper [1]. They are called Shapiro steps named after S. Shapiro who was the first to observe them in a junction [19].

Integrating the second Josephson equation (2.7) to determine φ and combining it with the first Josephson equation (2.6) results in,

$$I_s(t) = I_c \sin \left[\int_0^t \frac{2e}{\hbar} V(t') dt' + \varphi_0 \right] \quad (2.19)$$

Taking $V(t)$ to be the sum of a dc voltage and an ac voltage of frequency ω_s ,

$$I_s(t) = I_c \sum_{n=-\infty}^{\infty} (-1)^n J_n \frac{2eV_{ac}}{\hbar\omega_s} \sin [(\omega_J - n\omega_s)t + \varphi_0] \quad (2.20)$$

where J_n is a Bessel function of the first kind. There is only a dc component to the supercurrent when $n\omega_s = \omega_J$ or equivalently $V = \frac{nhf}{2e}$, this creates steps in the $I-V$ characteristic with half width determined by, $I_c J_n \frac{2eV_{ac}}{\hbar\omega_s}$ (Figure 2.5). This derivation assumes that the junction is voltage biased which is very difficult to do in practice because the impedance of a junction is very small compared to typical sources. For the case of a current biased junction an analytical solution is not possible and numerical calculations are necessary [20]. Numerical results for

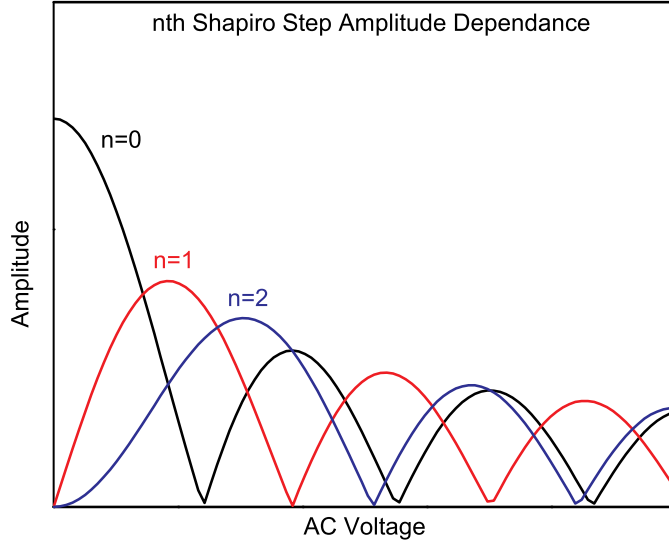


Figure 2.5: Shapiro step amplitude dependence as a function of ac bias.

a current biased junction resemble the voltage bias case and show a Bessel-like dependence of the step amplitudes [21].

2.4.3 The Josephson Penetration Depth

For the following discussions it is essential to clarify the variables to represent the spatial junction parameters to be used for the remainder of this dissertation. Figure 2.6 is a schematic diagram of a planar junction with current flow along the x -axis. The dimension of the barrier in the direction of the current will be referred to as the junction length, l . The dimension of the bridge along the y -axis will be referred to as the junction width, w and the thickness of the film in the z -direction will be referred to as thickness, t . In the absence of a magnetic field the supercurrent in a junction is distributed evenly across its length provided that its length is smaller than a quantity called the Josephson penetration depth λ_J ,

$$\lambda_J \equiv \sqrt{\frac{\Phi_0}{2\pi L_0 J_c}}, \quad (2.21)$$

where J_c and L_0 is the critical current and inductance, per unit length of the junction respectively. The Josephson penetration depth is a screening length similar to the London penetration depth in bulk superconductors. For classical sandwich type junctions it can be shown [20] that the Josephson penetration depth takes the familiar form,

$$\lambda_J = \sqrt{\frac{\Phi_0}{4\pi^2 \mu_0 j_c (2\lambda_L + l)}}, \quad (2.22)$$

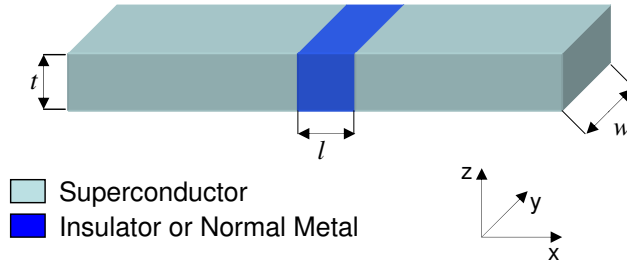


Figure 2.6: 3-dimensional representation of a Josephson junction. The current flow is along the x -axis, and the width of the barrier lies along the y -axis.

where j_c is the current density, λ_L is the London penetration depth of the material, and l is the length of the junction barrier. This relation is not applicable to junctions with a planar geometry because the inductance is not the same as in the classical sandwich geometry [22]. Tolpygo and Gurvitch [22] derived an expression for planar junctions by making the assumption that the inductance was dominated by the kinetic inductance of the film. In the thin film limit where the thickness of the film t is less than the London penetration depth the kinetic inductance can be taken as $L \approx \frac{2\mu_0\lambda_L^2}{wt}$. Using this inductance results in the expression,

$$\lambda_J = \sqrt{\frac{\Phi_0 w}{4\pi^2 \mu_0 j_c \lambda_L^2}} \quad (2.23)$$

which differs from the classical formula by about a factor of $\sqrt{w/\lambda_L}$ which implies that the Josephson penetration depth in planar junctions is larger.

The Josephson penetration depth plays an important role in how current is distributed in a junction. Consider the junction depicted in Figure 2.7(a). The current in the electrodes is carried along the edges of the bridge extending a

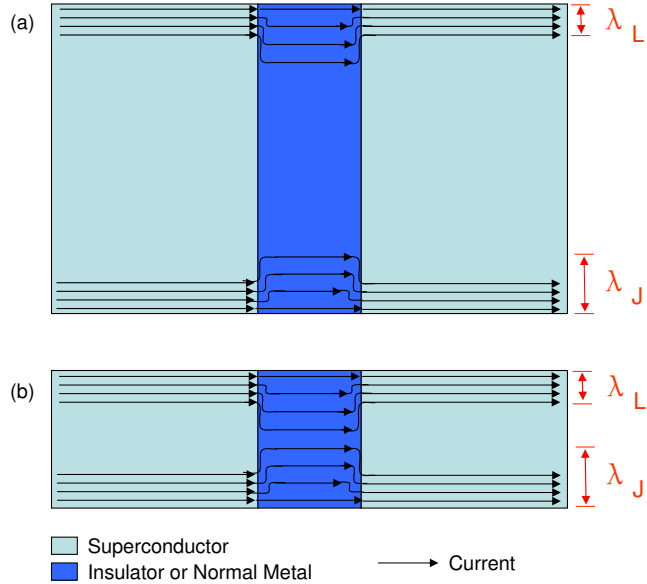


Figure 2.7: Two dimensional cross-section showing the current density in a long (a) and short (b) Josephson junction. Current in the electrodes is carried on the edges and penetrates a distance of λ_L into the interior. Inside of the barrier this screening length is λ_J .

distance of λ_L into its interior. Upon reaching the junction's barrier the current penetrates further up to a distance of λ_J , but is still screened from the interior. If the width of the junction is comparable to λ_J as in Figure 2.7(b), the current distributes itself evenly across the junction's length. Junctions of this type are referred to as "short" junctions and in the former case of Figure 2.7(a) they are called "long" junctions. The junctions in this thesis work are considered as short junctions which simplifies the following discussion of the effect of magnetic field on the supercurrent.

2.4.4 The Effect of Magnetic Field on the Supercurrent

The phase of a "short" Josephson junction is the same along the width of its barrier, except for the case when the junction is in a magnetic field. Flux threading the junction causes the phase to vary spatially which results in a redistribution of the supercurrent. Consider the junction depicted in Figure 2.6 with a field H_z applied along the z -axis. It can be shown that the phase varies along the width of the junction as,

$$\frac{\partial\varphi}{\partial y} = \frac{-2e\acute{l}}{\hbar}H_z \quad (2.24)$$

where \acute{l} is equal to the length of the region penetrated by the field. This consists of the length of the junction barrier and includes the distance the field penetrates into the electrodes on either side so that $\acute{l} = l + 2\lambda_L$. For constant field this can be integrated and substituted into the first Josephson equation(2.6) to obtain the supercurrent density along the junction,

$$J_s = J_c \sin \left[\frac{2e\mu_0\acute{l}}{\hbar}H_z y + \varphi_0 \right] \quad (2.25)$$

where φ_0 is an integration constant.

The critical current can be found by integrating equation (2.25) and choosing φ_0 so that the current is maximized. In the case of a rectangular shaped

junction with barrier width w this results in,

$$I_c(H) = I_c(0) \left| \frac{\sin\left(\frac{e\ell w\mu_0 H_z}{\hbar}\right)}{\left(\frac{e\ell w\mu_0 H_z}{\hbar}\right)} \right| \quad (2.26)$$

This can be written in terms of the flux through the junction, $\Phi = \ell w\mu_0 H_z$ and the flux quantum $\Phi_0 = \frac{e}{\hbar}$,

$$I_c(H) = I_c(0) \left| \frac{\sin\left(\frac{\pi\Phi}{\Phi_0}\right)}{\left(\frac{\pi\Phi}{\Phi_0}\right)} \right| \quad (2.27)$$

This function, plotted in Figure 2.8, is the absolute value of a sinc function as in a single slit interference in optics, and is a Fraunhofer pattern with a periodicity of a flux quantum in the junction. It is commonly used as a test for the Josephson effect and a measure of the uniformity of the current distribution in a junction. Figure 2.9 shows the distribution of current in the junction for different values of flux. Minima in the sinc function occur for integer values of Φ_0 , because there is an equal amount of current in both directions. The maxima occur at half integer values and the maximum amplitude is reduced as the oscillations become smaller.

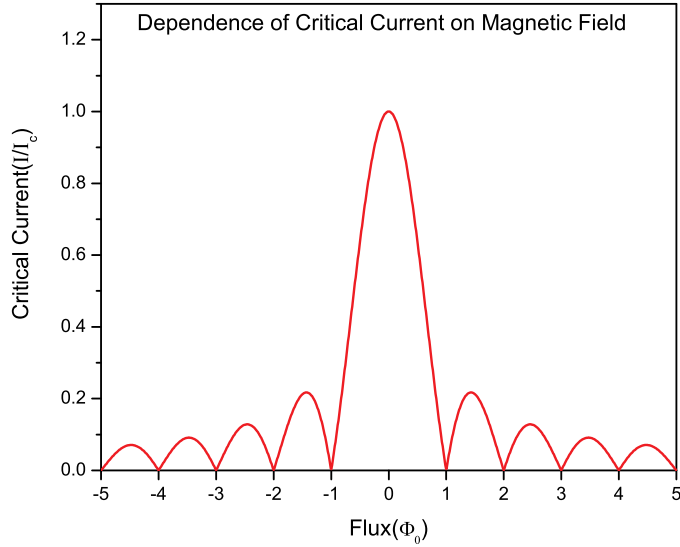


Figure 2.8: Critical current as a function of magnetic flux for a rectangular junction.

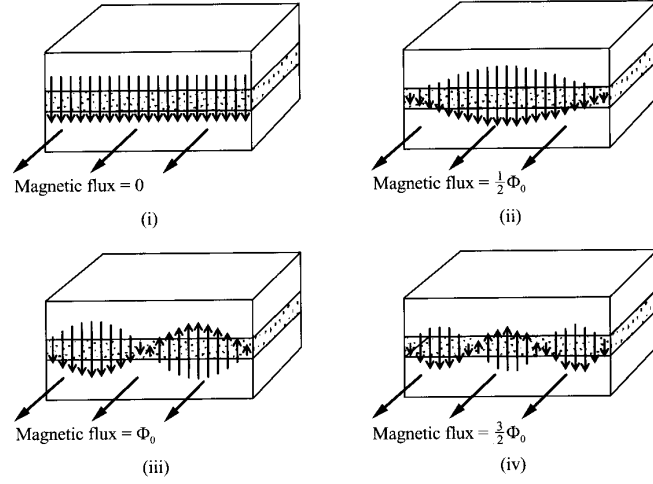


Figure 2.9: Spatial distribution of the supercurrent in a Josephson junction for different values of magnetic flux. One can see that at the minima in the sinc function in Figure 2.8 (integer values of Φ_0) that there is an equal amount of current in both directions. For half integer values of Φ_0 the net-current flow is in one direction but its magnitude is reduced as more oscillations traverse the junction [20].

2.4.5 Proximity Coupling

When a superconductor is in contact with a normal metal, cooper pairs from the superconductor diffuse into the normal metal and quasiparticles from the normal metal diffuse into the superconductor. They can extend for hundreds of nanometers in either direction depending on the coherence length in that material. This has the effect of reducing the T_c of the superconductor and making the normal metal superconducting. This is called the proximity effect and plays an important role in metallic barrier junctions. These types of junctions can be of two types. The first will be referred to as SNS which stands for superconductor-normal metal superconductor. For this junction the barrier is a “true normal” metal which does not undergo a superconducting transition at any temperature. SN’S will be used to represent a junction that has a normal metal barrier which has a superconducting transition below the temperature of operation.

The pair amplitude for both cases, $F(x)$ decays into the normal region exponentially in the form of,

$$F(x) \propto e^{-k|x|} \quad (2.28)$$

where k is determined by the properties of the material and temperature. For

“clean” materials,(by “clean” it is meant that the electronic mean free path is greater than the coherence length)

$$k^{-1} = \frac{\hbar v_{fn}}{2k_b T} \quad (2.29)$$

where v_{fn} is the Fermi velocity of the normal metal. If the material is in the dirty limit where the mean free path, $l_{e,n}$ is much smaller than the coherence length ($l_{e,n} \ll \xi_n$),

$$k^{-1} = \xi_n \quad (2.30)$$

for SNS junctions and,

$$k^{-1} = \xi_n \sqrt{1 + \frac{2}{\ln\left(\frac{T}{T_c}\right)}} \quad (2.31)$$

for SN'S junctions where,

$$\xi_n = \sqrt{\frac{\hbar v_{fn} l_{e,n}}{6\pi k_b T}} \quad (2.32)$$

is the normal metal coherence length, that can be much longer than that of the superconductor. Due to the longer coherence length in most metals the barriers of SNS and SN'S junctions can be much wider than in the case of an SIS tunnel junction where the barrier is insulating. The temperature dependence of the maximum super current, close to T_c for these junctions was calculated by de Gennes [23] to be,

$$I_c(T) = I_{c0} \left(1 - \frac{T}{T_c}\right)^2 \frac{kl}{\sinh kl} \quad (2.33)$$

where I_{c0} is the critical current at 0 K and l is the width of the barrier.

2.4.5.1 Ion Damage SN'S Junctions

In high- T_c materials the critical temperature can be significantly reduced by disorder inflicted from ion or electron beam damage. This has been used to create SN'S junctions within the plane of a single thin film [24, 25], by selectively damaging (reducing the T_c) of the region intended to serve as a barrier. These junctions have no interface between the higher T_c and lower T_c materials and both

regions have nearly identical properties with the exception of T_c . Clarke proposed a model where the interfaces can move with temperature as a form of Andreev scattering, i.e the width of the barrier gets smaller as temperature is reduced [26]. To account for this movement “soft” boundary conditions have been used with the classical de Gennes model, equation (2.33) to explain experimentally measured critical current temperature dependence [27]. Katz and Dynes [27] introduced a temperature dependant junction width into the de Gennes model which results in a critical current dependence of the form,

$$I_c(T) \propto \left(1 - \frac{T}{T_c}\right)^3 \quad (2.34)$$

The additional factor of T , from the temperature dependant width, fits well with experimental data (Figure 2.10). Furthermore they also introduced a current dependant resistance because at higher biases the interfaces move away from the center of the weak link as a local I_c is exceeded for more of the material. They

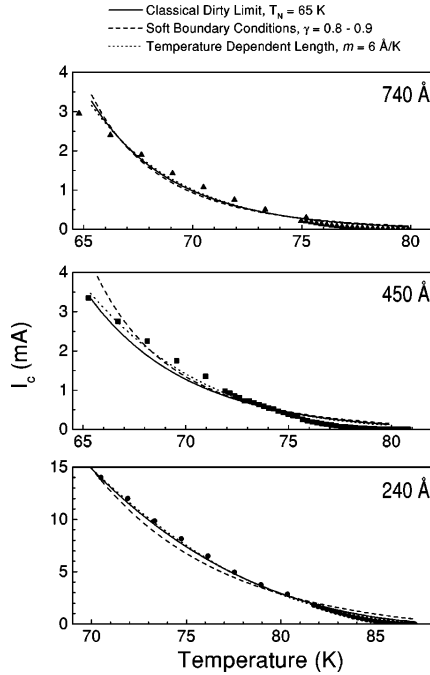


Figure 2.10: Critical current dependencies for 3 ion-damage Josephson junctions of different lengths. The temperature dependant barrier length provides a better fit then the classical de Gennes model with and without “soft” boundary conditions [27].

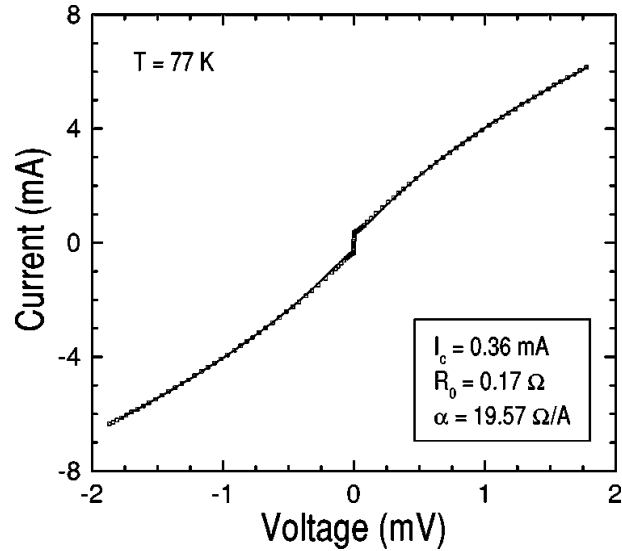


Figure 2.11: $I-V$ characteristic for an ion-damaged Josephson junction fit with the RSJ model modified with a current dependant resistance [27].

suggested a resistance of the form,

$$R(I) = R_0 + \alpha I \quad (2.35)$$

where α is a fitting parameter. Substituting this into the RSJ model fit their data well (Figure 2.11) and explained a downward curvature observed in the $I-V$ curve for junctions of this type [27].

2.4.5.2 SS'S Junctions

Another type of junction worthy of mention is referred to as an SS'S junction, where the barrier material like in the SN'S case is also a reduced T_c superconductor. The difference between the two is that the SS'S junction operates below the T_c of the barrier whereas the SN'S junction operates above T_c . The implications of having a superconducting barrier will be discussed in more detail in chapter 5.

2.4.6 Series Arrays of Josephson Junctions

Series or parallel arrays of junctions are desirable for applications where junctions are used as oscillators [28], voltage standards [29] or sensitive detectors. A

Josephson oscillator involves applying a dc voltage across the junction and coupling the ac supercurrent generated into an antenna. It is difficult to do this in practice with single junctions because the single junction impedances are typically very small. Utilizing series arrays of junctions increases the impedance and circumvents this difficulty. Furthermore the power output from an array increases as the square of the number of junctions in the array. In single junction oscillators the radiation line width is proportional to the normal state resistance, $\Delta\omega \propto R_n$. In the case of an impedance matched array it decreases by the square of the number of junctions in the array, i.e $\Delta\omega \propto \frac{R_n}{N^2}$ [20].

For voltage standards, arrays are used to increase the voltage available [20]. For a single junction driven at 20 GHz the voltage of the first Shapiro step occurs at 40 μ V which is too small for practical applications. However in an array the voltage from equation (2.6) increases as the number of junctions in the array.

$$V = \frac{nNhf}{2e} \quad (2.36)$$

Where n is the step number, N is the number of junctions in the array and f is the drive frequency, so a 1000 junction array at 20 Ghz yields 40 mV, a usable value.

2.4.6.1 The Josephson Arbitrary Waveform Generator

Most Josephson voltage standards are dc standards. A junction array is biased with a high frequency ac current to create constant voltage steps. The number of junctions needed to produce the desired voltage are dc biased simultaneously with the ac drive signal. The dc current is selected to occur at the constant voltage step. The frequency of the ac current and the number of junctions biased determine the voltage of the Shapiro step. This type of standard may not be used for ac voltages, especially for high frequency (>1MHz) by simply switching between the desired voltages to create a waveform because the voltage across the array is undefined during the switching process [30]. Northrop Grumman and NIST co-

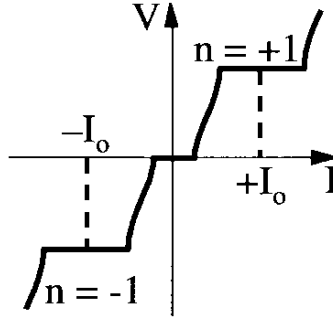


Figure 2.12: Voltage-current characteristic for a junction array simultaneously ac and dc biased depicting optimum dc bias currents, $\pm I_0$ for selection of the output voltage polarity [30].

developed a new type of ac standard that involves closely spaced junctions in an array as a lumped circuit element [31]. This circuit is called a Josephson arbitrary waveform generator. It is operated by biasing the junction with a sinusoidal drive signal and a 2-level binary bit stream. Waveforms may be stored in the form of binary code for the playback of waveforms with quantum accuracy.

Figure 2.12 shows the $V-I$ characteristic of a junction biased simultaneously with ac and dc current. The voltage ($V = \frac{nNh\hbar f}{2e}$) of the $n = \pm 1$ Shapiro steps are shown and are the time averaged voltage of a set of pulses whose time integral is precisely equal to the flux quantum (as explained in section 2.41).

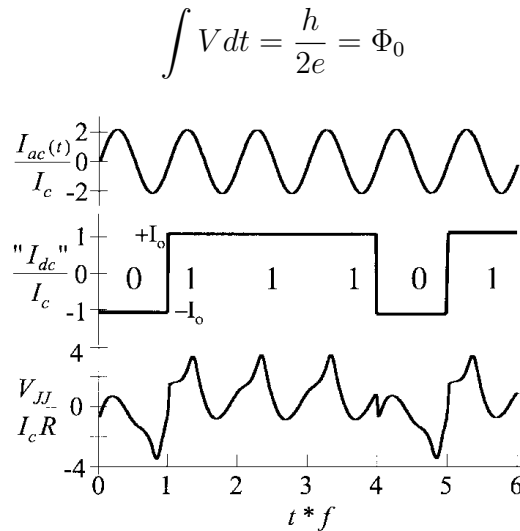


Figure 2.13: Example of dc voltage synthesis using a pulse driven waveform generator. The top curve is the ac bias drive signal, the middle is the binary bit stream and the bottom shows the instantaneous voltage across the junction [30].



Figure 2.14: 2-level binary code used to generate the sine wave S' , the pulses in S_D represent the density of 1's and 0's in the bit stream [30].

The bias currents $+I_0$ and $-I_0$ are used to select the polarity of the voltage output. Time averaged voltages between these two values can be generated by using periodic sequences of bias pulses. Figure 2.13 shows an example of a 6 bit code. The top curve is the drive signal used to ac bias the array. The middle shows the binary pattern used to select which voltage step is output, and the third trace is the time dependant output of the junction array. If this 6 bit pattern is continuously repeated it results in 2 extra positive polarity pulses for each cycle resulting in a voltage equal to $V = \frac{2}{6} \frac{Nhf}{2e}$. Similarly ac voltages can be generated using complex bit patterns. Figure 2.14 shows a two level binary code used to create a sine wave. This code represents the density of the 1's and 0's in the bit stream. In the peak there is a larger density of 1's and in the node there are an equal number of 1's and 0's (i.e. the number of pulses of positive polarity equals that of negative polarity resulting in a zero voltage).

For this device it is essential that the Josephson array appears as a lumped element to the drive signal and the bit stream so that each junction in the array sees the same power. By “lumped element” it is meant that the device is smaller then $\frac{1}{4}$ wavelength of the microwave. For a 1 volt standard driven at 18 GHz Benz has determined the optimum junction parameters for this application [29]. It would require 13,500 junctions with $37\mu V I_c R_n$ products and an inter-junction spacing of 120 nm. The junctions to be described in this thesis work were motivated by this application.

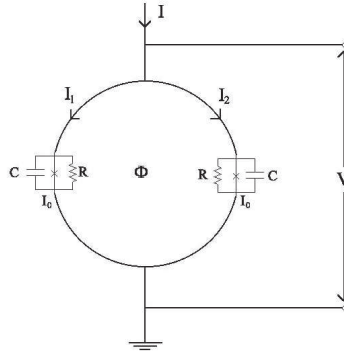


Figure 2.15: Circuit diagram for a dc SQUID.

2.4.7 The DC SQUID

The dc SQUID [5] (Figure 2.15) consists of two Josephson junctions connected in parallel in a superconducting loop with inductance L . Biasing the SQUID with a constant current I_B , causes the voltage V across the SQUID to oscillate with a period f_0 , as external magnetic flux Φ is changed (figure 2.16). Small changes in magnetic flux, ($\Phi \ll \Phi_0$) can be measured by selecting a bias current that maximizes the amplitude of the voltage modulation and sets the external flux at,

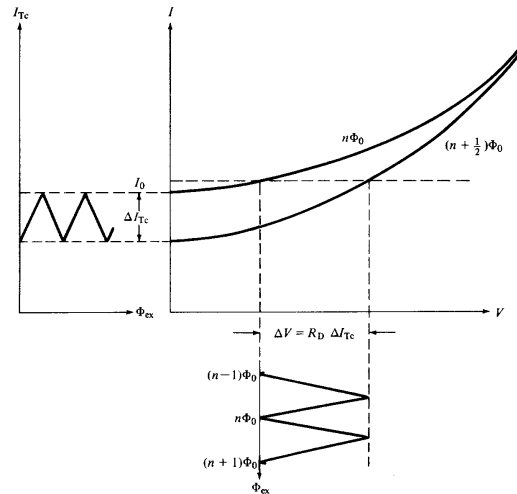


Figure 2.16: Modulation of the current-voltage characteristic for a dc SQUID the trace on the left shows how I_c changes with applied flux and the trace underneath shows the voltage modulation or “triangle wave” resulting [20].

$$(2n + 1) \frac{\Phi_0}{4}, \quad (n = 0, 1, 2, \dots)$$

so that the flux-to-voltage transfer coefficient,

$$V_{\Phi} = \left| \frac{\partial V}{\partial \Phi} \right|_I$$

is maximized. Thus the SQUID produces a maximum output voltage signal,

$$\partial V = V_{\Phi} \partial \Phi$$

in response to a small flux signal $\partial \Phi$.

The sensitivity of the SQUID to detect small magnetic fields is ultimately limited by intrinsic white noise associated with the resistances of the junctions. Sensitivity can be improved by connecting many SQUID loops together in a series array [20]. The voltage signal increases by a factor of N while the noise only increases by, \sqrt{N} where N is the number of SQUID loops in the array. Nonuniform junction parameters and/or loop size variations degrade the performance of SQUID arrays. That has made them difficult to realize in high- T_c superconducting materials.

2.4.7.1 Superconducting Quantum Interference Filters (SQIF)

Researchers at the University of Tübingen developed a technology called a superconducting quantum interference filter (SQIF) [32] that is not as sensitive to non-uniformities. The essence of a SQIF is that it employs arrays of SQUIDs with different loop sizes analogous to an unconventional grating structure in optics. The loop sizes can be selected in such a way so that the flux-to-voltage transfer coefficient has a delta like peak and small side lobes in the presence of zero magnetic field (Figure 2.17). In finite field the modulation contributions from the different sized loops prevents a superposition of the junction currents and makes the flux-to-voltage response non-periodic and relatively small. The unique voltage peak at zero field in the SQIF's transfer function makes it a highly sensitive sensor of absolute magnetic field. This is unlike a SQUID which is a relative magnetic

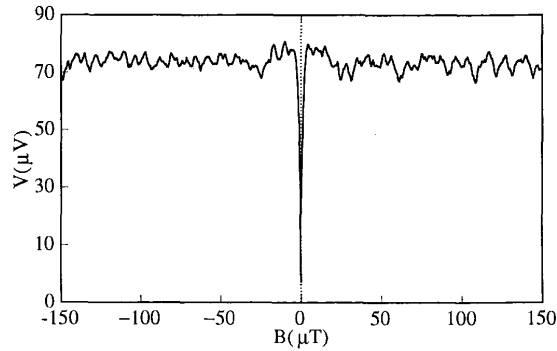


Figure 2.17: Calculated magnetic field response of a serial SQIF [32].

field sensor because voltage peaks occur in the transfer function for fields equal to integer values of the flux quantum (Φ_0). SQUID sensors rely on electronic counters to count these values for measurement of field in excess of Φ_0 . The counting rate of these electronics places a limitation on the sensors bandwidth. Thus the uniqueness of the SQIF's transfer function gives it an advantage in high frequency applications. The disadvantage, of course, is that the SQIF must be operated in ambient fields much less than the earth's field. In the presence of a received microwave signal, the SQIF will see a magnetic field proportional to the signal with the same frequency. The SQIF will give a low voltage response (a pulse) each time the field goes through zero (twice the frequency of the signal). This allows for measurement of the frequency and intensity of the signal. By applying a small static magnetic field (field biasing the SQIF) one can also obtain a signal that is proportional to field, and therefore proportional to the signal with most of the noise filtered out.

2.5 Superconducting Materials

The first materials discovered to exhibit superconductivity were elemental superconductors such as Hg, Pb, Al and Nb. Clean elemental superconductors are type I superconductors with the exception of Nb. They have relatively long coherence lengths and low critical temperatures with the highest being Nb at 9.25 K. Niobium is commonly used for low-temperature Josephson junctions for SQUIDs

and digital Josephson applications. Historically, soon to follow were numerous binary compounds that exhibited superconductivity. Some of these being type II making high field magnets possible. Some of the more notable ones are, NbN, Nb₃Sn, and Nb₃Ge. The latter two belong to a group of compounds called the A15 superconductors named after their crystal structure. This pushed the T_c up to 23.2 K (Nb₃Ge) a record which held for binary compound superconductors until the discovery of MgB₂ in 2001 with a T_c of 39 K. All of these superconductors are described well by BCS theory.

In 1986 Bednorz and Muller discovered superconductivity in a layered ceramic material La_{2-x}Ba_xCuO₄ [33]. Its T_c of 30 K was much higher than any other superconductors at the time and this discovery sparked a large research effort in the new materials. In 1987 a major breakthrough came with the discovery of YBa₂Cu₃O_{7-δ} [34]. Its T_c of 92 K was the first superconductor to have T_c above the boiling point of liquid nitrogen 77 K. This was a major breakthrough as this potentially simplified cooling requirements and reduced cost for a variety of applications.

2.5.1 YBa₂Cu₃O_{7-δ}

YBa₂Cu₃O_{7-δ} (YBCO) belongs to a family of oxygen deficient perovskite layered materials, R-Ba₂Cu₃O_{7-δ}, where R is one of the Rare earth elements, Y, La, Pr, Nd, Sm, Eu, Gd, Tb, Dy, Ho, Er, Tm, Yb, and Lu. YBa₂Cu₃O_{7-δ} is the most studied and widely used of these compounds and the primary material used in this thesis. The nature of superconductivity in these materials is not explained by BCS and has eluded physicists for almost 2 decades, however empirical observations have provided some clues. Figure 2.18 shows a single unit cell of YBCO. It may exist in two different structures depending on the reduced Oxygen content (δ). With $\delta = 1$ the O(1) sites in the Cu(1) layer are vacant and the structure is tetragonal. In this form YBCO is insulating and does not superconduct. Increasing the oxygen content adds atoms at the O(1) sites. When $\delta < 0.65$ oxygen atoms

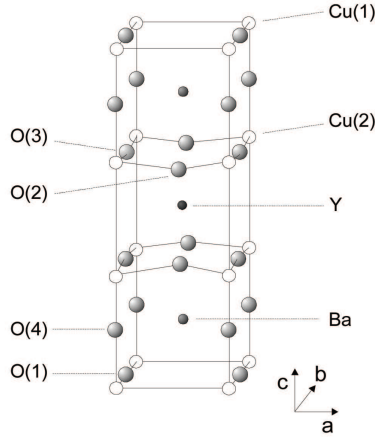


Figure 2.18: Orthorhombic unit cell for $\text{YBa}_2\text{Cu}_3\text{O}_{7-\delta}$, showing the positions of the different atoms. The cell is usually described as three oxygen deficient perovskite cells stacked on top of each other.

at the O(1) sites form Cu-O chains along the b -axis. This elongates the b -axis and changes the structure to orthorhombic, with $a=3.82 \text{ \AA}$, $b=3.89 \text{ \AA}$, and $c=11.68 \text{ \AA}$. Optimum superconducting properties occur when $\delta \sim 0.07$ and all of the O(1) sites are occupied with the exception of a few vacancies. Substitution experiments of atoms at the Cu and rare earth sites provide evidence that conduction occurs in the Cu(2)O planes and the Cu(1)O(1) chains act like a charge reservoir, which provides carriers to the CuO planes. With conductivity confined to a - b planes a large anisotropy in transport properties results. Along the c -axis, normal conductivity is 10 times smaller than in the a - b plane. For other cuprates in the same general class, the anisotropy is even greater and inter plane transport is highly restricted. Furthermore the superconducting length scales show similar anisotropy, the penetration depth ($\lambda_{ab} \approx 150 \text{ nm}$, $\lambda_c \approx 800 \text{ nm}$) and the coherence length, ($\xi_{ab} \approx 2 \text{ nm}$, $\xi_c \approx 0.4 \text{ nm}$). Although the coherence length in the a - b plane is 5 times bigger than that along the c -axis it is quite small compared to classic superconductors such as niobium. ($\xi \approx 40 \text{ nm}$). This means that the superconducting state is more susceptible to local disruptions from interfaces or defects of the order of a single unit cell. This complicates device fabrication. Another difficulty in working with this material is that it readily forms twin boundaries and is easily degraded by water.

2.5.2 MgB₂

The structure of MgB₂ has a hexagonal unit cell, with $a = b = 3.086 \text{ \AA}$ and $c = 3.524 \text{ \AA}$. HCP layers of Magnesium alternate with graphitic Boron layers (Figure 6.2).

In its normal state it is metallic and has a room temperature resistivity of about $5 \mu\Omega\text{cm}$. The T_c of bulk samples is 39 K [35] and has been reported as high as 41 K in thin films [36]. The penetration depth is around 100 nm [36] and like YBa₂Cu₃O_{7- δ} the coherence length is anisotropic. For thin films the coherence lengths were measured to be, $\xi_{ab} \approx 5 \text{ nm}$ and $\xi_c \approx 3 \text{ nm}$ [36]. The higher T_c makes MgB₂ a promising candidate to replace niobium in commercial junction technologies. A recent survey of 235 cryocoolers [37] reveals many potential benefits from MgB₂ devices. For a 300 mW cooler, the input power to the cooler can be up to 100 times less for an MgB₂ device operating at 37 K compared to Niobium at 4.2 K. Furthermore, the cooler mass decreases by 10 times and the cost is halved.

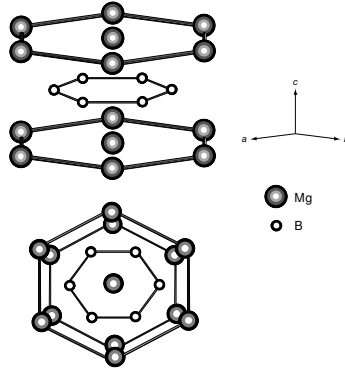


Figure 2.19: Hexagonal structure of MgB₂.

2.5.3 Ion Damage in Superconductors

The superconducting state in some materials is sensitive to disorder which can completely destroy superconductivity. Many experiments in the A15 compounds [38] and high- T_c cuprates [39] involving disorder induced by ion bombardment have provided insight into the mechanisms involved. If the superconducting

pair wave function is written as,

$$\Psi = \delta e^{i\varphi}$$

where δ is the pair amplitude and φ is the phase, it is evident that there are two ways to destroy superconductivity; either by reducing the pair amplitude or destroying the phase coherence. In A15 compounds it is thought that ion damage creates defects that alter the pair density whereas in cuprates the defects affect both the phase coherence and the pair amplitude. In the A15's ion damage decreases the critical temperature until it saturates when the damage level decreases the mean free path to inter-atomic distances [39]. Electron defect scattering lowers the density of states and reduces the pair amplitude which results in the lowering of T_c . In the cuprates there is strong evidence that the mechanism of destruction of the superconducting state is mainly due to defects in the oxygen ordering which create non-superconducting grains that disturb the phase coherence and the pair density [39, 40].

2.5.3.1 Ion Damage in $\text{YBa}_2\text{Cu}_3\text{O}_{7-\delta}$

Many studies of ion damage in $\text{YBa}_2\text{Cu}_3\text{O}_{7-\delta}$ have been carried out over the past 20 years [39, 40]. It has been shown that as dose increases T_c is reduced and resistivity is increased. For high doses, films become highly disordered and insulating and superconductivity is destroyed. Figure 2.20 shows an example of the metal insulator transition of $\text{YBa}_2\text{Cu}_3\text{O}_{7-\delta}$ irradiated with 1 MeV Ne^+ . In this thesis non-hysteretic junctions are created by the selective masking of a bridge of the superconductor and ion damaging the material with a dose that lowers the film's T_c but leaves it metallic.

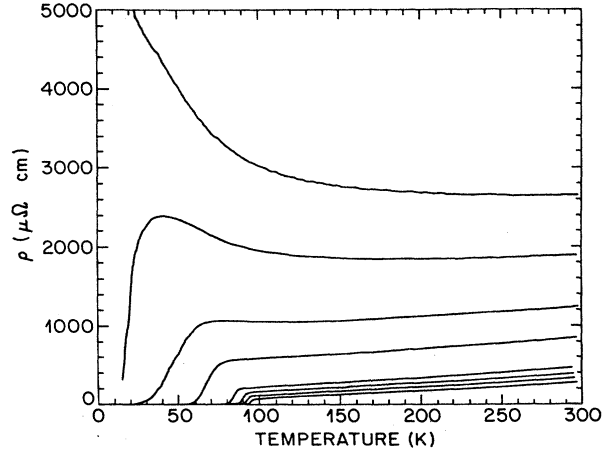


Figure 2.20: Resistivity as a function of temperature for a single $\text{YBa}_2\text{Cu}_3\text{O}_{7-\delta}$ film after bombardment with 1 MeV Ne^+ ions at fluences of (0, 0.1, 2.5, 4.0, 10.0, 15.0, 20.0, and 22.0) $\times 10^{13}$ ions/cm² [40].

2.5.3.2 Ion Damage in MgB_2

A recent study of ion damage in MgB_2 reveals that the mechanism of disorder is similar to that of A15 materials [41]. The pair amplitude is decreased by inter-grain scattering. For high doses T_c is reduced to about 7 K and there is no insulator transition as in the case for $\text{YBa}_2\text{Cu}_3\text{O}_{7-\delta}$. Figure 2.21 shows the results of a sample bombarded with 2 MeV alpha particles. Josephson junctions using this material will also be presented in this thesis.

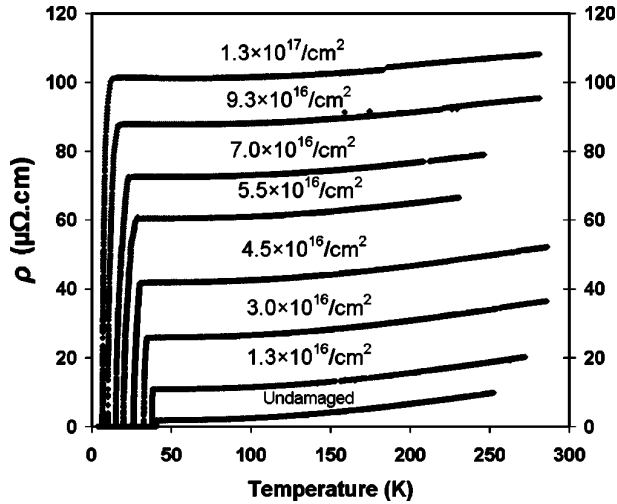


Figure 2.21: Resistivity as a function of temperature for a MgB_2 film bombarded with various fluences of 2 MeV alpha particles [41].

Chapter 3

Device Fabrication

3.1 HTS Thin Films

The majority of the devices studied in this dissertation were fabricated from YBCO thin films. Initially films used were grown in the lab at UCSD using pulsed laser ablation. However since this technique is limited to producing small quantities of samples per growth-run, the source material was changed to commercial films deposited on 2" wafers by thermal co-evaporation. The commercial films proved more economical and more importantly allowed the fabrication of many devices from more uniform material for comparison of other process variables.

$\text{YBa}_2\text{Cu}_3\text{O}_{7-\delta}$ is typically grown with its c -axis normal to the substrate, because quality a -axis films are difficult to grow. To stabilize the superconducting phase, depositions must be carried out at high temperature ($\sim 800^\circ\text{C}$) and high oxygen partial pressure. Optimally doped samples have the highest T_c of about 93 K however these films have rougher surface morphology and create difficulties in device processing. Smoother films have lower T_c between 86 and 91 K.

3.1.1 HTS Substrates

Many factors play a role in choosing a substrate. The substrates must have a small degree of lattice mismatch to prevent defects and cracking from strain.

They must also have a similar thermal expansion coefficient to avoid cracking when samples are cooled. Furthermore a small dielectric constant and loss tangent is desirable to minimize losses and optimize performance when films are used for microwave devices. Dielectric constants between 20 and 25 can be used for devices up to about 10 GHz. For higher frequencies it is not practical to use a dielectric constant above 10 [42].

Table 3.1 shows some of the most common substrates used with $\text{YBa}_2\text{Cu}_3\text{O}_{7-\delta}$. Each has its advantages and disadvantages that need to be taken into consideration based on the application. SrTiO_3 provides a desirable lattice match however it has poor microwave properties, which makes it unusable for RF devices. MgO on the other hand has desirable microwave properties but it has a 9% lattice mismatch and it also reacts with water. LaAlO_3 was a popular substrate in the 90's due to its small 2% lattice mismatch and relatively low dielectric constant, however it readily forms twin boundaries that can transfer into the film and reduce qual-

Table 3.1: Properties of Common HTS Substrates

Substrate	Structure	Mismatch	ϵ	Other
SrTiO_3	cubic $a = 3.90\text{\AA}$	0.5%	300	large ϵ
MgO	cubic $a = 4.21\text{\AA}$	9%	9.6-10	reacts with water
LaAlO_3	rhombohedral $a = 3.79\text{\AA}$ $c = 13.11\text{\AA}$	2%	20.5-27	twinning
Al_2O_3 r-plane	hexagonal $a = 4.76\text{\AA}$ $c = 12.99\text{\AA}$	6%	9.4-11.6	reacts with film
$\text{CeO}_2/\text{Al}_2\text{O}_3$	cubic $a = 5.41\text{\AA}$	0.7%	9.4-11.6	stress cracking
NdGaO_3	orthorhombic $a = 5.43\text{\AA}$ $b = 5.50\text{\AA}$ $c = 7.70\text{\AA}$	0.04%	23	expensive
LSAT	cubic $a = 7.737\text{\AA}$	0%	≈ 22	non-uniform ϵ

ity. R-plane sapphire (Al_2O_3) is inexpensive in comparison to other substrates, and has exceptional microwave properties; however it reacts with $\text{YBa}_2\text{Cu}_3\text{O}_{7-\delta}$ and forms a BaAl_2O_4 interface layer [42]. A solution to this as well as reducing the large mismatch is to deposit a thin CeO_2 buffer layer between the substrate and film. This has become a standard technique for producing commercial films of thicknesses < 350 nm. Thicker films crack from strain. NdGaO_3 is emerging as a favorite substrate due to its small mismatch and ability to grow twin free $\text{YBa}_2\text{Cu}_3\text{O}_{7-\delta}$, however it costs about \$600 per 2" wafer which is about 6 times as much as sapphire. The most unique substrate was developed especially for HTS films at Bell laboratories [43]. It is called LSAT and is a 30/70 mole % solid solution of LaAlO_3 and SrAlTaO_6 . Its lattice parameter can be varied between that of LaAlO_3 7.585 Å (two unit cells) and that of SrAlTaO_6 7.795 Å so it can be used to match a wide variety of HTS compounds. One difficulty with this substrate is that the dielectric constant can vary throughout the substrate.

For this work, the majority of the substrates used were CeO_2 buffered r-plane sapphire. This choice was made to reduce costs and to ensure future devices could be easily incorporated into microstrip transmission lines for RF devices. Sapphire is a hexagonal structure with, $a = 4.759$ Å, and $c = 12.97$ Å. When cut along the $(\bar{1}102)$ plane (r-plane) it has a pseudo-rectangular surface structure. CeO_2 is a cubic structure that grows on the r-plane of sapphire with its principle axes along the $[1\bar{0}11]$ and $[1210]$ directions. The lattice parameter of CeO_2 is 5.41 Å. This is a close match to the $a - b$ plane diagonal of $\text{YBa}_2\text{Cu}_3\text{O}_{7-\delta}$ and encourages growth of c -axis (001) YBCO with the $[110]$ direction along the $[100]$ direction of CeO_2 .

3.1.2 Growth of HTS Materials by Laser Ablation

One of the common techniques for the growth of high temperature superconductors (HTS) is laser ablation; also called pulsed laser deposition (PLD). It has the advantage of allowing deposition in higher background pressures than

other techniques. PLD is also relatively inexpensive and not as complicated as other deposition techniques. The disadvantage is that it is limited to depositing small areas (1cm^2), which can lead to material variations between growth runs. In PLD, a laser is used to ablate a stoichiometric target of the material to be grown. Species are ejected from the target and mix with background gas(es) to form a plasma plume. The species from the plume collect on a substrate attached to a heater placed in the vicinity of the plume for crystal formation.

Films were grown at UCSD using a custom built system set-up by previous graduate students. It consisted of a Lambda Physik Lextra 300 pulsed excimer laser filled with a Kr/F gas mix (which produces a 248 nm wavelength), a large stainless steel cryo-pumped vacuum chamber, a rotating 5 target carousel, and a 2" diameter heater block connected to a programmable temperature controller. Figure 3.1 is a schematic of this system. Substrates were attached to the heater block using silver paint and loaded into the vacuum chamber which was then pumped to its base pressure $\sim 5 \times 10^{-8}$ Torr. The substrate was then heated to 800°C . The gate valve between the pump and the chamber was partially closed and oxygen was introduced through a variable leak valve that was adjusted to maintain a 300 mTorr partial pressure. The beam from the laser was passed through a rectangular aperture to cut off the edges and produce a rectangular beam of uniform energy density (an unperturbed beam has a Gaussian energy distribution). The beam

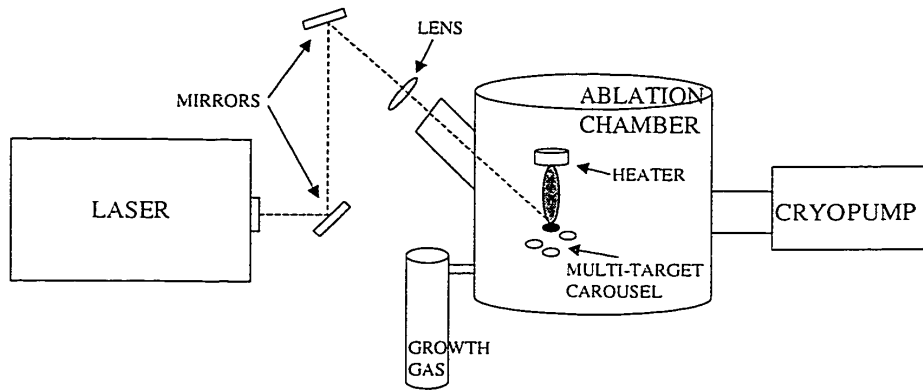


Figure 3.1: Schematic representation of the PLD system used at UCSD.

was then reflected by a mirror upward at 90° to another mirror which reflected it back downward at an angle of 45° where it passed through a lens and a UV transparent viewport of the vacuum chamber where it was focused on the rotating target of $\text{YBa}_2\text{Cu}_3\text{O}_{7-\delta}$. The target was ablated for 2 minutes to clean the surface before deposition. A shutter between the target and sample prevented deposition on the substrate during this stage. With a 1.2 mJ/mm^2 energy density and a 10 Hz duty cycle the growth rate was approximately 100 \AA/min . Following deposition the heater temperature was dropped to 420°C , the gate valve was closed and the oxygen pressure was increased to 350 Torr. The film was annealed in this environment for 1 hr. Modifications were made to this system to include an oxygen nozzle directed at the substrate to increase the oxygen pressure at the substrate, and an off-axis sample holder. Off-axis PLD involves situating the substrate parallel to the length of the plume opposed to directly underneath it (Figure 3.2). This prevents large sticking particles ejected from the target from being included in the film. Films grown by PLD have a spiral growth pattern. During the initial stages of deposition, islands of $\text{YBa}_2\text{Cu}_3\text{O}_{7-\delta}$ form on the substrate. As more material

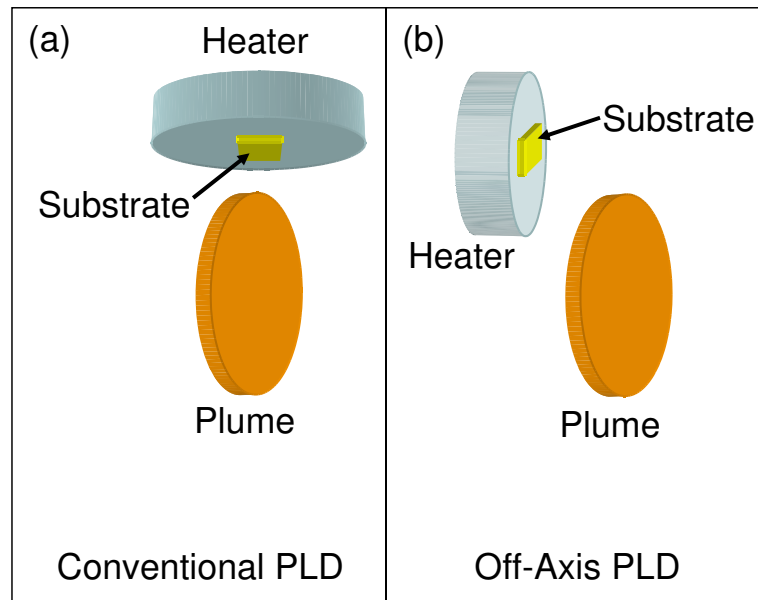


Figure 3.2: Orientation of the sample holder (heater) with respect to the plume for conventional (a) and off-axis PLD (b.)

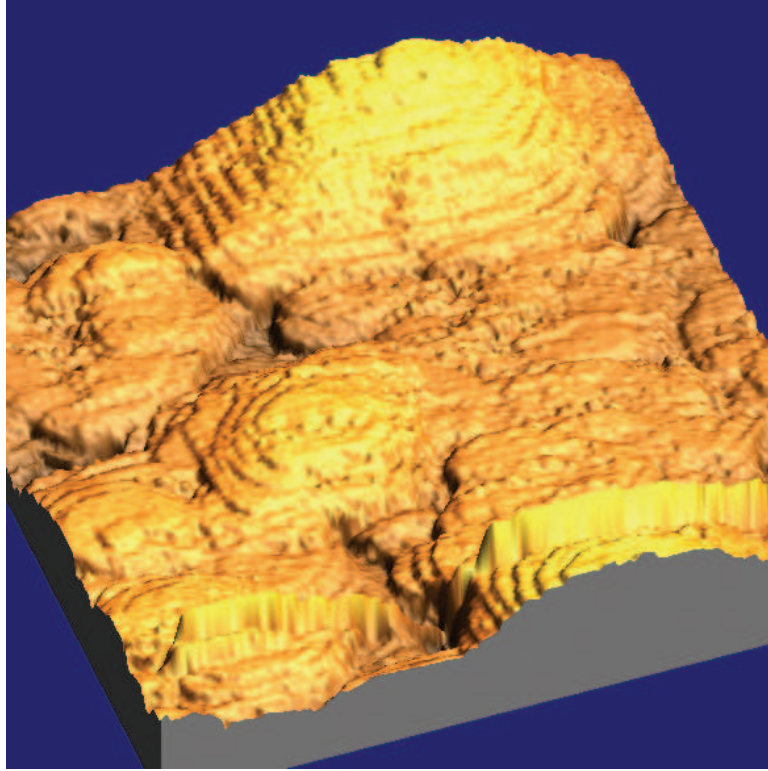


Figure 3.3: $1 \mu\text{m}^2$ STM image of a $\text{YBa}_2\text{Cu}_3\text{O}_{7-\delta}$ film grown by PLD. The growth spirals are visible and the height of the terraces correspond to a single unit cell (11.7 \AA).

is deposited, the islands grow spirally and increase in size until eventually they coalesce and form the contiguous film. Figure 3.3 shows an STM image of a $1 \mu\text{m}^2$ section of an $\text{YBa}_2\text{Cu}_3\text{O}_{7-\delta}$ film grown by PLD at UCSD. The height of the terraces correspond to a single unit cell of YBCO (11.7 \AA) with its c -axis orientated normal to the substrate. Only four $5 \text{ mm} \times 5 \text{ mm}$ films could be produced in a single growth run due to the small area of the plume. This complicated experiments where comparisons were to be made between different samples, because of variations in the material characteristics due to the many process variables. Therefore an alternative source of starting material was pursued.

3.1.3 Thermal Co-Evaporated HTS Thin Films

The majority of the YBCO devices in this dissertation were fabricated from thin films purchased from Theva, a company that specializes in HTS films and tapes [44]. They were prepared using a deposition method called thermal

co-evaporation.

Thermal evaporation is a common technique used for the deposition of metals. It is performed in a vacuum chamber at pressures below 10^{-5} Torr, by passing a current through a coil basket or boat filled with the material to be evaporated. Resistive heating raises the temperature of the material and creates a vapor which collects on the substrate. Compounds can be created by using multiple sources and co-evaporating simultaneously while monitoring the individual rates so that the desired stoichiometry is obtained in the vapor. The high oxygen pressure required to stabilize the superconducting phase of YBCO creates a problem because high pressure in the chamber reduces the mean free path of the species and inhibits deposition. Experiments conducted using RHEED (reflection high energy electron diffraction) revealed that during the growth of YBCO the atoms arriving at the substrate are still mobile on the substrate for a time of the order of 1 sec. after arriving [45]. This allows enough time to shift the substrate to a different environment with higher pressure before the atoms arrive at their resting place. A construct to achieve this is called an oxygen pocket and is depicted in a schematic of a co-evaporation system in Figure 3.4. The main chamber

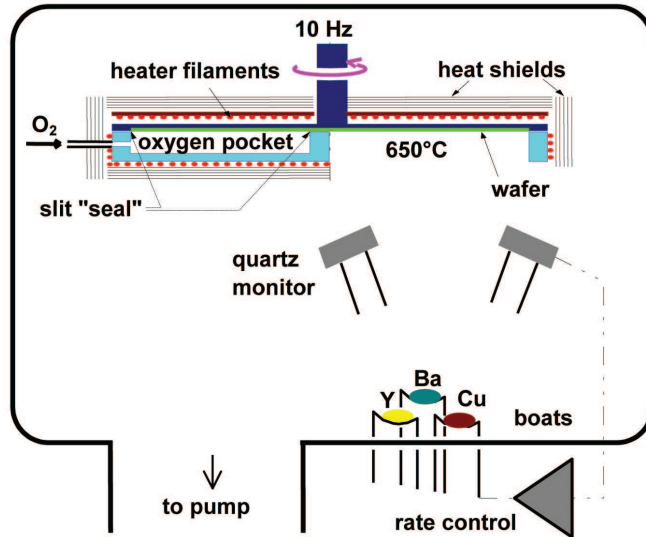


Figure 3.4: Schematic diagram of the Theva thermal co-evaporation system for the deposition of YBCO and other RBCO compounds [44].

is pumped to a pressure of the order of 10^{-5} Torr, oxygen is inlet to a pocket covering half of a rotating substrate platter. The pocket is not perfectly sealed, but a slit with width of 0.5 mm between the pocket edge and holder is sufficient to achieve a partial pressure of 100 mTorr of oxygen inside the pocket region. The three elements are evaporated in the low pressure region and the sample is rotated into the oxygen environment where they mix with oxygen and form $\text{YBa}_2\text{Cu}_3\text{O}_{7-\delta}$. This technique creates high quality large area films. A notable advantage is that the substrate temperature using this technique is over 100° lower than any competing method [46]. The Theva system is also equipped with dc magnetrons for in-situ deposition of metal contacts. It is well documented that immediate subsequent deposition of contact metal reduces the contact resistance from about 10^{-4} to 10^{-8} Ω/cm^2 [47]. Films were grown on 2" wafers with the exception of LSAT substrates which were only available in 30 mm wafers at the time. Table 3.2 shows the different wafers purchased for this thesis work.

Table 3.2: Wafers Purchased From Theva

Film	Substrate	Contact	T_c (K)	J_c (MA/cm ²)
200nm YBCO	LaAlO ₃	200nm Au	86.3	2.2
200nm YBCO	LSAT	200nm Au	86.3	2.2
200nm YBCO	50nm CeO ₂ /Al ₂ O ₃	200nm Au	86.3	2.2
100nm YBCO	50nm CeO ₂ /Al ₂ O ₃	200nm Au	85.7	3.0
100nm NdBCO	50nm CeO ₂ /Al ₂ O ₃	200nm Au	86.5	0.8
100nm YBCO	50nm CeO ₂ /Al ₂ O ₃	200nm Au	85.0	2.1
75nm YBCO	50nm CeO ₂ /Al ₂ O ₃	10nm Ag	85.4	2.4
50nm YBCO	50nm CeO ₂ /Al ₂ O ₃	10nm Ag	81.0	0.7

3.1.3.1 Film Morphology

By varying deposition conditions Theva can control the morphology of the films and they are classified into three types; M-type for microwave filters or high current applications, S-type for SQUIDs and devices, and E-type for finely patterned electronics (Figure 3.5). All of the films used in this thesis were of E-type and guaranteed to have a T_c greater than 77 K, no scratches or line defects, no

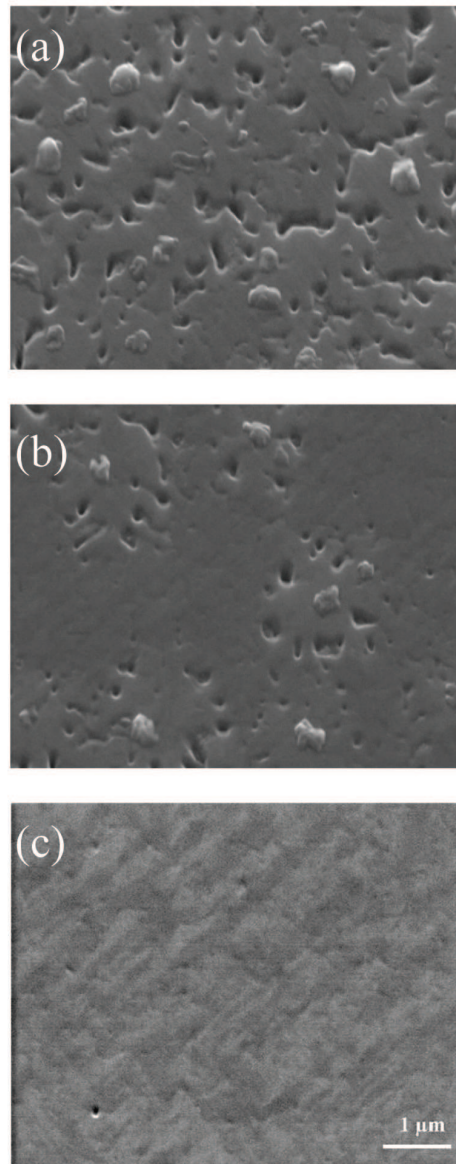


Figure 3.5: SEM pictures of the different grades of YBCO films, (a) M-type, (b) S-type, and (c) E-type [44].

sticking particles or point defects $> 25 \mu\text{m}$, and to be $< 2\%$ a -axis by volume. With the exception of $\text{NdBa}_2\text{Cu}_3\text{O}_{7-\delta}$ (NdBCO) all of the wafers purchased exceeded these conditions. The films grown by Theva are guaranteed to have an average surface roughness between 6-10 nm. Figure 3.6 is an AFM image of a 600 nm thick $\text{YBa}_2\text{Cu}_3\text{O}_{7-\delta}$ film on MgO substrate, and a RMS surface roughness plot.

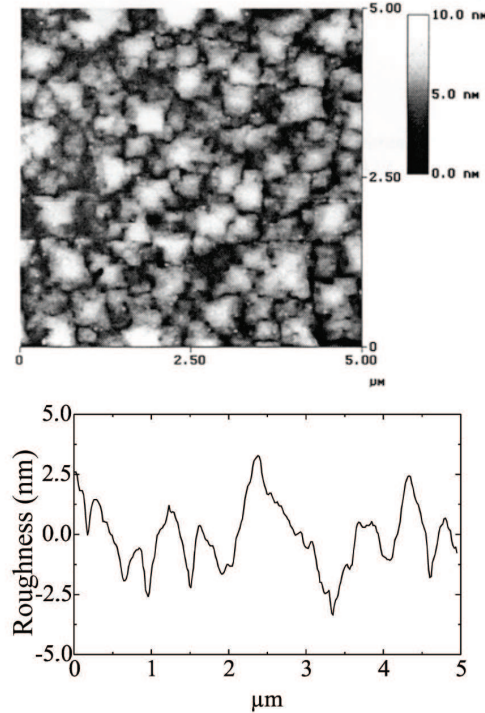


Figure 3.6: (a) AFM image of a 600 nm YBCO film on MgO, (b) average surface roughness of the same film [44].

3.1.3.2 Electrical Transport Properties

A Cryoscan of a 100 nm YBCO wafer on buffered sapphire is shown in Figure 3.7. A Cryoscan is an inductive non-destructive mapping of the critical current density [44]. The wafer is cooled below T_c and an ac probe signal is increased until it exceeds the critical current of the film resulting in a distortion of the reflected signal. This response is then calibrated with a known J_c . This provides a useful tool for determining the uniformity of the superconducting properties of a film throughout a wafer.

The electrical transport properties of these materials were determined by the photolithographic patterning of a 4-point bridge and measuring the resistance as a function of temperature. This will be explained in detail in later sections. From this measurement resistivity can be calculated using the bridge geometry. The y-intercept from a linear fit of the data above the transition is how the residual

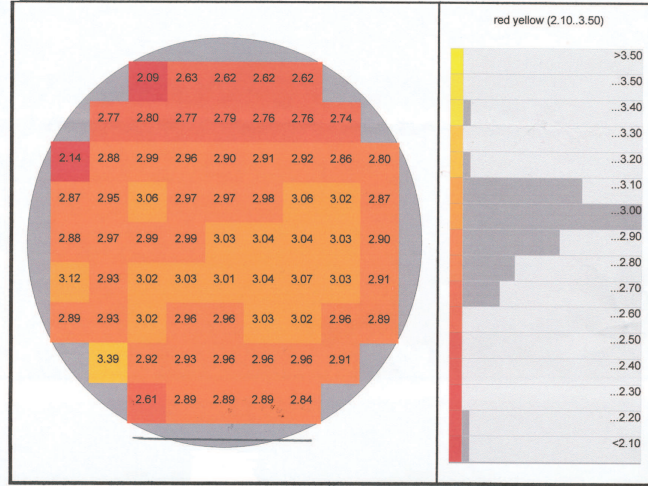


Figure 3.7: Cryoscan for a 2'' wafer of 100 nm $\text{YBa}_2\text{Cu}_3\text{O}_{7-\delta}/\text{CeO}_2/\text{Al}_2\text{O}_3$, depicting the critical current density in units of MA/cm^2 for $5 \times 5 \text{ mm}^2$ regions.

resistivity was determined, (ρ_0). This provides information about the quality of the normal conductivity. The width of the superconducting transition provides a measure of the distribution of the critical temperatures throughout the bridge. A wide transition can be attributed to inhomogeneous material with regions of different T_c . Furthermore, the temperature dependent resistivity is different for the Cu-O chains along the b -axis (ρ_b) then the Cu-O planes along the a -axis (ρ_a). Measurements in de-twinned single crystals [48] reveal that ρ_0 has a T^2 dependence while ρ_a is linear with T . Furthermore ρ_a is of the order of $300 \mu\Omega\text{-cm}$ at room temperature with ρ_{0a} near 0, while ρ_b is 3 times less and ρ_{0b} can be as large as $100 \mu\Omega\text{-cm}$. Most films contain grains of both a and b axis orientation with respect to the current flow, thus they have resistivity characteristics that are a mix between these two extremes.

Figure 3.8 shows a typical result for a Theva $\text{YBa}_2\text{Cu}_3\text{O}_{7-\delta}$ film. The data show a mix between a and b axis transport. The small width of the superconducting transition infers that the material is homogeneous and doesn't contain mixed phases. Figure 3.9 shows the results from a NdBCO film. The non-linear behavior in the normal region and high resistivity indicate poor quality material and the large transition width of 5 K indicates that there are mixed phases with

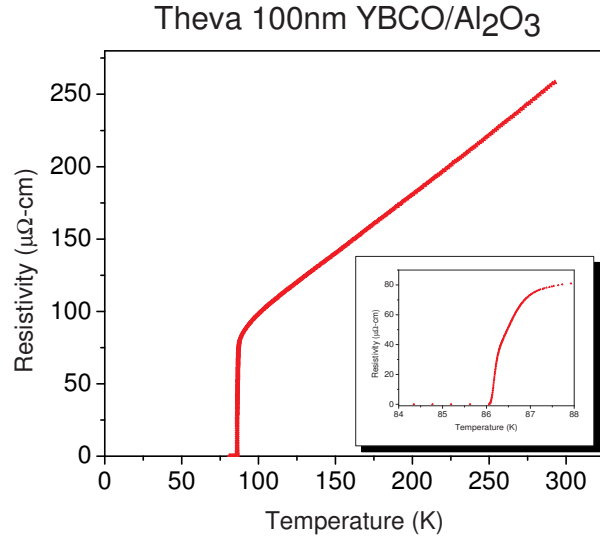


Figure 3.8: Resistance vs. temperature measurement of a Theva co-evaporated 100 nm thick YBCO thin film on CeO_2 buffered r-plane sapphire substrate. The T_c of this film is 86 K and the residual resistivity is $17 \mu\Omega\text{cm}$. The inset shows the transition width to be about 0.5 K.

variation of critical temperature. To rule out processing damage, measurements were repeated using a simple 4-point VanderPaaws resistance measurement without removing the *in-situ* contact. The T_c and transition width was identical to the patterned bridge.

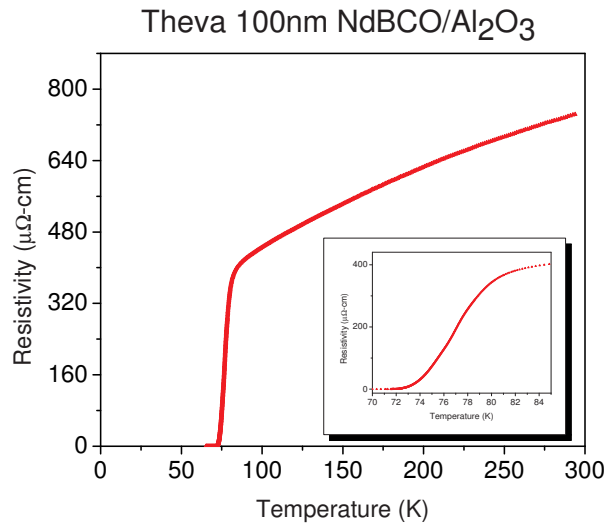


Figure 3.9: Resistance vs. temperature measurement of a Theva co-evaporated 100 nm thick NdBCO thin film on CeO_2 buffered r-plane sapphire substrate. The T_c of this film is 71 K and the residual resistivity is approximately $300 \mu\Omega\text{cm}$. The inset shows the transition width to be about 5 K.

3.2 MgB₂ Thin Films Grown by HPCVD

Early thin films of MgB₂ were grown in a two step process where Boron films were annealed in a magnesium rich environment. This technique produced low quality films with reduced transition temperatures and rough surfaces. A thermodynamic study showed that high magnesium pressures were necessary to stabilize the desired phase at high temperatures [49].

These pressures are too high for most conventional deposition techniques. Researchers at Penn State University developed a new method to address this problem called hybrid physical-chemical vapor deposition (HPCVD), a combination of physical and chemical vapor deposition [50]. Diborane gas (B₂H₆) is used as the precursor gas and thermally evaporated bulk Mg is used as the Magnesium source. The sample is placed on a susceptor along with pieces of magnesium which are inductively heated to a temperature between 730°C and 760°C. The susceptor is orientated coaxially with a vertical quartz reactor tube where the B₂H₆ is introduced. The total pressure is maintained between 100-700 Torr. This arrangement creates a high partial pressure of Mg near the substrate and results in high quality MgB₂ films. Figure 3.10 shows SEM pictures of the surface of films grown on sapphire and SiC substrates [50]. The SiC substrates produce smoother films. The surface roughness of the SiC films are ~ 2.5 nm as opposed to ~ 4 nm for sapphire. The films grow in hexagonal columns that are typically larger than 100 nm across. Figure 3.11 is a $5 \times 5 \mu\text{m}^2$ AFM scan of an MgB₂ film on SiC. The hexagonal

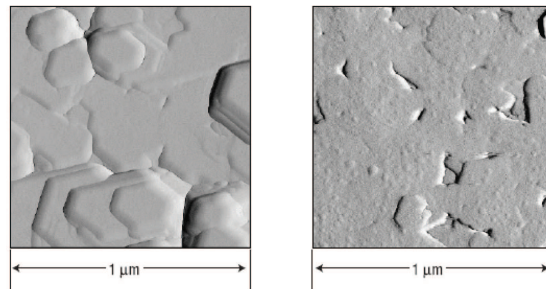


Figure 3.10: SEM pictures of MgB₂ films grown on sapphire (left) and SiC (right), both feature hexagonal growth columns [50].

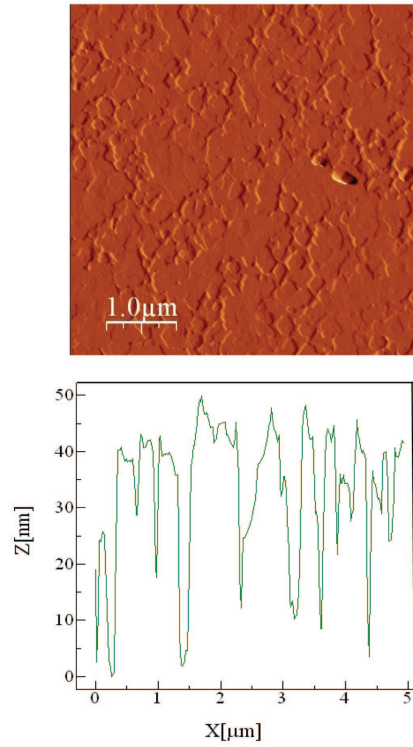


Figure 3.11: AFM picture of an MgB_2 films grown on SiC and a surface profile of the same film [50].

growth columns are visible and the profile shows that their heights are between about 10 and 40 nm. Figure 3.12 shows electrical transport characteristics for an MgB_2 film measured at Penn State. The resistivity shows a parabolic temperature dependence and is over an order of magnitude smaller than that of $\text{YBa}_2\text{Cu}_3\text{O}_{7-\delta}$. The narrow transition width (inset) indicates that the material is homogenous.

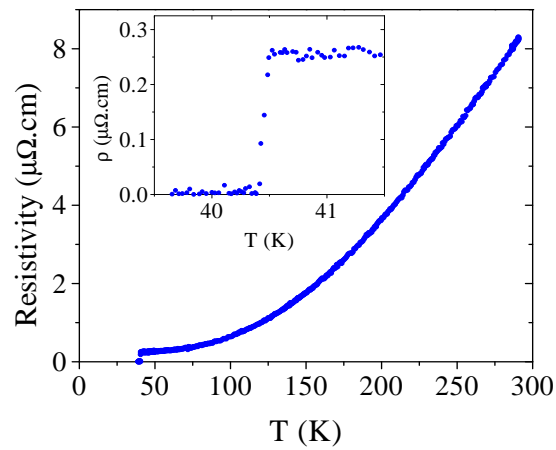


Figure 3.12: Temperature dependence of the resistivity of an MgB_2 film.

3.3 Mask Design

The superconducting films were patterned with photolithography to create contacts, electrodes, and alignment marks for electron beam lithography (EBL). Figure 3.13 shows one of the masks designed for the superconducting layer. The light lines (green) are alignment marks for electron beam lithography and the dark lines (blue) are part of the circuit. This particular pattern has 16 individual $4\ \mu\text{m}$ wide bridges for 4-point measurements. Two contact pads are common for all bridges, V^- and I^- . Each bridge also has 2 unique additional terminals referred to as V^+ and I^+ . One feature unique to this mask is that all of the devices for the chip are contained in a $90 \times 90\ \mu\text{m}^2$ area in the center of the chip. This is the field of view that our EBL system can write without having to be refocused or have the substrate stepped.

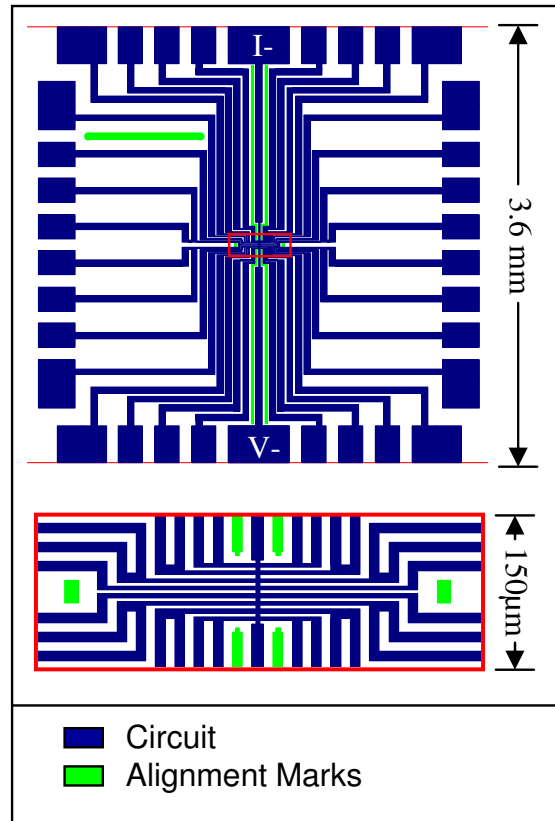


Figure 3.13: Sixteen bridge photolithographic graph mask dark lines(blue) represent the circuit areas and light lines(green) are EBL alignment marks. 16 bridges are located within a $90\ \mu\text{m} \times 90\ \mu\text{m}$ central region of the mask.

3.4 Pattern Photolithography

Wafers were diced by Theva into 5x5 mm² samples. They were spin-coated with a 1.8 μm layer of Shipley 1818 positive photoresist spun at 4000 rpm for 30 s. Samples were then soft-baked on a hotplate at 90°C for 2 minutes to remove the solvent from the resist. After baking, samples were first exposed for 1 min at 12.5 mW/cm² in a JBA contact mask aligner using a solid 3.6 mm x 3.6 mm square that covered the resist in the center but left the edges exposed. Samples were developed in Shipley MF-319 until the resist on the edges was gone. This step was essential because the resist on the edges of the samples was much thicker than in the center, which prevented good contact at the essential circuit areas in the center of the sample. The pattern was then exposed using a chrome-on-quartz mask with a 0.25 μm tolerance for 18 s at 12 mW/cm². Exposed samples were developed for approximately 18 s in Shipley MF-319 developer. Samples were agitated during development to ensure that resist coming off the sample did not remain near the pattern which can prevent development of some areas. Samples were rinsed in deionized water to stop the development and then blown dried with compressed nitrogen. The Patterns were examined with an optical microscope to ensure there were no defects or resist remaining to be developed. After inspection samples were placed on a hot plate and hard-baked at 120°C for 5 minutes to cross link the polymers in the resist and make it more resistant to ion-milling.

3.5 Argon Ion Milling

Argon ion mill dry etching has become the standard way to pattern HTS samples. It involves subjecting the sample to an energetic beam of ions that physically sputters the atoms off of the material being etched. A discharge from a tungsten filament ionizes atoms in the surrounding gases and creates a plasma. The ions in the plasma are accelerated and focused using two grids placed above the discharge. A potential difference is applied between the grids which cause the

ions to accelerate from the lower to the upper grid. Upon reaching the upper grid the ions pass through the holes in it and exit the source.

A custom built cryogenic ion milling system consisting of a diffusion pumped bell jar, a 3.5 cm Kaufmann ion source, Commonwealth Scientific ID 2500 ion drive, and a liquid nitrogen cooled sample holder was used. Samples were then attached to a copper plate with Dow-Corning vacuum grease and loaded into the bell jar. The chamber and gas lines were pumped to 2×10^{-6} Torr, and then liquid nitrogen from a pressurized Dewar was forced through a coil of copper tubing attached to the sample holder. After the sample holder was cooled to 77 K, argon gas was introduced into the chamber through a variable leak valve and the pressure was adjusted to be 2.5×10^{-4} Torr. The ion mill power supply was then turned on and ran in auto mode with the acceleration voltage set to 400 V with a beam current of 5 mA. This etched $\text{YBa}_2\text{Cu}_3\text{O}_{7-\delta}$ at 75 Å/min and gold at 400 Å/min. The cryogenic cooling helps protect the superconductor from heating that would result in oxygen loss and it also creates steeper edges. After ion milling, the resist was removed using acetone and ultrasound, followed by a rinse in isopropyl alcohol and then blown-dry with compressed nitrogen

3.6 Lift-off and Gold Removal

Another photolithographic step followed ion milling to create metallic contacts. Two different processes were followed depending on whether the sample already had a contact layer deposited in-situ or whether it was a bare film requiring metallization. Samples requiring contacts were coated with resist as described in section 3.4. A mask of the contact pads was aligned to the sample and exposed for 22 s at 12 mW/cm^2 . After exposure they were then soaked in toluene or chlorobenzene for 60 s. This slows down the development of the resist on the surface and creates an overhang feature (Figure 3.14). This feature prevents contacts from pulling off during resist lift-off, by ensuring the metal is discontinuous at the edges.

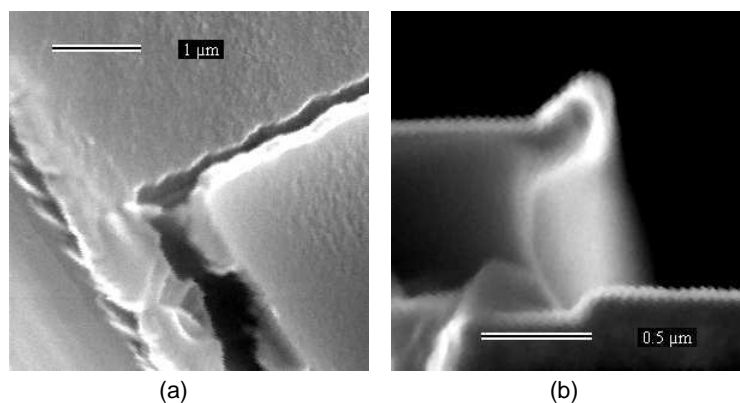


Figure 3.14: (a) Ge film evaporated on top of a lift-off overhang created using a chlorobenzene soak. The film is discontinuous at the resist edge preventing it from being pulled off when the resist is removed. (b) Cross-section showing the extent of the overhang.

After development the sample was ashed in oxygen plasma in a Technics 500 II asher at 200 W for 30 s at a pressure of 200 mTorr. This descums the surface and improves contact adhesion. After ashing, a layer of gold was deposited via dc sputtering in a Denton Discovery 18 sputtering system. Then the underlying resist was removed using acetone and ultrasound.

For samples already having a contact layer deposited in-situ, the metal over the center of the sample had to be removed. This was done by exposing and developing a $500 \times 100 \mu\text{m}^2$ area over the 16 bridge region (Figure 3.15). Following development, $\text{YBa}_2\text{Cu}_3\text{O}_{7-\delta}$ samples were etched in NaI/I^+ filtered semiconductor grade gold etch for 45 s and rinsed in isopropyl alcohol. Cryogenic ion milling for 5 minutes was used for MgB_2 samples because the gold etch degraded the films.

Fabricating contact layers using this technique was superior to the lift-off contacts for many reasons. Having a noble metal covering the superconductor in the early processing steps prevents degradation from contact with water and process chemicals. It also protects from any thermal damage inflicted by the ion mill. It lowers the contact resistance over 4 orders of magnitude and substantially improves contact adhesion

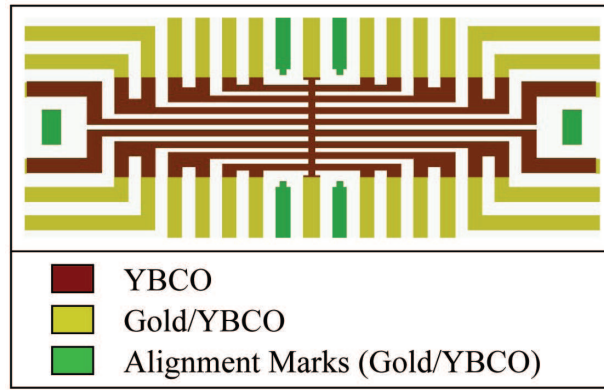


Figure 3.15: Central region of the sixteen bridge photolithographic graph mask dark lines showing the region where the contact was removed via chemical or dry etching.

3.7 Tri-layer Structure

The junctions were defined in the bridges by using electron beam lithography and ion damage. Electron beam resist is not thick enough to serve as an implantation mask so the EBL pattern was transferred into a layer of germanium and photoresist. Samples were cleaned in isopropyl and dried in nitrogen prior to the creation of a tri-layer structure. (Figure 3.16). They were spin-coated with

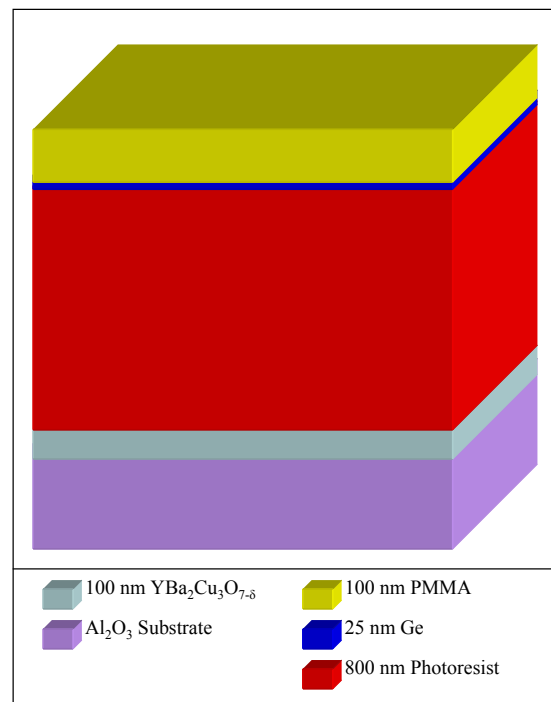


Figure 3.16: Cross-section showing the components of the tri-layer implant mask.

an 800 nm thick layer of Shipley S1808 photoresist spun at 4000 rpm for 60 s, followed by a hard-bake on a hot plate for 10 minutes at 130°C. This was followed by thermal evaporation of a 25 nm thick layer of amorphous germanium. A 100 nm layer of electron beam resist, 2% polymethylmethacrylate (PMMA) in chlorobenzene was spin-coated on top of the Ge at 4000 rpm for 60 s. The sample was then baked again on the hot plate at 125°C for 10 minutes. It was important for the temperature of the second bake to be lower than that of the first, otherwise the underlying photoresist would contract and crack the germanium layer as shown in Figure 3.17.

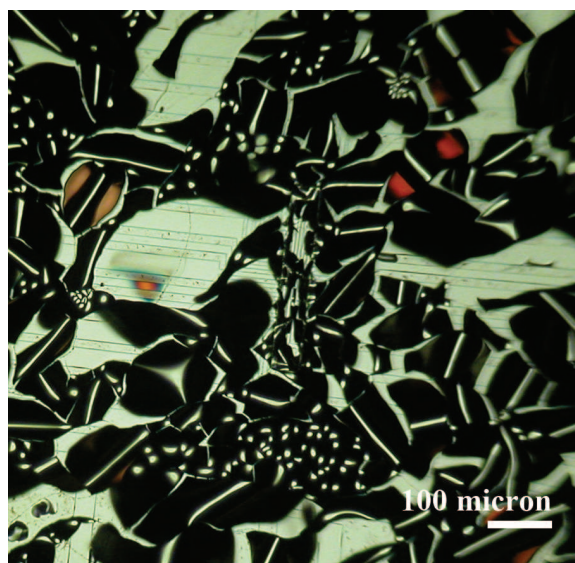


Figure 3.17: Microscope picture showing a cracked tri-layer mask. The circuit pattern is visible underneath the cracked resist/Ge layers.

3.8 Electron Beam Lithography

For positive electron beam lithography a resist, such as PMMA, consisting of long molecular chains is exposed to an electron beam that breaks many bonds in the chains. Shorter chains are more soluble in developer than unbroken chains. The dose of electrons required to break enough chains to make the exposed area more soluble is called the threshold level of the resist. Thus by optimizing the resist with the proper dose of electrons and developer, fine lithography can be

performed. Features of the order of 10 nm can be readily obtained in PMMA using commercial high voltage lithography systems.

For this thesis work electron beam lithography was performed on a JEOL JSM-6400 scanning electron microscope equipped with Nanometer Pattern Generation System (NPGS) to modify it for lithography [51]. It was also equipped with an electrostatic beam blanker which consisted of two plates in the column that the beam passed through. A potential applied across the plates deflects the beam so it misses the aperture and prevents the beam from reaching the sample. This can be used to prevent exposure of critical areas while performing lithography. Patterns to be written are drawn in a CAD program (DesignCad) and the writing conditions such as dose are entered into a run file that controls the $x - y$ scan coils of the SEM using a 5 MHz, 16 bit digital-to-analog-converter (DAC). The coils are not scanned continuously due to the nature of the digitized signal from the DAC card. The beam is stepped point by point (1.37 nm between points at 1000X magnification) and NPGS controls the dwell time at each point to control the dose. The dwell time can be as short as $0.2 \mu\text{s}$. A short dwell time and high current is desirable so that the writing can be done fast to eliminate 60 Hz environmental noise that can create wavy lines (Figure 3.18).

Samples were mounted to the specimen holder using carbon double-sided

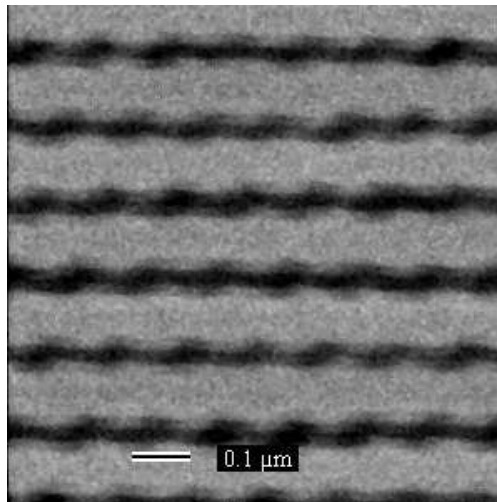


Figure 3.18: The effect of 60 Hz environmental noise on lines written with EBL.

adhesive tape. The surface was then grounded to the holder by using a drop of silver paint on the corners. This prevented the surface from charging. The sample was loaded into the SEM column and pumped to 3×10^{-6} Torr and moved from underneath the center of the beam to prevent accidental exposure. The aperture was set to the smallest and the working distance was set to 8 mm. The operating voltage was turned on and set to 36 kV. The filament current was increased slowly while looking, in line mode, at a grid or edge of the sample (away from the circuit area). This allowed for finding the maximum or saturation current of the filament. Right below this maximum the filament is the most stable.

Due to diffraction by apertures, the distribution of the electron beam in the $x-y$ plane is a set of coaxial circles, only the center peak is the maximum (brightest). This was typically centered, but sometimes x and y tilt/shift had to be adjusted to find the optimum condition; condenser lens (CL) rough 14, fine 100, with a current reading of 8 pA. The beam current was set to CL rough 12 or higher and magnification was set to 200X. A probe current detector (PCD) was equipped in the SEM for measuring the beam current. It was a pneumatically activated faraday cup which could be moved into the path of the beam to collect the current. It was used to set the desired current. Typically these CL settings (rough, fine) produced the following currents: (14, 100), 8 pA, (13, 100), 13 pA, (12, 100), 27 pA, (11, 100), 67 pA and (10, 100), 113 pA. The beam current determines the line width written in the resist so the beam current was routinely checked for stability to ensure uniform line widths.

The sample edge was carefully moved into view. And magnification was increased to 1000X. The silver paint on the corner was located and a particle with size of less than $1 \mu\text{m}$ and with good contrast was used as a specimen to further adjust the SEM for centering and stigmatism. Stigmatism happens when the objective lens has two different focus lengths in the x and y directions. Astigmatism lenses are used to correct this aberration. Adjusting x -astig, y -astig, and focus, the stigmatism can be decreased to a minimum. The ultimate goal is to have no

directional image blur when focusing and defocusing the specimen. The wobbler, a function that changes the focus in and out was then turned on. It was used to assist in centering the beam in the aperture. With the wobbler on, the image may move periodically in one direction. The x and/or y knobs on the aperture stub on the column were used to minimize the motion. If the aperture is centered well, the image will not move. Precise adjustment of astigmatism and wobbling require higher magnification so this process can be repeated at higher magnification for further optimization. Astigmatism is not independent of focal length. If the focal length changes astigmatism readjustment is necessary. Therefore, level samples are preferred so that it is not necessary to change astigmatism at different areas of the pattern.

To check that the SEM was properly adjusted it was tested on a non-essential region of the resist. Using the maximum magnification (300,000X), and the beam current at which the sample is to be exposed, a hole was burnt in the PMMA in point scan mode. This hole shown in Figure 3.19 appeared as a dark spot surrounded by a bright halo. During burning, the absolute value of the current shown on the specimen current meter decreased monotonically which signifies the area has been burnt and is becoming brighter and brighter. When no indication of such decreasing happened, it indicated bad focus or wrong astigmatism. Adjusting the fine focus, while burning was sometimes all that was needed, otherwise astigmatism had to be readjusted. When focus and astigmatism are both perfect, a halo can be burnt in less than 5 seconds. In image mode the halo can be used as a small visible object to help further adjust focus and astigmatism. It also assures that the focus and astigmatism are correct. The PMMA at the center of the hole is usually changed from “positive” to “negative” resist due to cross-linking of their polymers from the elevated dose. This feature can be used in developing and RIE to verify processing times. Due to backscattering, electrons are not only located at the halo; they can expose a range of tens of microns depending on the exposure time so it must not be too close to the significant parts of the sample.

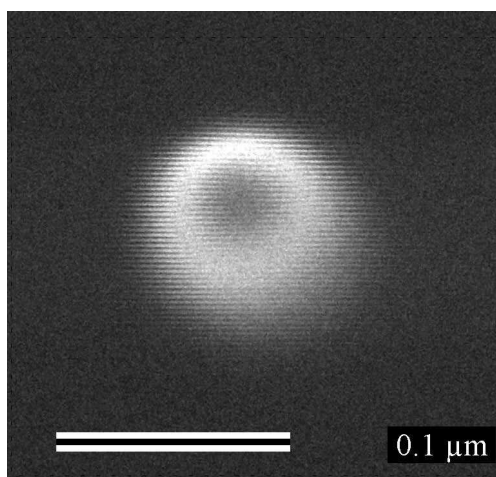


Figure 3.19: Hole burned in the PMMA layer in point scan mode to test and adjust the focus and astigmatism.

With the beam optimized the sample was ready to be positioned for writing. One of the 4 alignment bars next to the common electrodes (V^- , I^-) of the photolithographic pattern (Figure 3.13) was located. Magnification was increased so that the bar filled the whole field of view (10,000X). This limited exposure to the resist directly above the bar and prevented exposure where the pattern was to be written. The sample was then moved into position by following the bar into the center. At the end of the alignment bar another hole was burnt in the PMMA to adjust focus.

The beam was then blanked, and the scan coils were placed under the control of the NPGS. Magnification was changed to 1000X which has a $90\ \mu\text{m} \times 90\ \mu\text{m}$ field of view. A program for alignment was then executed. The program scans 4 rectangular regions on the outside of the pattern without exposing the center. The rectangles are then moved to correspond to the ends of the 4 alignment bars on the sample. The program then calculates a transformation matrix to correct any x and y error. After alignment is complete the run file is called and the DesignCad pattern is written. Typical run files were sets of lines used to define the junction barriers. A single line would cross 8 of the 16 bridges. Figure 3.20 shows the pattern written for 5-junction arrays.

Exposed samples were then developed for 35 s in 1:3 Methyl Isobutyl

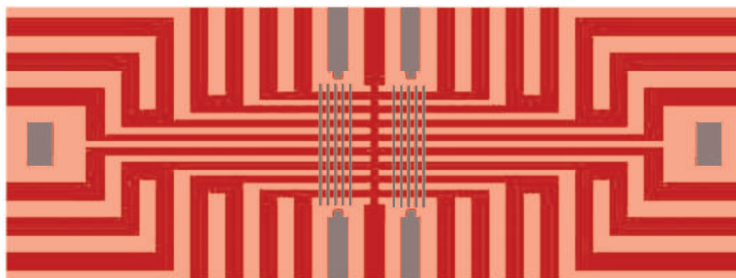


Figure 3.20: Central region of the 16-Bridge mask showing 5 lines (junctions) scribed across each bridge.

Ketone in Isopropyl Alcohol (MIBK/IPA). During development the sample was agitated gently to promote removal of the exposed region. After development samples were rinsed in isopropyl and blown dried with compressed nitrogen.

Using a 20 pA beam current line doses between 3-8 nC/cm were used to create line widths ranging between 30-100 nm. The dose required to generate a desired line width varied between samples and had to be optimized.

3.9 Reactive Ion Etching

Reactive ion etching is a common etching technique used in microelectronics processing. It combines physical sputtering and chemical etching and can be used to anisotropically etch many materials. A plasma discharge is created in the presence of a low pressure gas. The species in the gas disassociate in the plasma and form chemically reactive radicals. They are accelerated to the target where they interact chemically to form gas molecules with the target atoms that are then pumped away. The acceleration makes the etch highly directional. Choosing a gas whose radicals react with the target but not the mask results in a highly anisotropic etch capable of producing nearly vertical sidewalls.

Developed samples were loaded into a Plasma Science table top, parallel plate reactive ion etcher (RIE). This system had a turbo pumped 8" diameter cylindrical quartz chamber. Inside were a set of 6" circular plates with $2\frac{1}{2}$ " spacing. The lower plate was cooled with chilled water. The chamber was equipped with two process gas lines, each terminating with a needle valve inline with a shut off

valve to control the gas flow. One line could be used to introduce either Argon or Oxygen and the other was used for CCl_2F_2 , CF_3H , CCl_3F , SF_6 or CF_4 . A 300 W 13.56 MHz RF power was used to generate the plasma and a manual matching network was used to match the impedance of the plasma to the power supply.

The pattern from the PMMA was transferred into the Ge using a CCl_2F_2 plasma. The gas pressure was maintained at 14 mTorr, and the dc self bias at 200 V. The forward power resulting was 20 W. The matching network was adjusted so that the power reflected was 0 W. This etched the Ge at about 15 nm/min and the PMMA at about 30 nm/min. Etching was performed for 2 min. to ensure the 25 nm layer was completely etched. Although the selectivity between PMMA and Ge was not very good for this etch the thickness of the PMMA was sufficient to transfer the pattern without broadening of the features. The chamber was pumped back out to its base pressure and the sample was then etched in Oxygen plasma. The gas pressure was maintained at 5 mTorr, and the dc self bias at 300 V. The forward power resulting was 28 W. This etched the photoresist at 50 nm/min. The sample was over etched for 1 min to ensure that the layer was completely etched. This etch also removed the PMMA layer but had no effect on Ge or YBCO.

It was essential to clean and condition the chamber thoroughly prior to etching, otherwise “grass” would be left on the surface of the sample (Figure 3.21). Grass occurs when etched material recombines with impurities and redeposits on the sample. The quartz chamber was cleaned with 2% HF in deionized water. Then an Oxygen plasma at 40 mTorr, 600 V (40 W) was used for 20 minutes. This was followed by a CCl_2F_2 plasma with the same conditions as the Ge etch. No grass was visible after following this procedure. Etched samples were examined under the SEM with care taken not to observe regions directly above the YBCO bridges, because prolonged observation locally heated the resist causing it to contract, widening the lines. Line widths were measured and recorded.

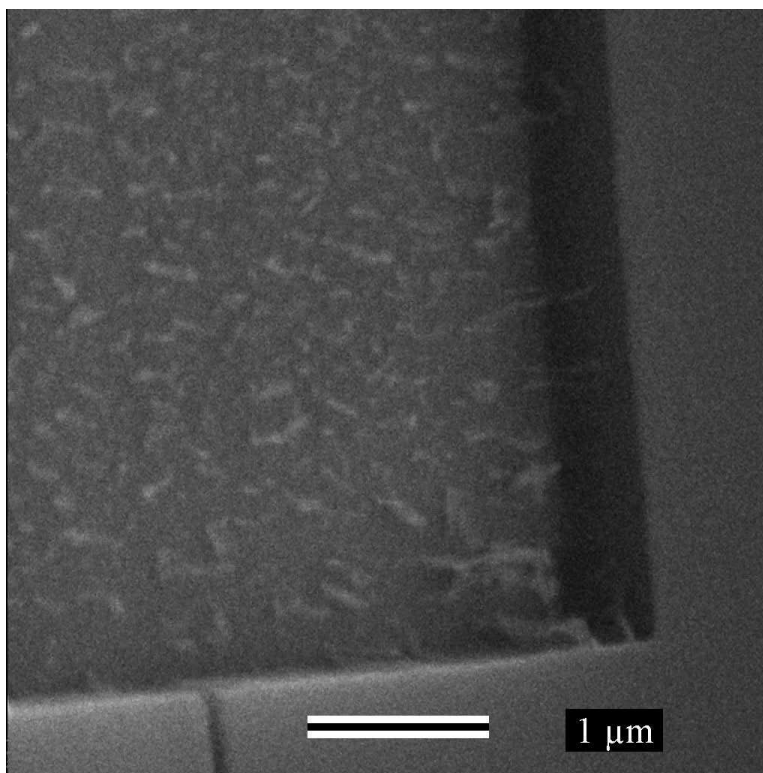


Figure 3.21: Grass after RIE etching of the tri-layer.

3.10 Ion Damage

To create the actual junction the masked bridges were bombarded with ions in an ion implanter. The ion energy was balanced so that it was high enough to penetrate the whole thickness of the unmasked YBCO film to create uniform damage, but not high enough to penetrate the Ge/Resist mask and damage the electrodes. Building on previous work the majority of the samples were implanted with 200 keV Neon with doses ranging between (5×10^{12} - 3×10^{13} ions/cm²).

Etched samples were attached to a 4" wafer with silver paint and sent to a company for ion implantation (Core Systems) [52]. To limit charging the surface of the sample, it was grounded to the wafer with silver paint. To prevent ion channeling along the *c*-axis of the crystal, samples were tilted at 7° (Figure 3.22). Channeling limits the amount of damage because the ions can travel very far through the sample before experiencing a collision. Because of the high aspect ratio of our mask it was important to ensure that the tilt angle was along the slits

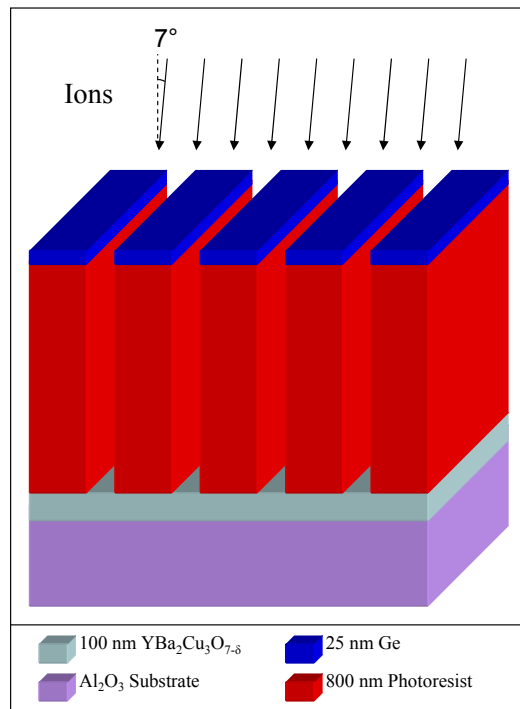


Figure 3.22: Etched tri-layer mask depicting the 7° tilt used to prevent channeling.

used to define the junctions. Any misalignment would create a shadow and result in reduced or no damage depending on the level of misorientation. A 4" copper wafer was machined with a 7° inclined ramp in the center (Figure 3.23). This allows us to align the sample with regard to the tilt rather than relying on the technicians at the company. The company could then implant with any rotation at a 0° wafer tilt and the lines were always 7° to the ion beam. The machine used

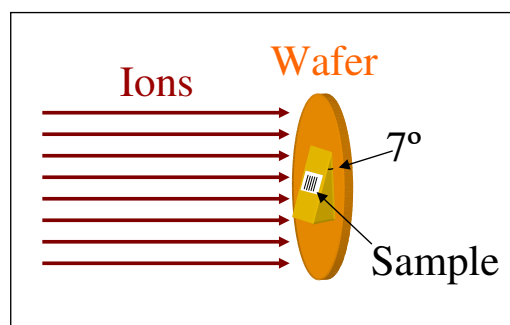


Figure 3.23: Sample holder designed to prevent misalignment. The center of the wafer contains a ramp with a 7° tilt. The lines scribed by EBL are aligned parallel with the ramp and the wafer is implanted at 0°.

was a Varian CF 3030 implanter. The ion beam was electrostatically scanned. The horizontal and vertical scan rates were 256 Hz and 2.250 KHz respectively. The machine scans an area of a 4" wafer plus a $\frac{1}{2}$ " of over scan to ensure uniform implantation. Uniformity studies by Core show the uniformity of the implant to be between 0.5-1.0%. Table 3.3 shows the different implantations performed. Most of the implantations were 200 keV Ne, however Ag was also attempted. The current is the beam current used over an area of a 4" wafer. Holding dose constant a decrease in current increases implantation time. This was varied to investigate the possibility of charging effects.

Table 3.3: Implantations

Energy(keV)	Ion	Dose($\frac{\text{ions}}{\text{cm}^2}$)	Current(μA)
100	Ne	1.0×10^{13}	1.2
200	Ne	5.0×10^{12}	1.0
200	Ne	1.0×10^{13}	0.12
200	Ne	1.0×10^{13}	0.5
200	Ne	1.0×10^{13}	1.0
200	Ne	1.0×10^{13}	1.2
200	Ne	1.5×10^{13}	0.5
200	Ne	1.5×10^{13}	1.0
200	Ne	2.0×10^{13}	0.5
200	Ne	2.0×10^{13}	1.0
200	Ne	3.0×10^{13}	1.0
400	Ag	1.0×10^{11}	0.32
400	Ag	1.0×10^{12}	1.0
400	Ag	1.0×10^{13}	1.0

3.10.1 Simulations

Simulations were performed using SRIM 2003 (Stopping and Range of Ions in Matter) to help optimize the implantation process [53]. SRIM is a freeware program used in ion implantation to calculate the stopping and range of ions in matter using a quantum mechanical treatment of ion-atom collisions. SRIM simulations showed that for a 200 keV Ne⁺ implantation the ions are energetic enough to penetrate an unmasked 200 nm thick YBCO film (junction barriers) and

that the Ge/photoresist mask was of sufficient density to stop ions from damaging the electrodes (areas underneath the trilayer mask).

SRIM is a useful tool for investigating the range in different targets, but it is difficult to do 2-dimensional device modeling. It also lacks the capability to take into account the crystallinity of the sample where channeling effects can significantly alter the damage. To perform more complex simulations a commercial software package called Athena from Silvaco [54] was used. It is a common tool used in semiconductor processing for the simulation of implants, annealing and etching. The model used for the simulations was a Monte Carlo model based on the Binary Collision Approximation.

Figure 3.24 is an example of a simulation that shows the structure and implantation damage from $1 \times 10^{13} \text{ Ne}^+/\text{cm}^2$. The mask opening is parallel to the

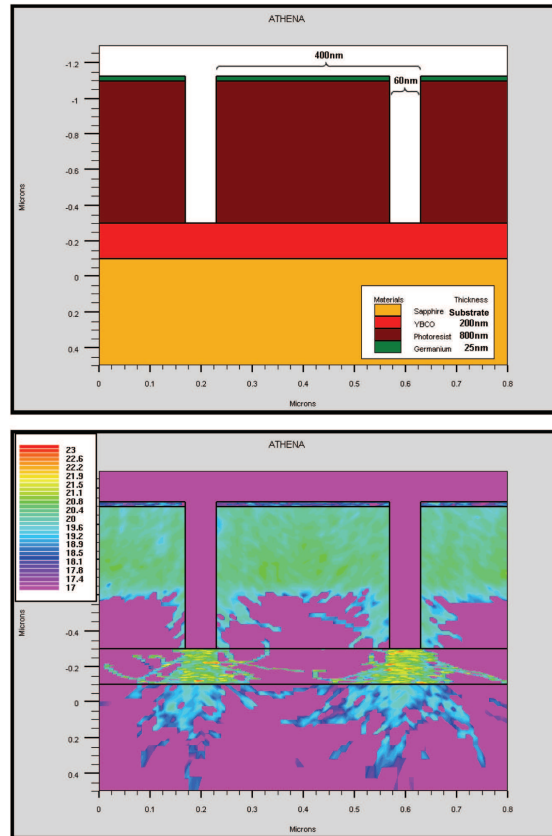


Figure 3.24: Implantation simulation of a 400 nm space junction pair. The contour scale is the base ten log of the number of displacements for cm^3 .

b - c plane of $\text{YBa}_2\text{Cu}_3\text{O}_{7-\delta}$ and the cross sectional view is taken along the a - c plane. Implantation parameters rotation, tilt, energy and dose were varied along with the mask dimensions and materials to gain insight into this process. Simulations were also performed for comparison with experimental results.

3.11 Electron Beam Proximity Effect

In EBL backscattered electrons can travel tens of microns in the resist. The range of the electron beam scattering depends on the energy of the incident electron beam, the thickness of the resist, and the materials under the resist. If enough of these electrons expose an area over the threshold of the resist it can result in the development of undesired features. This effect called the proximity effect and typically manifests itself in the broadening of the pattern features. Since the density of the scattered electrons decay exponentially with distance from the beam, closely distributed patterns are affected by the proximity effect substantially more than sparsely distributed ones. In the case of a set of uniformly spaced identical parallel lines for the ion-damaged Josephson junction arrays, the resultant pattern will not faithfully replicate that which was written. Lines in the center of the pattern receive a higher dose than those on the outside resulting in thinner line widths for those written on the edges.

Figure 3.25 shows an exposure vs. distance curve determined by measuring the line widths for different doses. A double-Gaussian function was fit to the data for comparison. A double-Gaussian model is commonly accepted as an approximation to the real scattering behavior. This curve illustrates how important the proximity effect is. The equivalent relative exposure values for distances of 40, 250 and 500 nm are approximately 7×10^{-2} , 4×10^{-3} , and 2×10^{-3} , respectively. This means that writing an 80 nm wide single line will expose the area 250 nm and 500 nm away from the line to $\frac{2}{35}$ and $\frac{1}{35}$ of the threshold of the resist required for development. This may not seem to be a serious problem for just a few lines, how-

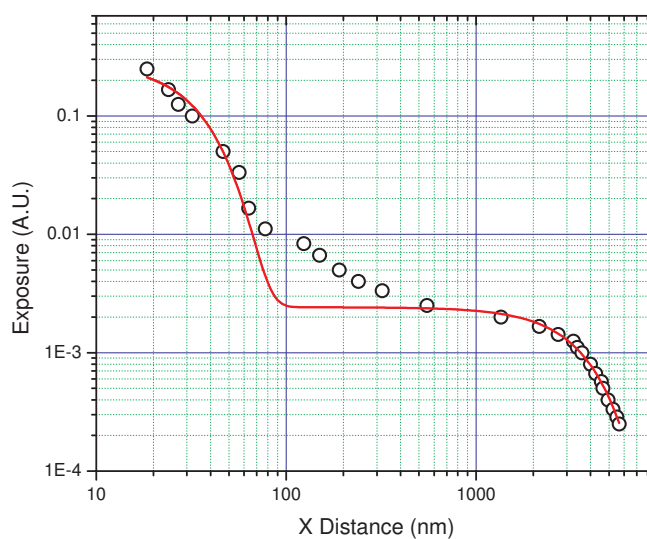


Figure 3.25: Exposure vs. distance data for single line writing demonstrating the electron beam proximity effect. Distance is measured from the center of the line. The solid line is a double Gaussian fit.

ever as the number of lines increases or the distance between the lines decreases, the exposure contributions from scattering of all the other line writings may add up to a significant value great enough to impact the line width. If the same dose is used for writing each line, the line at the middle of the array sees more exposure than the lines at the far ends.

Attempts to modulate the dose for each line to compensate for the differences a line in the middle would “see” compared with one at the edge was complicated and did not provide satisfactory results. The compensation was either too much or not enough. We attributed this failure to the inadequacy of the double-Gaussian approximation, which may be too simple to properly take into account the real behavior of electron scattering in our samples.

Instead of modulating the line doses, the dose was offset by writing additional simple patterns outside the line array. Writing additional lines with the same dose would make the lines in the middle part of the array experience a more uniform amount of electron scattering from the surroundings. However, the additional lines would then develop and be part of the pattern. Instead, the additional

lines can be replaced with simple rectangles with the same average surface dose. Since most of the areas of the rectangles are far away from all the lines, the lines in the array still feel roughly the same amount of scattering from writing the rectangles as if they were lines. The writing of the rectangles did not leave any pattern after developing as long as the dose was below the threshold of the resist. Experiments have shown that this idea works very well. Figure 3.26 illustrates the writing pattern for 100 parallel lines. Each line is $80\ \mu\text{m}$ long and was written by scanning the electron beam in only one scan. The width is controlled by the writing dosage. The center-to-center distance between adjacent lines was $250\ \text{nm}$ and $500\ \text{nm}$ for two separate samples. Two rectangles were written next to the line at the each end of the array as compensation for the proximity effect. Their size was $80\ \mu\text{m}$ by $20\ \mu\text{m}$. The separation between the rectangle and the last line in the array was kept the same as the line period in the array. The doses for all the lines in an array are the same and the doses for the two corresponding rectangles are the same. The doses for the rectangles are set by the average surface dose of the arrays. In order to determine the effect of the rectangles, another pattern with a rectangle at only one end was also written. The doses for writing the rectangles

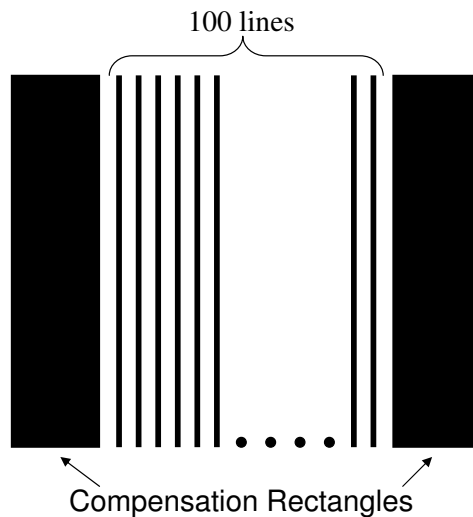


Figure 3.26: Illustration of the pattern for writing 100 parallel lines and compensation rectangles at each end of the lines (not to scale).

are 80 and 120 $\mu\text{C}/\text{cm}^2$ for 250 and 500 nm period line arrays. The dose threshold for developing PMMA is about 250 $\mu\text{C}/\text{cm}^2$. Consequently, writing compensation rectangles left no pattern after development. After developing and RIE etching, the stencil structure was measured under the same SEM. The NPGS was used to record the SEM images and measure the widths of the resultant lines.

Figure 3.27 (a)(b)(c) shows the left end, middle and the right end region of the 100-line (spaced at 500 nm) array with compensation rectangles; (d)(e)(f) shows the corresponding regions with a compensation rectangle written only at the right end. The widths of the lines for the first sample are all 86.9 nm, while the widths of the lines for the second one are 80.7, 93.1 and 93.1 nm for the left, middle, and right region. It is clear that the line width differences induced by the electron proximity effect have been corrected with the rectangles. The result for a sample of 100-line with 250 nm period is shown in Figure 3.28. The array has the same line width 37.2 nm for lines in the middle and by the edge of the array.

The sizes of the compensation rectangles are not critical. The compensation rectangles only have to cover the entire area from which scattered electrons could reach the array. From Figure 3.25, the range of electron scattering is less than 10 μm . Therefore, the size of the rectangles were chosen to be 80 μm by 20 μm . Since rectangles were used, which are continuous patterns, to compensate scattering from discrete lines (or individual patterns in two dimensional cases), summation is substituted by an integral in the approximation, which is good only when the array size is sufficiently large and the period is small enough. Based on Gaussian-like behavior of electron scattering, it is estimated that the array size has to be larger than the electron scattering range. From experiments, this method works with periods of 500 nm and less.

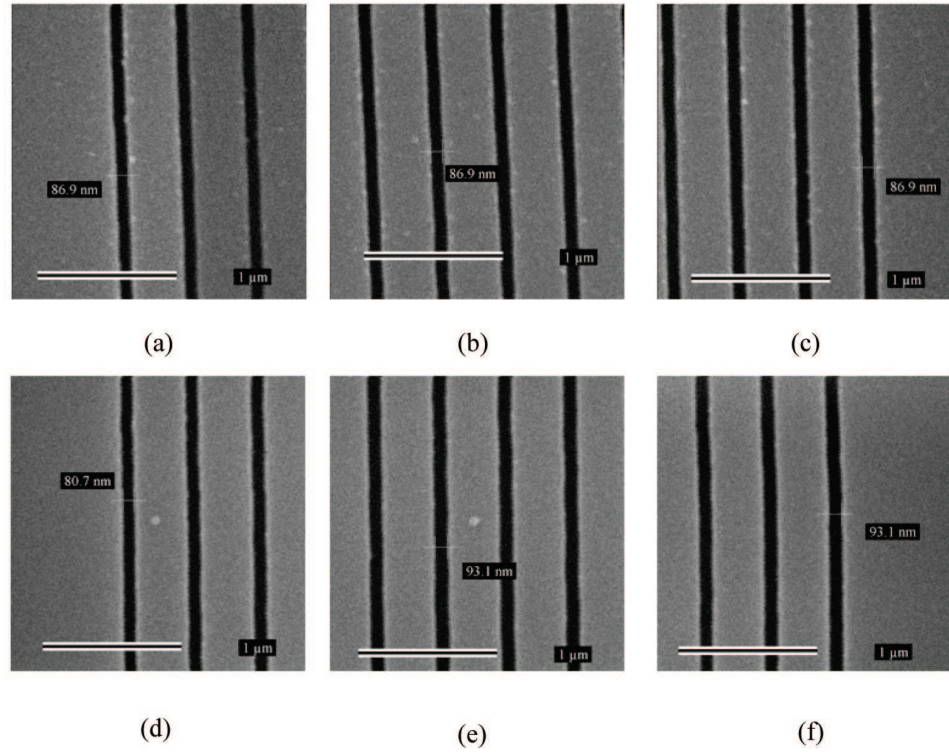


Figure 3.27: SEM pictures of the 100-line array with 500 nm period. (a), (b), (c) The pictures of the left end, middle, and the right end of the line array of a sample with both compensation rectangles written. (d), (e), (f) The pictures of the corresponding parts of the line array of a sample with only right compensation triangle written.

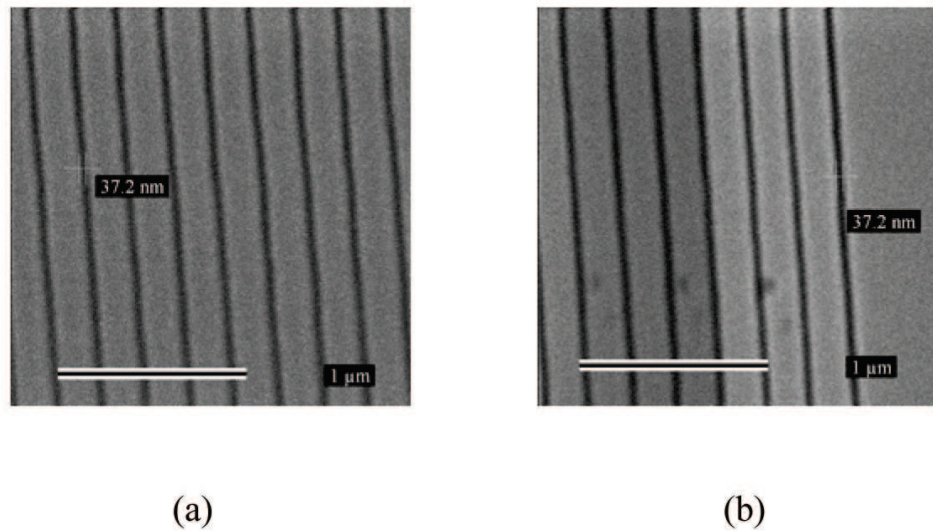


Figure 3.28: SEM pictures of the 100-line array with 250 nm period. (a) The middle part, (b) the right end of the line array. A compensation rectangle has been written by the right end.

Chapter 4

Measurements

To perform the electrical measurements, a custom cryogenic dip probe was built for this dissertation. At the top of the probe was a 6-way cross with $2\frac{3}{4}$ " con flat (CF) flanges. Mounted at the top flange was a butterfly valve and roughing port to evacuate the probe. The side faces of the cross contained two 19-pin electrical vacuum feedthroughs, a 32-pin feedthrough and an 18 GHz SMA RF feedthrough (Figure 4.1). The electrical feedthroughs had circular MIL-26482 series connectors on the air side and solder cups on the vacuum side. Attached to the bottom face of the cross was a spacer containing a thermocouple vacuum gauge and a pressure relief valve. At the bottom of the spacer was a reducing nipple welded to a 36" length of $\frac{3}{4}$ " diameter stainless steel tubing. Around the perimeter of the tubing was a quick-disconnect fitting welded to a Ladish flange, the common flange used on helium storage Dewars. The probe could be sealed in a storage dewar and the height could be easily adjusted by the quick disconnect fitting.

Mounted at the end of the tube was a $\frac{1}{2}$ " x $\frac{1}{2}$ " x $1\frac{1}{2}$ " copper block. Holes were drilled in the block to accommodate a $50\ \Omega$ resistor which served as a heater, a Lakeshore Cernox thermometer for temperature measurements below 40 K and a Lakeshore PT-103, platinum thermometer for temperature measurements above 40 K. A square socket, for 44-pin J-Lead chip carriers was attached to the top

of the copper block. Four leads from each thermometer and two from the heater were wired to one of the 19-pin feedthroughs. Pins 1 through 25 of the 44-pin socket were wired to the 32-pin feedthrough and 26 through 44 were wired to the other 19-pin feedthrough. 28 gauge teflon insulated copper wire was used for all connections. The heater and thermometer lines were separated from those of the devices in their own feedthrough to prevent any interference. It would have been preferable not to split the device lines between two feedthroughs however a 44-pin or greater feedthrough was not available. A low temperature 18 GHz microwave cable connected the SMA feedthrough to a length of coax with its center conductor bared, situated directly above the chip carrier socket to serve as an antenna. A

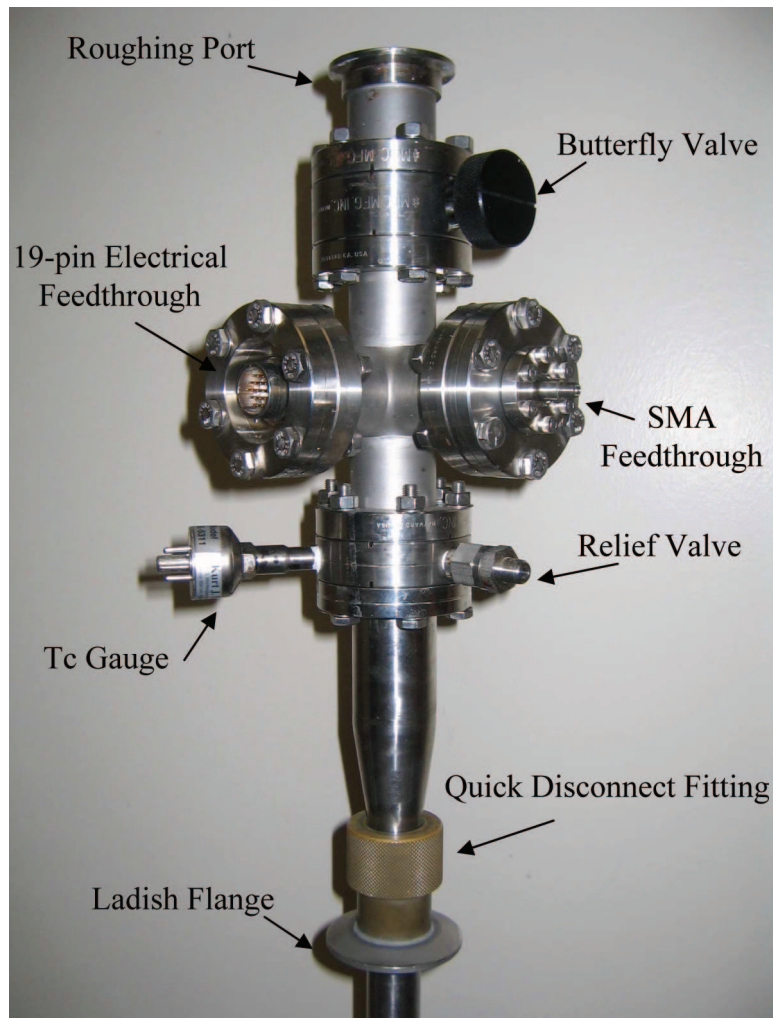


Figure 4.1: Top of the cryogenic dip probe built for this dissertation.

brass cylindrical jacket was used to encase the lower end of the probe. It was sealed with Woods metal solder (a eutectic alloy of Bi, Sn, Pb, and Cd with a melting point of 70°C) to a brass ring welded to the outside of the tubing. A copper shield surrounded the socket to increase the thermal stability. The high thermal conductivity of the copper shield ensured the sample saw the same temperature in all directions.

Samples were mounted in the pocket of a 44-pin J-Lead chip carrier with silver paint. Contacts were ultrasonically wire bonded to the terminals of the carrier. For precise temperature measurements a Lakeshore Silicon diode DT-670D chip sensor was placed in the pocket of the carrier next to the sample (Figure 4.2). This was necessary for measurements of quantities as a function of temperature, because the thermometers in the probe were too far away from the sample and were only accurate after the system reached equilibrium. The carrier was loaded into the probe and the brass end of the probe was sealed. It was evacuated to about 10 mTorr with a roughing pump, and back filled with 1 Torr of Helium gas. The gas served as a thermal exchange gas. The end of the probe was submersed in a Dewar of liquid nitrogen and cooled to 77 K, then it was transferred to a 100 L liquid helium storage Dewar. Temperature could be accurately controlled by adjusting the height of the probe in the storage Dewar, because of this the heater

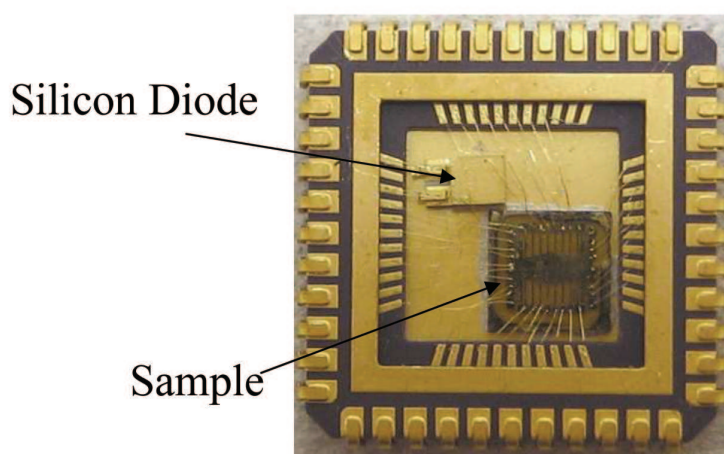


Figure 4.2: Sample and thermometer bonded in a 44 pin J-lead chip carrier.

was seldom used. Temperatures between 4.2 and 90 K were obtainable using this method. Helium was preferred over nitrogen for temperatures in excess of 77 K because it was easier to control the temperature. For the higher temperatures the probe was just above the Helium and very little boiled off. A 100 liter Dewar would typically last 4-8 weeks. Josephson devices are very sensitive to magnetic fields. Magnetic flux can be trapped in the superconducting leads or in the junction and significantly alter their electrical transport characteristics. Figure 4.3 demonstrates this effect on an $I-V$ characteristic. A single junction was measured at 71 K with no magnetic shielding. The light-switch in the room was switched on and off to create trapped flux in the junction. $I-V$ curves were recorded at various levels of trapped flux. It can be seen that the flux rounds the $I-V$ characteristic and reduces the value of the critical current. The reduction is asymmetric depending on which side of the junction the vortice(s) are trapped. Trapped flux in the junction or in the leads will result in breaking the symmetry of the junction. With this broken symmetry, the measured critical current will also be asymmetric depending on the direction of measuring current flow.

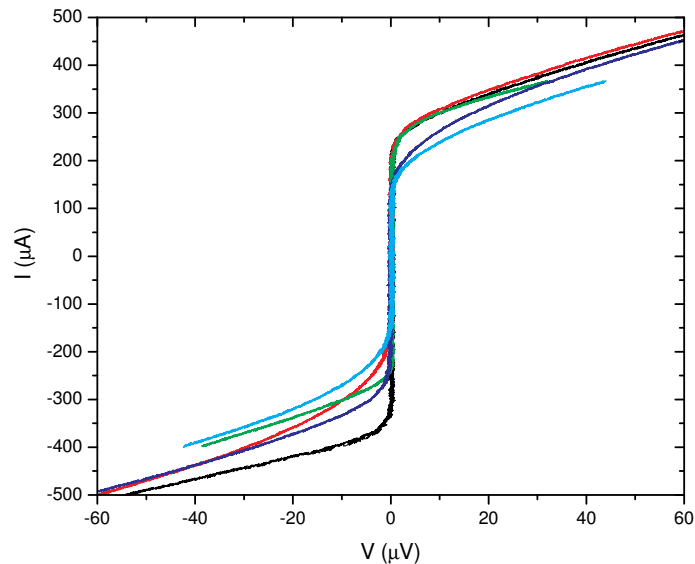


Figure 4.3: Flux trapping in a single junction measured at 71.0 K without any magnetic shielding.

To prevent flux trapping two shields were used. An HTS $\text{Bi}_2\text{Sr}_2\text{Ca}_2\text{Cu}_3\text{O}_{10}$ (BSSCO) shield with $T_c \sim 110$ K was used in place of the copper shield inside of the probe. When superconducting this shield would prevent any magnetic flux from entering the device. To prevent flux trapping before the BSSCO shield went superconducting, a μ -metal shield was used while cooling in nitrogen.

Electrical interferences and 60 Hz environmental noise can also cause problems when measuring Josephson devices. Therefore measurements were carried out in a Lindgren doubly shielded room. To further limit high frequency interferences all of the leads of the probe were filtered with tubular cascaded π -filter contacts arranged in a circular connector between the vacuum feedthrough and cable connecting the probe to the rack-mount panel. These connectors were manufactured by Amphenol Aerospace and had a 50 dB attenuation at 15 MHz and 80 dB attenuation for frequencies higher than 50 MHz.

Two different interfaces were used to connect instrumentation to the circular electrical feedthroughs on the probe. For current voltage characteristics a rack panel was designed with rotary switches that allowed quick switching between all of the 16 devices. For more generic measurements another rack panel with a BNC corresponding to each individual lead was used.

4.1 Resistance vs. Temperature

For measurements of resistance as a function of temperature the sample was measured as depicted in Figure 4.4. The oscillator signal (typically 1 V RMS, 22 Hz) of an EG&G DSP 7260 lock-in amplifier was connected in series with a limiting resistor (typically 500 kOhm) and the current leads of the sample. The voltage across the voltage leads was input into a SR560 low noise preamp with gain set to 10^4 . The output of the preamp was then fed back into the lock-in amplifier for measurement of the signal. The high pass and low pass filters of the preamp were set to 1 Hz and 1 kHz respectively. Temperature was measured using the

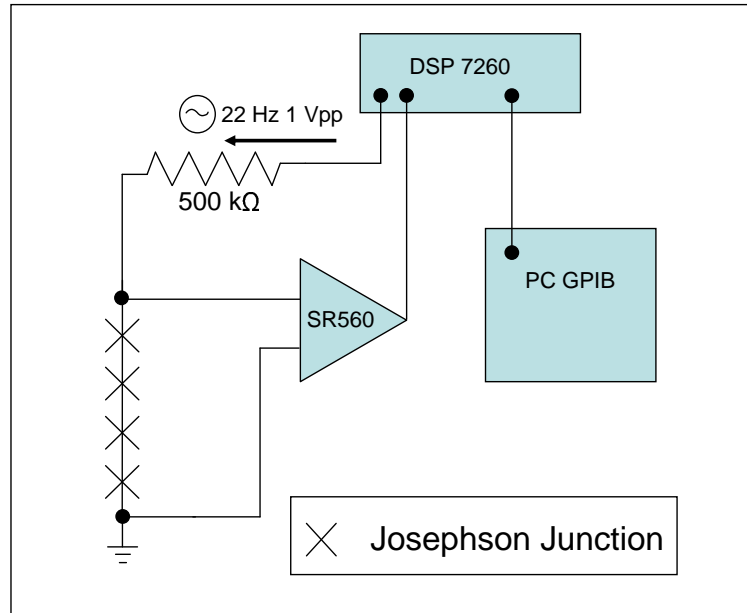


Figure 4.4: Schematic diagram for resistance-temperature measurements.

silicon diode sensor and a Cryocon model 32 temperature controller. The lock-in and temperature controller were both connected to the GPIB port of a computer and a Lab View program was used to collect data as the probe was cooled in liquid nitrogen or helium.

4.2 Current-Voltage Characteristics

Current voltage measurements were performed to determine junction parameters. Figure 4.5 is a schematic of a typical current voltage measurement. A 1 Hz, 8 V_{pp} triangle wave from an Agilent 33120A function generator was connected in series with a decade resistance box, a 100 Ω resistor and the current leads of the sample. The decade resistor was used to control the amplitude of the current. The voltage across the 100 Ω resistor and across the voltage probes of the sample was input to SR560 preamplifiers whose outputs were connected to the x and y channels of an Agilent 54830B digital oscilloscope. The voltage across the resistor was proportional to the current by a factor of 100. Typical gains for the preamps were 10³ and the band passes were set from DC to 1 KHz. The oscilloscope was

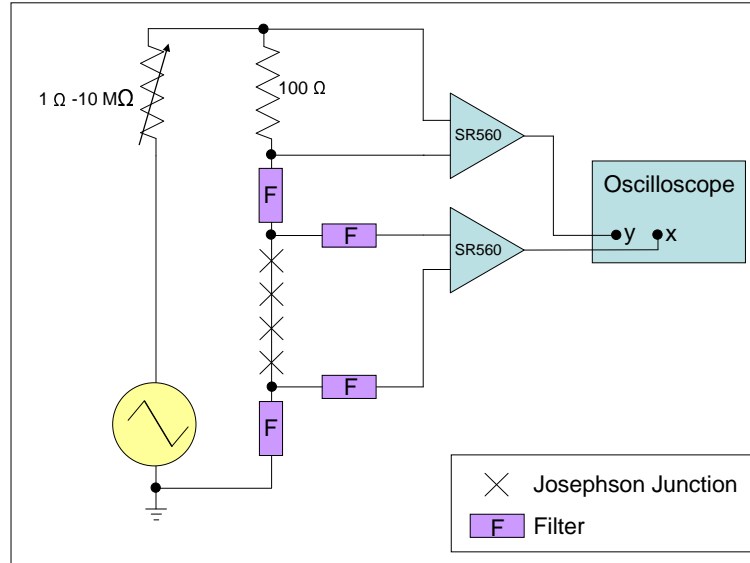


Figure 4.5: Schematic diagram for current-voltage measurements.

set to measure 10,000 points with 10 k samples/s so that data would include a complete period of the 1 Hz drive signal. The data-sets were recorded in ASCII format for further analysis. For observation of Shapiro steps an HP 83752A, 0.01 to 20GHz, microwave sweeper was connected to the SMA feedthrough of the probe and an RF signal was coupled into the junction(s) through the antenna.

4.3 Differential Resistance

If the junctions in an array have similar $I_c R_n$ products they will produce a Shapiro step at nearly the same bias current resulting in a giant Shapiro step. Differential resistance at this step should equal zero provided that all of the junctions are similar. Thus the differential resistance of a junction array is an important test of parameter uniformity. Figure 4.6 shows the technique used to measure differential resistance. The low frequency triangle wave was modulated with the output signal of a PAR 124 lock-in amplifier. This was achieved by inputting them into the differential inputs of a SR560 pre amp. This was then used to bias the sample as described in the previous section. The voltage across the sample was split into 2 SR560 preamps, one to output the low frequency voltage, and the other to pass the

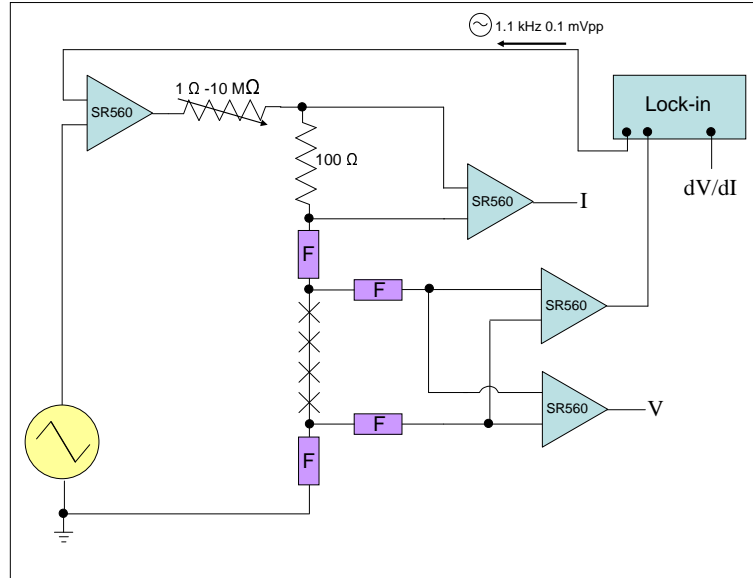


Figure 4.6: Schematic diagram for the measurement of differential resistance.

high frequency signal to the lock-in for detection. The output of the lock-in was differential voltage (dV) and because the limiting resistor was much greater than the resistance of the sample differential current (dI) can be considered constant, thus the output of the lock-in was proportional to $\frac{dV}{dI}$, the differential resistance. $\frac{dV}{dI}$ vs. V or I was then recorded using the oscilloscope.

4.4 Modulation of the Critical Current in Magnetic Field

For observation of the dc Josephson effect and to gain insight into how the current is distributed across the junction the magnitude of the critical current versus magnetic field was measured. The BSSCO shield was removed and the probe was cooled in a glass Dewar with liquid nitrogen. Pumping on this Dewar could lower the temperature to 58 K, if needed. A long coil was then situated around the bottom of the Dewar to introduce magnetic field. The coil was measured with a Gauss meter to determine the relationship between current and field (100 Gauss/A). The measurement of junction critical current was accomplished by using sample-and-hold electronics designed in conjunction with the UCSD Physics

Electronic Shop. The current and voltage was measured as in Figure 4.5 and input into the device. The voltage representing the current was held when the voltage across the junction passed a user defined threshold. Two of these circuits were used to record the current-voltage when the junction-voltage crossed $2 \mu V$ and $-2 \mu V$. The differential output of the two current-voltages held is approximately $2I_c$. This was then recorded along with the current through the coil (representing magnetic field) using a digital oscilloscope.

4.5 Shapiro Step Amplitude Dependence

Measurements of Shapiro step amplitude dependence on applied microwave power were carried out. The sample and hold device used in the previous section was used to determine the amplitude of the step by setting the appropriate thresholds. The microwave power was changed by either amplitude modulation using a triangle wave from a function generator or using a Lab View program which changed the power by communicating with the sweeper through its GPIB interface.

4.6 Temperature Dependence of the Critical Current

The temperature dependence of the critical current was determined by using the sample and hold electronics to determine the critical current. The output signal was then input to a Keithly 2000 DMM connected to the GPIB port of a computer. This was then recorded along with the reading of the temperature controller using a Lab View program.

Chapter 5

YBa₂Cu₃O_{7- δ} Josephson Junctions

5.1 Single Junctions

A successful VLSI junction technology must be able to fabricate junctions with junction parameters I_c and R_n that do not vary more than 10% between different junctions. Furthermore, different applications require different values of $I_c R_n$. For the Josephson arbitrary waveform generator, an $I_c R_n$ product between 24 and 40 μV at 65 K is desired, however SQUID applications require an $I_c R_n > 100 \mu V$. Therefore not only must a successful technology create uniform parameters, it must also be able to reproduce a given value of $I_c R_n$.

Although the primary goal of this work was to fabricate junction arrays, single junctions were also studied so that individual junction properties could be compared with those of arrays. Furthermore the uniformity of junction parameters is difficult to determine in an array because it would require voltage probes in between each of the junctions which is not practical.

Current voltage ($I-V$) measurements were performed to determine the uniformity and reproducibility of the junction parameters I_c and R_n . $I-V$ characteristics could be classified into two types. Resistively shunted junctions similar

to those described by the Stewart-McCumber model [17, 18] (RSJ) and curves rounded near I_c resembling those of flux-flow “long” junctions.

Figure 5.1 shows the $I-V$ characteristic at 63 K, for a junction fabricated from 200 nm $\text{YBa}_2\text{Cu}_3\text{O}_{7-\delta}$ on LaAlO_3 , implanted with $2 \times 10^{13} \text{ Ne}^+/\text{cm}^2$ at 200 keV. Figure 5.1(a) is a fit to the data using the RSJ model (equation 2.17). The data certainly follows the trend of the RSJ model however, it does not fit well near I_c where the critical current is rounded. At higher biases the resistance doesn’t follow that of the RSJ model due to broadening of the barrier. Rounding of the $I-V$ characteristic near the critical current can occur in junctions from thermal fluctuations that disrupt the coupling of the phases of the order parameters of the two superconducting electrodes. A common method for modeling of thermal rounding in Josephson junctions was first described by Ambegaokar and Halerpin [55]. A thermal noise current was introduced as an additional term in the RSJ model to account for the thermally activated phase slip processes. This model was

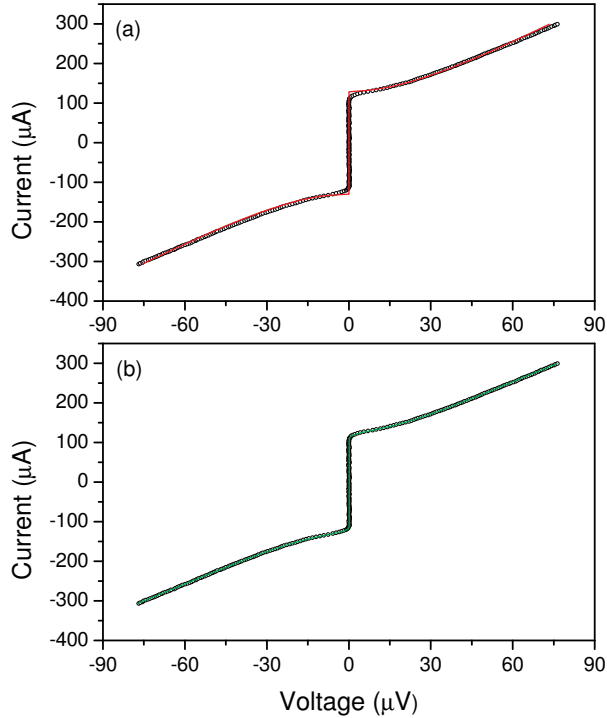


Figure 5.1: $I-V$ characteristic at 63 K showing a fit with (a) the RSJ model, and (b) the RSJ model with thermal rounding and a current dependent resistance.

combined with the current dependant resistance used by Katz and Dynes (equation 2.35) to fit the data. The result is shown in Figure 5.1(b). The noise temperature calculated from the fit was 71.9 K, which is close to the measurement temperature of 63 K. The additional noise temperature is attributed to the measurement system. Both of the fits produce similar $I_c R_n$, $35 \mu V$, and $31 \mu V$ for the RSJ and modified RSJ models respectively.

Figure 5.2 shows the $I-V$ characteristics at 5 different temperatures, for a junction fabricated from 200 nm $\text{YBa}_2\text{Cu}_3\text{O}_{7-\delta}$ on LSAT, implanted with $1 \times 10^{13} \text{ Ne}^+/\text{cm}^2$ at 200 keV. Near the T_c of the junction, $I-V$ characteristics have a RSJ-like shape. However as temperature is reduced the junction becomes strongly coupled and the $I-V$ curve becomes rounded near I_c . These rounded curves are similar to the rounding seen in “long” junctions, where the bridge width, w is larger than the Josephson penetration depth, w/λ_J . The crossover from short to long junction behavior is generally taken to be when the ratio $w/\lambda_J \geq 6$. This was calculated for the temperatures of the $I-V$ curves in Figure 5.2 and is displayed in the legend. At the crossover temperature, $T \sim 76.9 \text{ K}$, w/λ_J is over a factor of 3 smaller than what would be expected if this was solely a long junction effect.

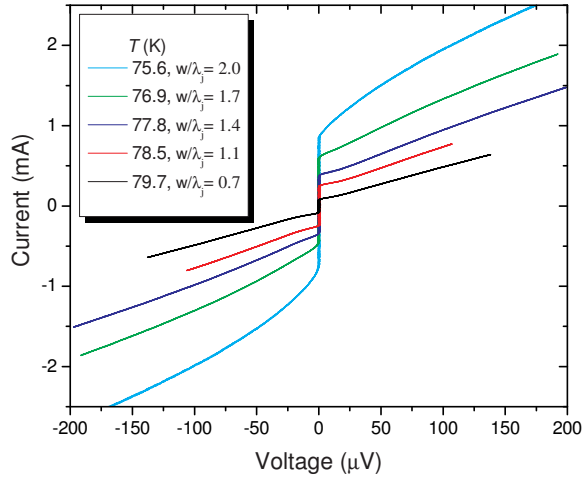


Figure 5.2: $I-V$ characteristics measured for the same junction at five temperatures. From top to bottom : 75.6 K, 76.9 K, 77.8 K, 78.5 K, 79.7 K. The junction’s barrier undergoes a transition from weak coupling to strong coupling with decreasing temperature.

Figure 5.3 shows the flux-flow regime $I - V$ characteristics of the ion damage junction from Figure 5.2. They have $V \propto I^n$ with n increasing with current density. This is consistent with models of vortex motion used to describe non-linear $I - V$ characteristics in flux-flow junctions [16, 56]. The transition from RSJ-like to flux-flow can be attributed to the junction changing from a SN'S to a SS'S junction as temperature is reduced below that of the critical temperature of the weaklink. From Likharev's theory of SS'S junctions [16] the current phase relationship becomes multi-valued when,

$$l/\xi \gtrsim 3.5$$

after which Abrikosov vortices may enter the weaklink. The entrance and motion of these vortices determine the properties of the junction, some of which resemble the ideal Josephson effects. When $T \rightarrow T'_c$, the critical temperature of the weaklink, $\xi \rightarrow \infty$ and $L/\xi \rightarrow 0$. Thus ideal Josephson effects are observed near T'_c for large barriers. Estimates of the coherence length using the Likharev model at the cross-over temperature are consistent with values determined from proximity effect fits of the critical current temperature dependence [8].

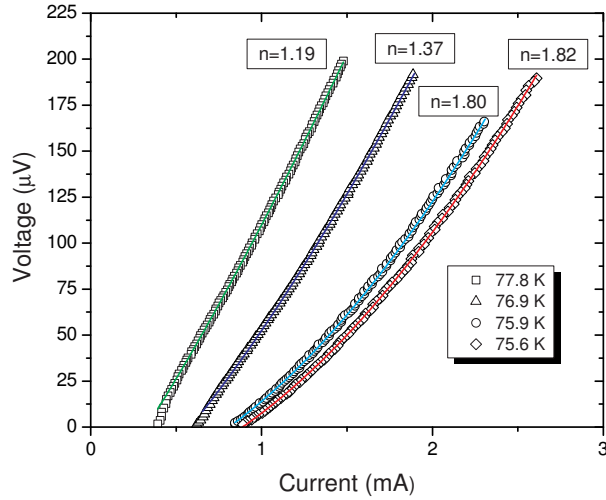


Figure 5.3: Flux-flow $V - I$ characteristics from the same junction in Figure (5.2). The solid lines are fits of the form $V \propto I^n$, where the exponent n is related to vortex motion in the weaklink.

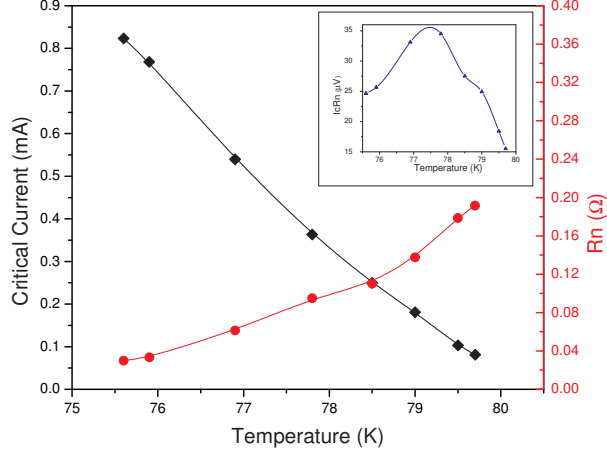


Figure 5.4: Critical current and normal resistance vs. temperature for the same junction from Figure 5.2. The inset shows the $I_c R_n$ product as a function of temperature. It has a peak where the junction transitions from RSJ-like to strongly coupled.

Figure 5.4 shows the temperature dependence of the critical current and normal state resistance for the same junction in Figure 5.2. The inset shows that $I_c R_n$ has a maximum near the crossover temperature. This feature has been empirically observed in many junctions near the temperature where the junction becomes strongly coupled.

The uniformity of the junction parameters for the single junctions fabricated on this sample were outstanding. Figure 5.5 shows the $I-V$ characteristics measured at 79.7 K, for 6 of 8 single junctions fabricated on one side of a 16-bridge sample by writing a single line across all bridges. Two of the junctions were not measured due to faulty contacts. The junctions are labeled J1-J8 with the number representing the position of the bridge. The $I-V$ curves for J3, J4, J6, and J7 are nearly identical, which seldom occurs in other HTS technologies. J1 and J8 have larger critical currents and smaller resistances indicating less damage. These junctions are located on the top and bottom bridges on the outside of the EBL pattern. Junctions fabricated on these bridges consistently had less damage for many samples. It was suspected that the substrate on the outside of the bridges was charging during the implantation and repelling incoming ions and hence reducing the damage. The implantation time was increased by an order of magnitude

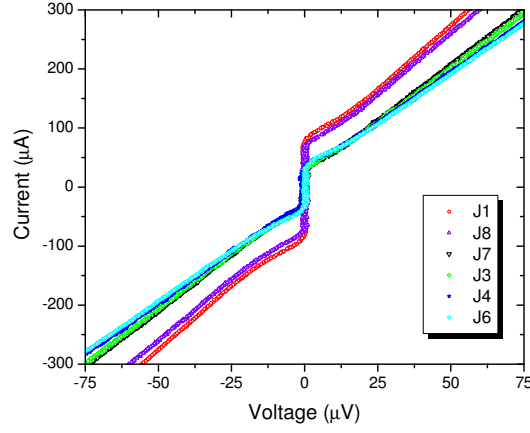


Figure 5.5: Six junctions from the same chip. The legend labels the curves from top to bottom. The parameters of J7, J3, J4, and J6 are nearly identical.

by decreasing the current to allow time for accumulated charge to dissipate. This had no effect and the outside bridges still appeared less damaged than those in the center.

The temperature dependence of the junction's critical current was consistent with the Katz-Dynes model which suggests a $(1 - T/T_c)^3$ dependence near T_c and a $(1 - T/T_c)^2$ dependence at lower temperatures. Figure 5.6 shows data for a junction fabricated from 100 nm $\text{YBa}_2\text{Cu}_3\text{O}_{7-\delta}$ on Al_2O_3 , implanted with $1 \times 10^{13} \text{ Ne}^+/\text{cm}^2$ at 200 keV, showing both fits.

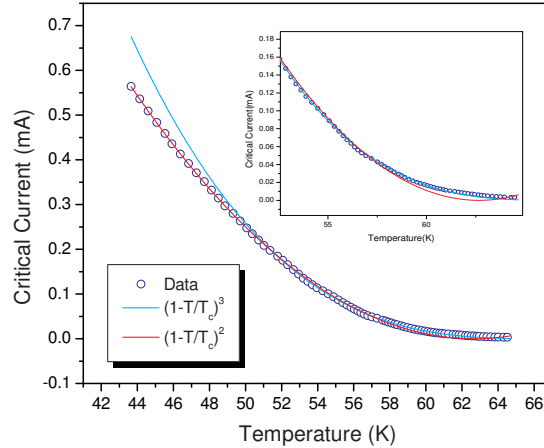


Figure 5.6: Critical current vs. temperature, near T_c the data have a $(1 - T/T_c)^3$ dependence. At lower temperatures it follows a $(1 - T/T_c)^2$ dependence.

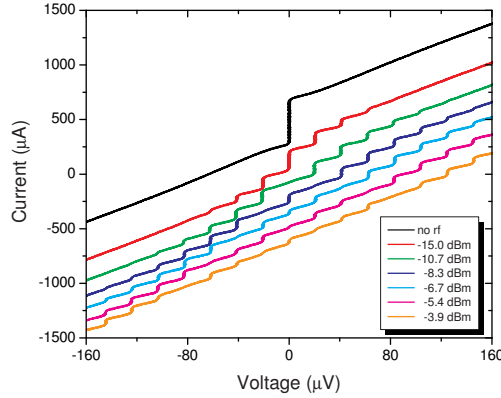


Figure 5.7: Shapiro steps in a junction's $I-V$ characteristics for different applied 10 GHz RF powers, measured at 77.7 K. The y -axis has been offset for clarity.

RSJ-like junctions exhibited the ac Josephson effect [1]. Steps occurred precisely at $V = \frac{nhf}{2e}$, with harmonics out to $n > 10$. Figure 5.7 shows $I-V$ characteristics for J6 of Figure 5.5 measured at 77.7 K. 10 GHz microwave radiation was introduced through an antenna and curves were measured for 6 different power levels. The amplitude dependence of the Shapiro steps as a function of RF Voltage for another similar junction was measured and is shown in Figure 5.8. The amplitudes have a Bessel-like dependence confirming that the steps are due to the ac Josephson effect.

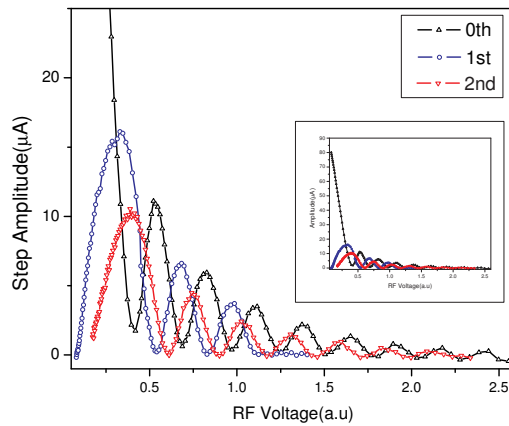


Figure 5.8: Bessel-like dependencies of the critical current ($n = 0$), and the first two Shapiro steps. The inset shows the full range of the data.

The modulation of the supercurrent in magnetic field was also measured as a test for the dc Josephson effect. Figure 5.9 shows a junction fabricated from 200 nm $\text{YBa}_2\text{Cu}_3\text{O}_{7-\delta}$ on LaAlO_3 , implanted with $1.5 \times 10^{13} \text{ Ne}^+/\text{cm}^2$ at 200 keV. The slit in the mask used to define the ion damage region was 50 nm. The data were taken at 65 K by sweeping the field from -40 to 40 Gauss and then sweeping back. The two traces represent data taken with increasing and decreasing field. Hysteresis is apparent between the two sweeps. This occurs when the field exceeds H_{c1} and Abrikosov vortices enter the film and become trapped in the electrodes near the junction. The vortices partially cancel the Meissner screening currents near the edge of the junction and shifts the pattern [57]. The period of magnetic field oscillation was calculated to be 15.6 Gauss by using equation(2.26), and estimating $\lambda_L = 300 \text{ nm}$. This is in close agreement to the measured value of the average oscillation period, 14.9 Gauss. This is a rare occurrence in Josephson junctions with a planar geometry. Planar junctions usually exhibit much smaller oscillation periods attributed to flux focusing effects. Theories by Rosenthal et. al. [58], and Humphries-Edwards [59] are commonly used to predict the periods in planar junctions. They make the claim that in a planar geometry the junction is unshielded opposed to the vertical geometry in classical junctions with thick electrodes. More

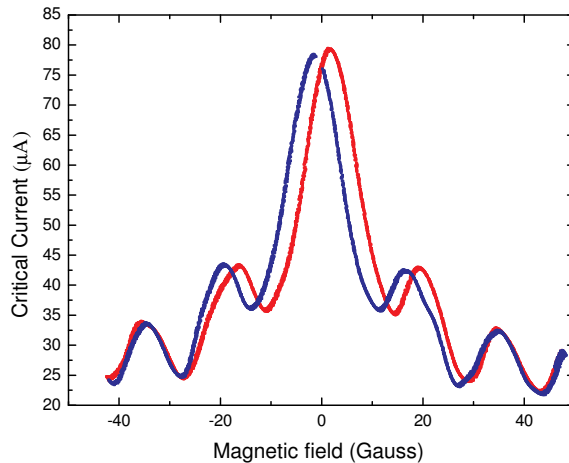


Figure 5.9: Fraunhofer pattern demonstrating the dc Josephson effect. The two curves show the hysteresis for sweeps of increasing and decreasing field.

field can penetrate in the planar junction case giving the appearance of a larger junction area. The period of oscillation for the junction in Figure 5.9 was calculated using these theories, resulting in 9.5 and 4.7 Gauss for Rosenthal, and Humpries-Edwards respectively. Both of these theories accurately predict the oscillation periods in grain boundary and ramp junctions yet they clearly fall short in the case of the ion damage junctions where the classical model describes the data better.

Figure 5.10 shows the $I-V$ characteristic without field and in field at the first minimum (Φ_0). A non-Josephson current of $25 \mu A$ is observed and a common occurrence in ion-damage $YBa_2Cu_3O_{7-\delta}$ junctions [24, 60]. It can occur from a number of different mechanisms that are related to strong coupling effects [61, 62]. It is insensitive to the phase difference across the junction and does not modulate in magnetic field. It can be viewed as a superconducting short in parallel with the junction. This is consistent with $I-V$ temperature data (figure (5.2) and simulation results that show the barrier is made up of grains of different damage levels. As temperature decreases some of the grains become superconducting and create a percolative network of superconducting shorts. Non-uniform current distribution across the barrier from defects can also prevent the minima from reaching zero

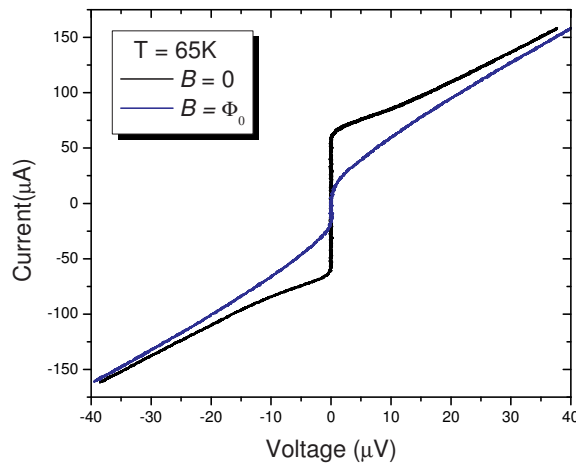


Figure 5.10: $I-V$ characteristic with and without an applied flux of Φ_0 .

thus the value of the current at the minima can only be taken as an upper limit on the excess current in the junction.

The effects of anneals on the junctions was also investigated in an attempt to improve uniformity. Anneals were performed in Oxygen at 800, and 400 °C and also in air at 100°C. The two highest temperature anneals resulted in reduced T_c of the bulk films and in some cases insulating samples. The low temperature anneal on the other hand, substantially improved the devices.

Figure 5.11 shows the $I_c R_n$ vs. temperature for the same junction before and after a 2 hour 100°C anneal. The operating temperature of the junction increased by over ten degrees. $I_c R_n$ also showed a considerable increase due to an increase in critical current. Figure 5.12 shows a plot of $I_c R_n$ vs R_n , for R_n of 0.07 and 0.05 there is a 5 times and 2 times increase in $I_c R_n$ respectively. Figure 5.13 compares two $I-V$ curves of the same resistance showing that it retains its RSJ-like appearance after a 2 times increase in the critical current. This is significant because high $I_c R_n$ products are desirable for some devices such as SQUIDs or SQIFs.

It seems likely that at 100°C the thermal energy is sufficient for the recombination of vacancy-interstitial defects which results in recovery of T_c . At

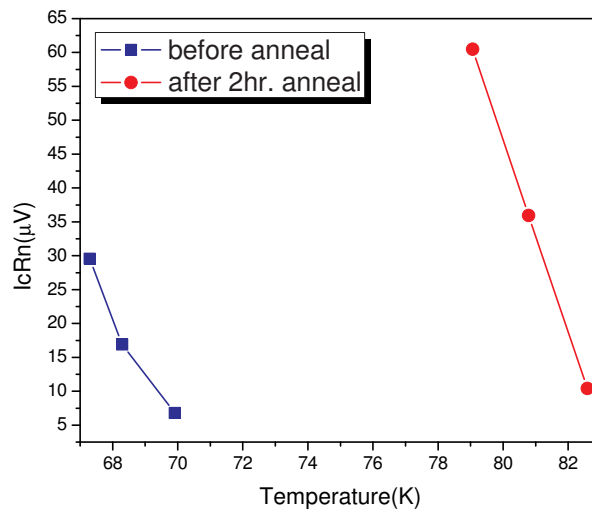


Figure 5.11: $I_c R_n$ vs. temperature for the same junction before and after a 2 hour anneal at 100°C.

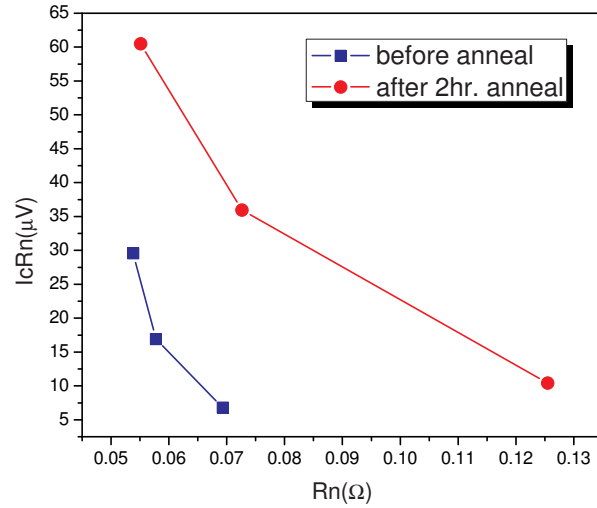


Figure 5.12: $I_c R_n$ vs. R_n showing a substantial increase in $I_c R_n$, for constant R_n .

the higher temperatures the thermal energy is greater than the oxygen activation energy which results in oxygen loss and a lower T_c .

The results from the studies of the single junctions demonstrate that this technology is capable of creating uniform and reproducible HTS Josephson junctions with RSJ-like $I-V$ characteristics. Furthermore the anneals provide a way to substantially increase $I_c R_n$ which broadens the possible applications.

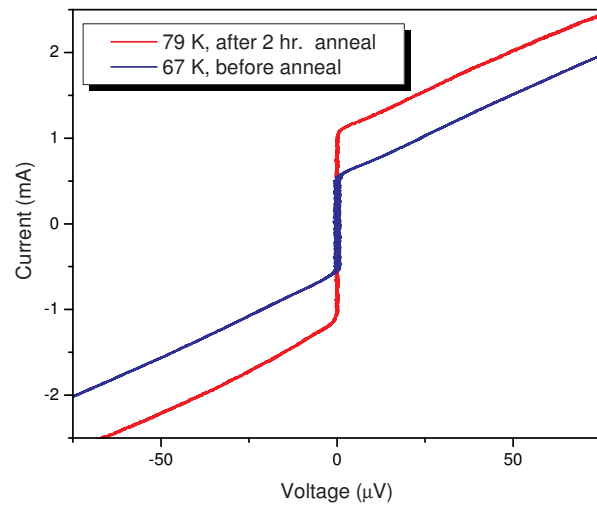


Figure 5.13: $I-V$ characteristics before and after the anneal. The resistance is the same and the critical current is increased by a factor of two. After the anneal the $I-V$ characteristic retains its RSJ-like shape.

5.2 Junction Pairs

Most applications associated with Josephson junction arrays require that all the Josephson junctions in the array are phase-locked to the applied microwave or to each other [28]. The interactions between Josephson junctions have been investigated intensively [63]. However, due to the complexity of Josephson junctions as highly non-linear quantum devices, the physics of the interactions has not been fully understood. Interaction mechanisms (e.g., mediated by Cooper pairs, quasi-particles and electromagnetic field) have been suggested to account for the mutual phase-locking between the junctions [63]. Because of the short coherence length in HTS materials the interaction mediated by Cooper pairs is expected to be weak unless the junctions are extremely close to each other. Theoretical analysis shows that apparent mutual interactions can be observed if the junction distance is less than 50ξ [64]. The fabrication difficulty of closely spaced junctions has ruled out many common types of HTS Josephson junctions, such as artificial grain boundary junctions and ramp-type junctions. Furthermore it is a difficult task to fabricate pairs with an electrode in between, so that individual junction behavior can be measured. EBL was used to pattern two slits with a center electrode in the tri-layer mask (Figure 5.14(a)) at the center of the 16 bridge pattern (Figure 3.13) where two of the bridges intersect the common electrode. After ion damage the uncovered material has a reduced T_c which effectively transfers the pattern in to the film with no need for etching. Figure 5.14(b) shows the measurement configuration for simultaneous measurement of individual $I-V$ characteristics along with the series pair.

Many identical pairs were created with 200, 400, and 800 nm center to center spacing. Figure 5.15(a) shows $I-V$ curves measured at 63 K for a 400 nm spaced pair with slit width of 50 nm, fabricated from a 200 nm $\text{YBa}_2\text{Cu}_3\text{O}_{7-\delta}$ film on LaO_3 implanted with $2 \times 10^{13} \text{ Ne}^+/\text{cm}^2$ at 200 keV. The analog oscilloscope was used so that all of the traces could be viewed simultaneously because the

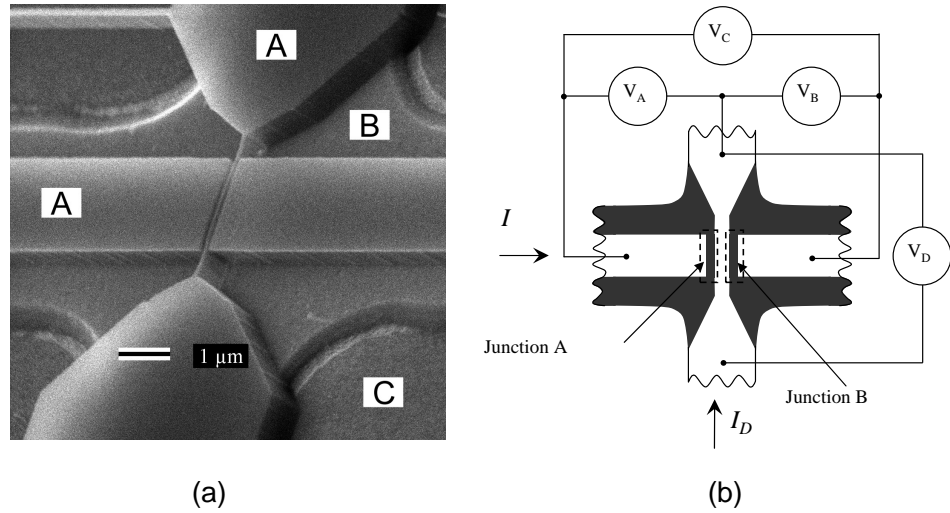


Figure 5.14: The SEM picture of a junction pair after ion damage. A, B, and C denote the photoresist mask, the YBa₂Cu₃O_{7-δ} bridge, and the sapphire substrate, respectively. (b) Schematic drawing of the junction pair and measurement configuration.

digital oscilloscope only had two channels. Traces A and B are for the individual junctions and trace C is for the pair in series. Figure 5.15(b) is with 12 GHz applied microwave radiation. Large amplitude Shapiro steps are visible in the single junctions at $V = \frac{nhf}{2e} = n \times 24 \mu V$ and twice this amount in the series pairs. It is assumed that these junctions are locking to the drive signal because other experiments did not show any evidence of an order parameter interaction.

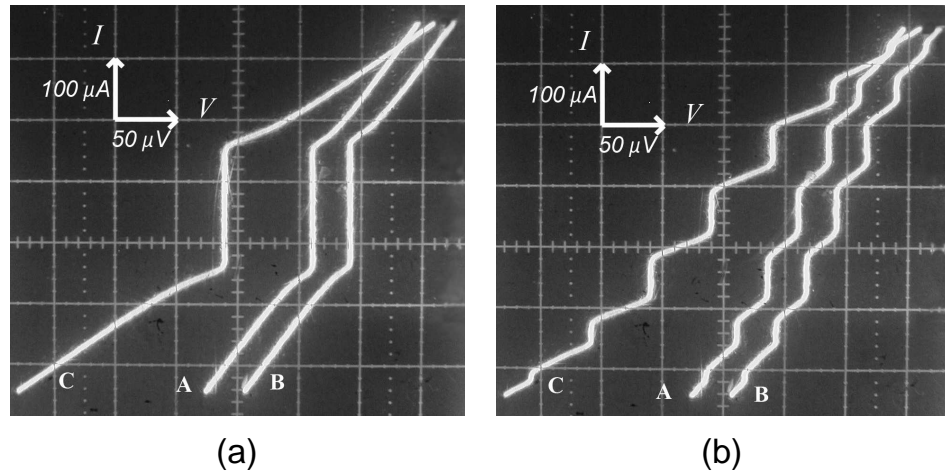


Figure 5.15: Oscilloscope pictures of the current voltage characteristics of junction 1 (curve A), junction 2 (curve B), and the pair in series (curve C) without (a) and with (b) 12 GHz microwave radiation.

Figure 5.16 shows results from a 150 nm spaced pair fabricated from 200 nm $\text{YBa}_2\text{Cu}_3\text{O}_{7-\delta}$ on LaAlO_3 implanted with $1 \times 10^{13} \text{ Ne}^+/\text{cm}^2$ at 200 keV. The $I-V$ curves A and B are measured using the center electrode, and across the two in series, C. Under 13 GHz the series pair showed steps that followed the AC Josephson relationship for a single junction. Fractional Shapiro steps were observed on the other two curves. At low temperatures these junctions show two junction behavior. This is strong evidence that the damage merged underneath the electrode to form a single barrier and contradicts a report that the barrier length in these junctions is equivalent to the slit size in the mask [27]. This geometry provides a novel tool to probe inside the barrier of a Josephson junction.

Athena ion implantation simulations were performed for the device of Figure 5.16. The structure and results are shown in Figure 5.17. The implant damage straggles underneath the center mask region and merges into one another. The central region appears to have slightly lower damage or equivalently a higher T_c , which explains why they demonstrate double junction behavior at low temperatures.

Nearly identical, closely spaced junction pairs were fabricated with elec-

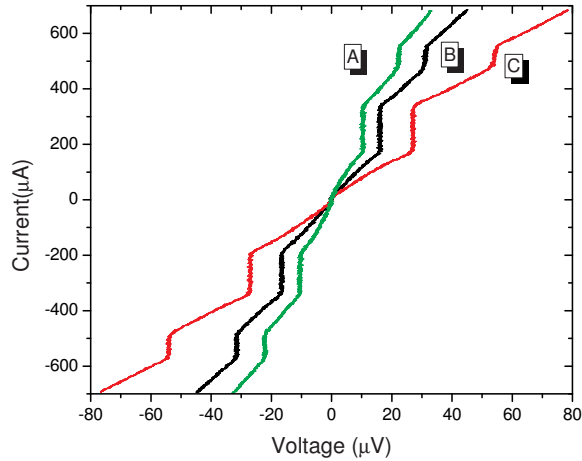


Figure 5.16: $I-V$ characteristics at 71 K for a 150 nm spaced junction pair with 13 GHz microwave radiation. A and B were measured using the central electrode and C is measured across the pair.

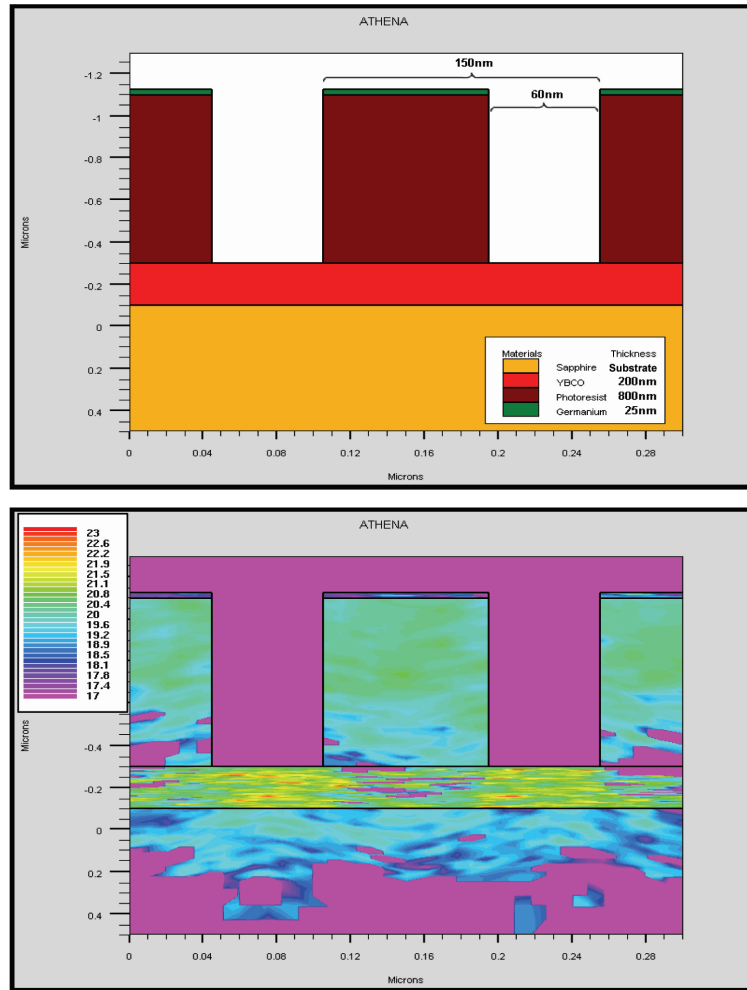


Figure 5.17: Implantation simulation

trodes in between them to study individual and collective junction behavior. No order parameter interactions or phase locking was observed possibly due to the short coherence length in $\text{YBa}_2\text{Cu}_3\text{O}_{7-\delta}$. Junctions with spacings of 150 nm merged to form a single junction allowing for the unique opportunity to probe the voltage inside of the barrier. It is also strong evidence that the barrier in ion damage junctions is much larger than the slit size in the implantation mask.

5.3 Series Arrays of Junctions

The focus of this work was to fabricate multi-junction series arrays with similar $I_c R_n$ products for use in ac voltage standards. Arrays were fabricated with line spacing that ranged between 125 nm - 2 μm . The slits used to define the junctions ranged from 30-110 nm wide. Arrays of 4, 10, 20, 50, and 100 junctions were attempted. Figure 5.18 shows a section of a typical implantation mask. This one in particular was for a 100 junction array with line spacing of 231.7 nm and slit width of 50 nm.

In an attempt to enhance uniformity a technique was developed to reduce the effective width of the bridges using ion damage. Rectangles on the bridge edges were written in the PMMA and etched along with the slits defining the junctions, so that the edges would be damaged during the implantation. Figure 5.19 shows

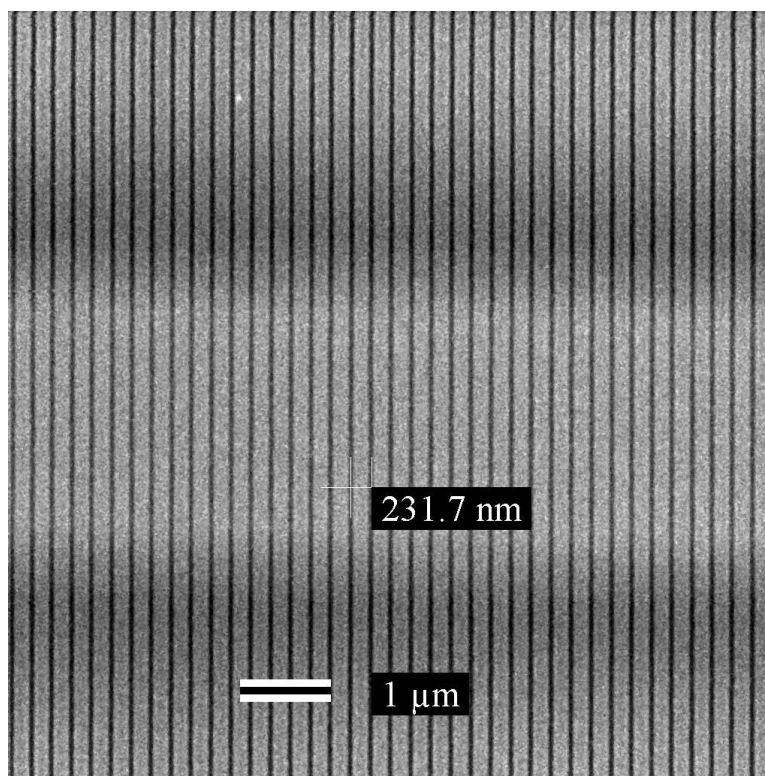


Figure 5.18: SEM picture of an etched tri-layer mask used for creation of a 100 junction array. The slits are 50 nm wide with a spacing of 231.7 nm.

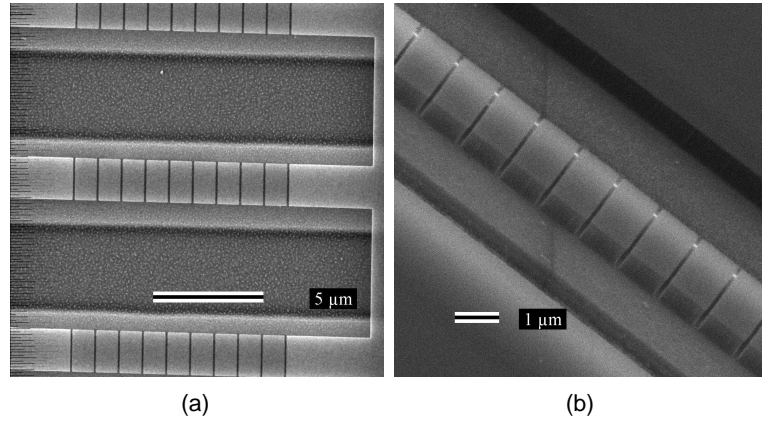


Figure 5.19: (a) Top view and 47° tilt of a tri-layer mask patterned so that ion damage can reduce the bridges electrical width from 4 to 2 μm .

the top view of the stencil used to damage the junctions and bridges for a sample of 10 junction arrays. Samples were made with bridges as narrow as 0.5 μm .

Figure 5.20 shows the $I-V$ characteristics for ten junction arrays from 3 different samples. Samples A and B were fabricated from 200 nm $\text{YBa}_2\text{Cu}_3\text{O}_{7-\delta}$ on LSAT, implanted with $2 \times 10^{13} \text{ Ne}^+/\text{cm}^2$ at 200 keV. Sample C was fabricated from 200 nm $\text{YBa}_2\text{Cu}_3\text{O}_{7-\delta}$ on Al_2O_3 , implanted with $0.5 \times 10^{13} \text{ Ne}^+/\text{cm}^2$ at 200 keV, furthermore the bridge width was damaged down to 2 μm . All of the junctions

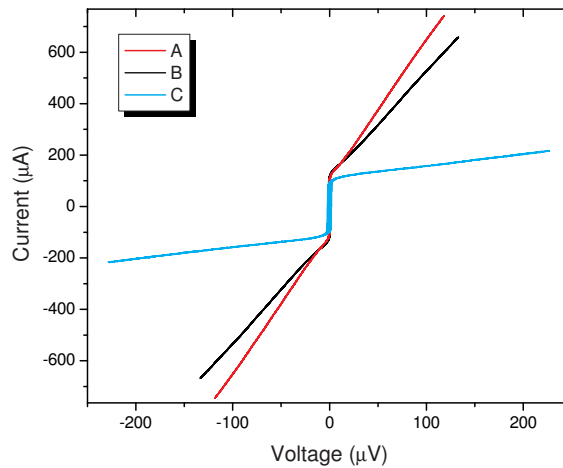


Figure 5.20: $I-V$ characteristics for 3 different ten junction arrays measured at 78.0 K, 77.3 K and 84.0 K for A, B, and C respectively.

had similar slit sizes 80, 85, and 90 nm for A, B, and C respectively. The inter-junction spacing was 400, 2000, and 1000 nm for A, B, and C respectively. The $I-V$ characteristics are RSJ-like and all exhibit flat giant Shapiro steps at 10 times the voltage of a single junction. The resistance of sample C is higher than that of A and B as expected from having the bridge reduced to 2 μm .

Figure 5.21 shows the $I-V$ characteristics of sample C at 4 different temperatures fit using the RSJ model modified for thermal rounding and current dependant resistance as described in the previous section. The noise temperature calculated for the smallest I_c is 89 K which is only 5° higher than the actual measurement temperature and in good agreement with our single junction results.

Junction arrays were tested for uniformity using the ac Josephson effect. Appearance of flat giant Shapiro steps is an indication that the parameter spread of the junctions in the array is less than 10% [64–66]. Figure 5.22(a) shows $I-V$ characteristics for sample B, with and without 15 GHz microwave radiation. Giant Shapiro steps are visible at 0.31 mV, 10 times the voltage expected for a single

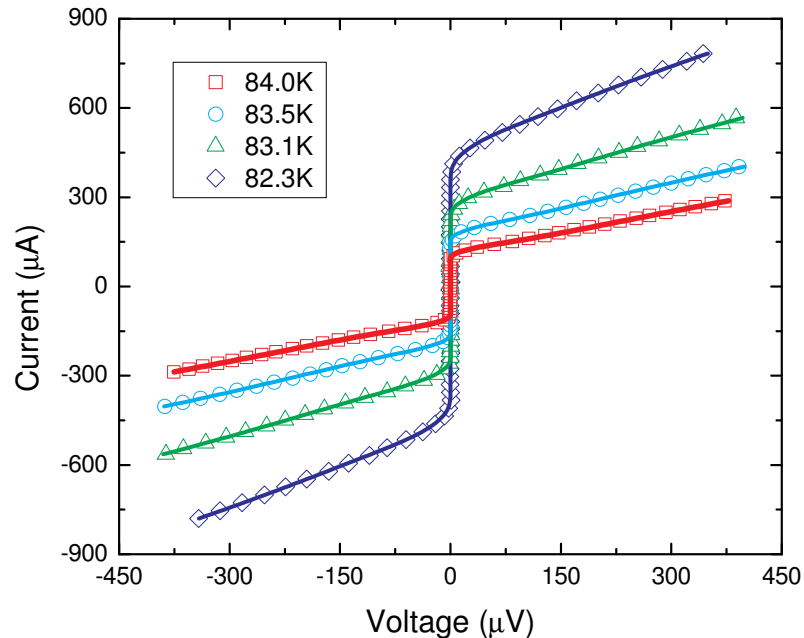


Figure 5.21: $I-V$ characteristics for 4 temperatures for sample C, fit with a modified RSJ model.

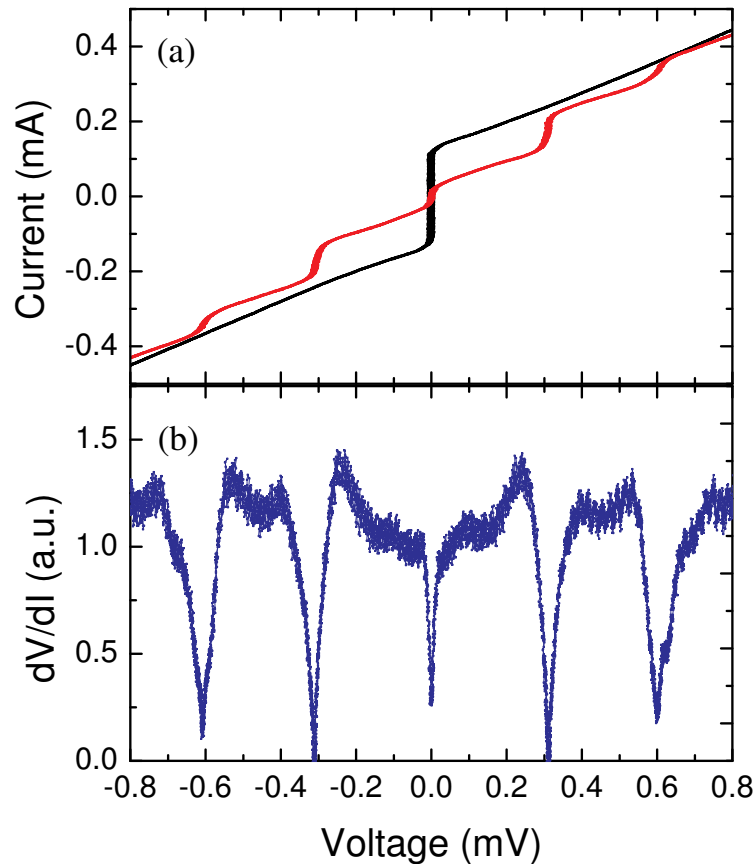


Figure 5.22: Ten junction array I - V characteristics measured at 77.4 K, with and without 15 GHz microwave radiation (a). Shapiro steps are visible at 0.31 mV, 10 times the voltage expected for a single junction at this frequency. Differential resistance (b) measurements going to zero verify that the steps are vertical, implying all junctions are locked to the 15 GHz signal.

junction at this frequency. Differential resistance was also measured to verify that the step was the product of all of the junctions. If one junction has different parameters it will produce its step at a different bias which will have a rounding effect on the giant Shapiro step. This is unacceptable for voltage standards and waveform generators which requires the position of the giant Shapiro step to be exact.

The microwave power dependence of the critical current was also measured for sample B and is shown in Figure 5.23. It shows a Bessel-like dependence similar to single junctions however at the higher order oscillations non-uniform

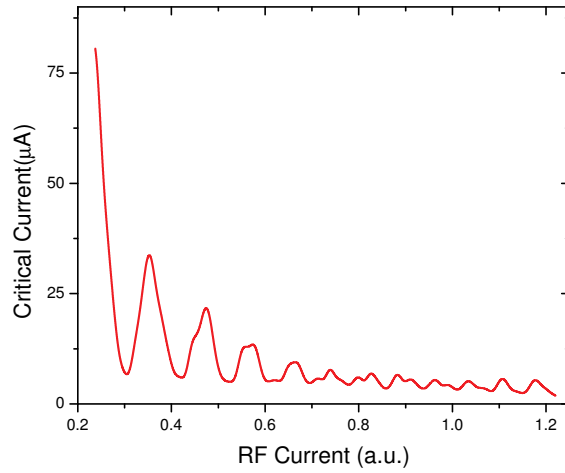


Figure 5.23: Dependence of the critical current for a ten junction array on microwave power.

critical currents of the individual junctions split the peaks.

Resistance as a function of temperature of the junctions was measured to determine the reduction in T_c from that of the bulk material. Figure 5.24 shows measurements for Samples A and C. after the bulk electrodes go superconducting ~ 85 K. The reduction in T_c is 6.5 K for the higher implantation dose in comparison

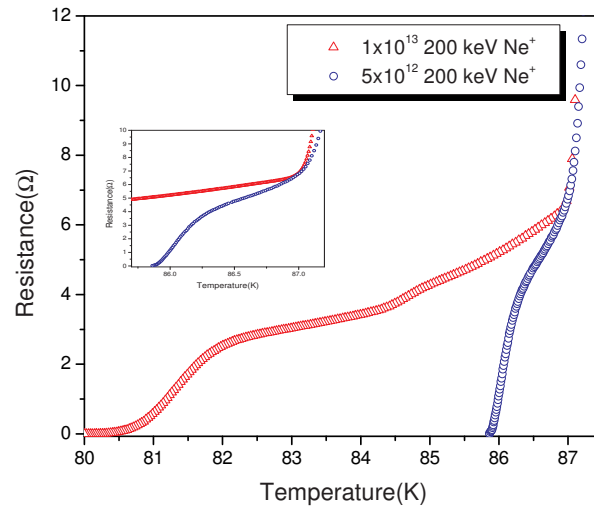


Figure 5.24: Resistance vs. temperature for samples A and C. The electrodes in both films superconduct at 87 K. The reduction in T_c is 6.5 K for the higher dose (sample A) and 1 K for the lower dose (sample C). The inset zooms in on the transition for the lower dose sample.

to 1 K for the lower. The height of the foot is higher about twice as high for sample C which is expected because the bridge width was reduced from 4 to 2 μm . The transition of sample C is smooth which indicates that T_c reduction of the material in the array is uniform, unlike sample A which shows transitions at both 84.5 and 80.5 K.

The modulation of the critical current in magnetic field was measured for all three samples and is presented in Figure 5.25 exhibiting quasi-like Fraunhofer patterns. Only half of the pattern was measured for sample C because the smaller bridge width required more field than the magnet could produce with the power supply used. The modulation period is not constant most likely due to unequal junction areas. In a non-uniform array the measured I_c is that of the junction(s)

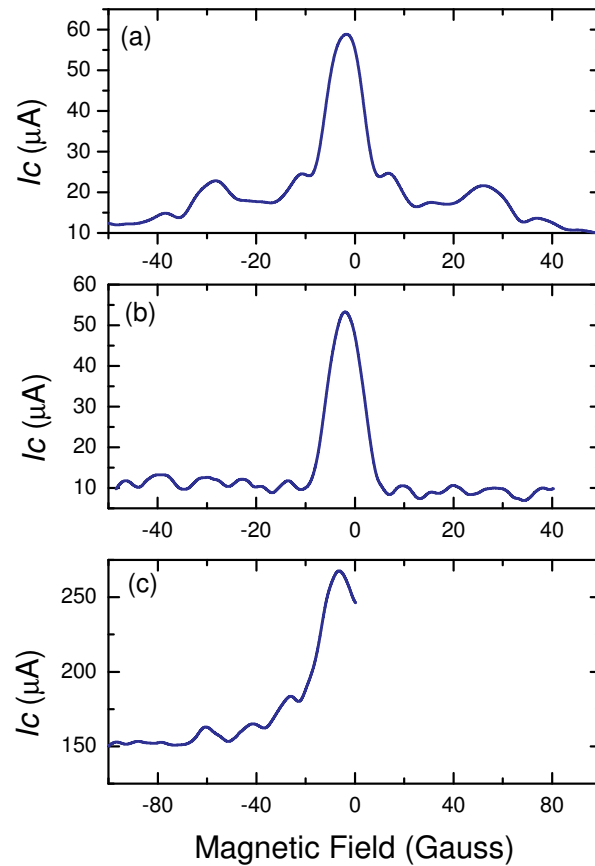


Figure 5.25: Critical current modulation in magnetic field for samples A (a) 78.0 K, B (b) 76.0 K, and C (c) 82.9 K.

with the smallest critical current. In the presence of a field the smallest critical current will be determined by the number of flux quanta penetrating the junction's area as well as its zero field value. The junction with the largest area has the shortest oscillation period as well as the smallest critical current therefore the first minima is solely due to the lowest $I_c(s)$ in the array. At higher order oscillations interferences will occur as the higher critical current junctions reach their minima. The interferences are observed in the data with the exception of sample C which appears to be very uniform. Different levels of flux trapped in between the various barriers can also play a big role in determining the shape of these patterns. Table 5.1 shows the average oscillation period of magnetic field oscillation for the three arrays of Figure 5.25 and three single junctions. The data for the single junctions includes one fabricated on sample B, the junction from Figure 5.9 and a grain boundary junction fabricated from the same material. These are compared to the three theories discussed previously. It is clear that the ion damage junctions exhibit classical junction behavior whereas the grain boundary junction closely follows the planar junction models.

Table 5.1: Comparison of ΔB (Gauss)

Sample	ΔB Actual	ΔB Classical	ΔB Rosenthal	ΔB Humphries
Array A	17.1	15.2	9.5	4.7
Array B	8.9	9.7	3.1	3.2
Array C	15.0	15.0	9.5	4.7
Single B	9.9	10.4	4.2	3.5
Single Fig. 5.9	14.9	15.6	9.5	4.7
GB Junction	3.0	8.5	3.1	2.8

Arrays containing more than ten junctions were not of sufficient uniformity to produce RSJ-like $I-V$ characteristics or flat giant Shapiro steps. Figure 5.26 shows the $I-V$ characteristics for a 50 junction array with 200 nm inter-junction spacing. Large amplitude steps are visible at $50 nhf/2e$, however, the differential resistance doesn't not reach zero. This is attributed to a variation of critical currents of the individual junctions within the array.

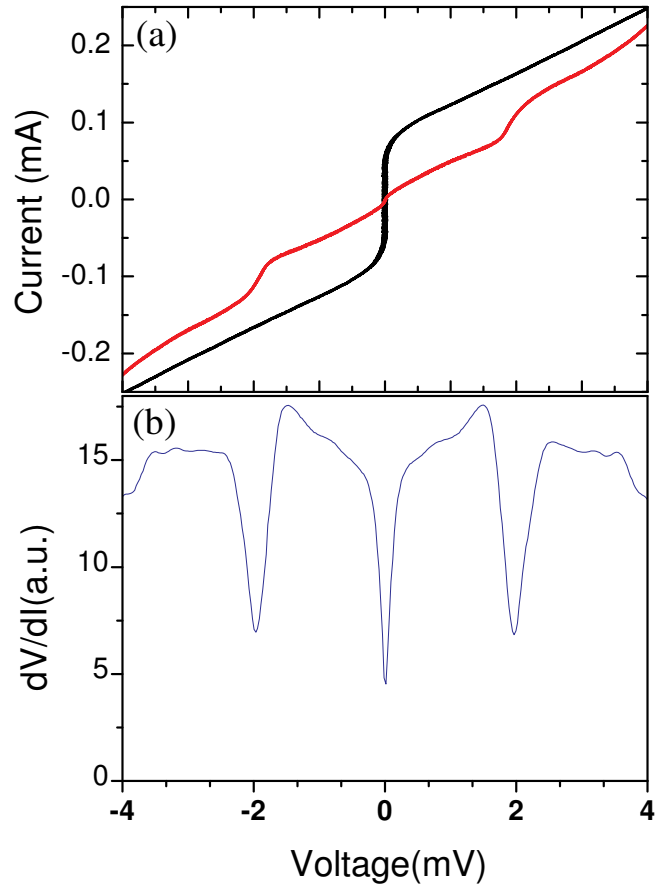


Figure 5.26: (a) $I-V$ characteristic for a 50 junction array measured at 71.8 K with and without 20 GHz microwave radiation. (b) Differential resistance measurements do not reach zero due to non-uniform junction parameters.

Reproducible series arrays of Josephson junctions for ten or less junctions exhibit RSJ-like $I-V$ characteristics and flat giant Shapiro steps indicating that the junction parameter spreads are less than 10%. The critical current of the arrays modulate in magnetic field similar to single junctions with a period that can be predicted with classical sandwich-type junction theory. Arrays of greater than 10 junctions show rounded $I-V$ characteristics and as well as rounded giant Shapiro steps, possibly limited by the EBL proximity effect.

Chapter 6

MgB₂ Josephson Junctions

The major focus of this dissertation was on YBa₂Cu₃O_{7- δ} junctions, however MgB₂ ion damage junction results by Kahler et. al. [67] served as an inspiration to extend this technology to MgB₂. The initial results from one of the first few samples was encouraging and exceeded expectations. Figure 6.1(a) shows $I - V$ measurements for a single junction measured at 37.2 K, with and without 12 GHz microwave radiation. The $I - V$ characteristics are RSJ-like with an $I_c R_n$ product of 75 μ V. Near T_c of the junction they did not exhibit the subtle rounding near I_c as observed in YBa₂Cu₃O_{7- δ} junctions. This is an indication that the rounding in YBa₂Cu₃O_{7- δ} junctions is indeed thermal rounding and less pronounced at lower temperature.

Furthermore at lower temperatures the MgB₂ junctions did not show a cross-over to flux-flow as seen in the YBa₂Cu₃O_{7- δ} junctions despite having a larger w/λ_J ratio. For the junction of Figure 6.1, $w/\lambda_J \sim 8$. This fits well in the framework of the Likharev SS'S junction model. MgB₂ has a coherence length that is 2-3 times that of YBa₂Cu₃O_{7- δ} , which implies that $L/\xi \lesssim 3.5$ for a much wider range of temperatures. Under microwave radiation Shapiro steps are visible in the $I - V$ characteristic at the expected voltages: $V = nhf/2e$ and half integer Shapiro steps appear when the junctions are measured at temperatures where I_c is greater than 0.75 mA. This may be due to magnetic flux generated from the bias or

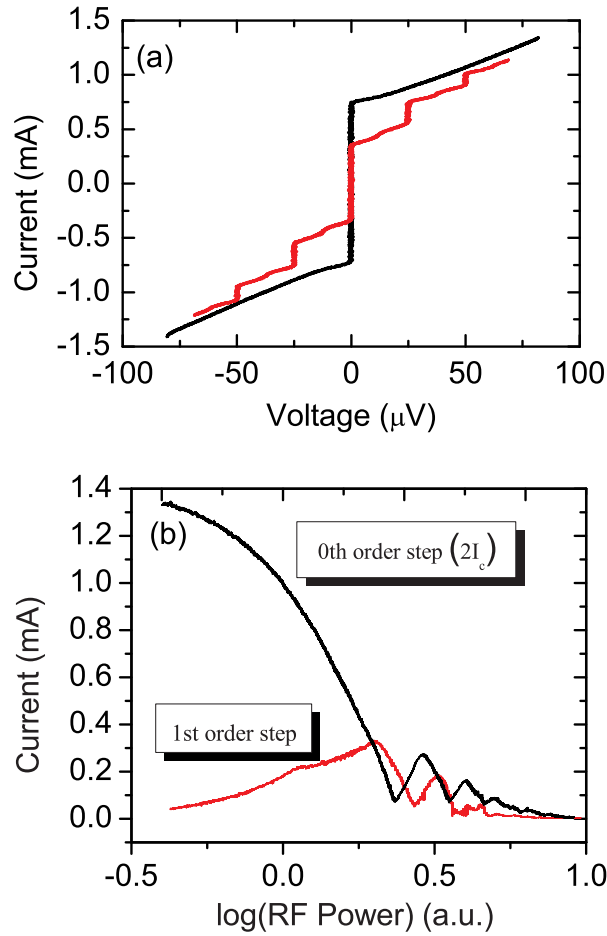


Figure 6.1: (a) $I - V$ Characteristics for a single junction measured at 37.2 K, with and without 12 GHz microwave radiation. (b) Microwave power dependence of the critical current and 1st-order Shapiro step.

from a non-sinusoidal Josephson current relation. Figure 6.1(b) shows the power dependencies of the critical current and 1st order Shapiro step. The Bessel-like dependence is a clear indication of the AC Josephson effect.

The critical current as a function of temperature was determined for a single junction by recording $I - V$ characteristics at different temperatures (Figure 6.2). Like the $\text{YBa}_2\text{Cu}_3\text{O}_{7-\delta}$ junctions these junctions have an $I_c \propto (T - T_c)^3$ near T_c and $I_c \propto (T - T_c)^2$ at lower temperatures. Resistance as a function of temperature measured using a $10 \mu\text{A}$ bias (Figure 6.2(a)) shows the T_c of the bulk material to be 38.8 K and the T_c of the weak link to be 38.2 K. This reduction in T_c ($\approx 0.6\text{K}$) is approximately one order of magnitude smaller than for $\text{YBa}_2\text{Cu}_3\text{O}_{7-\delta}$

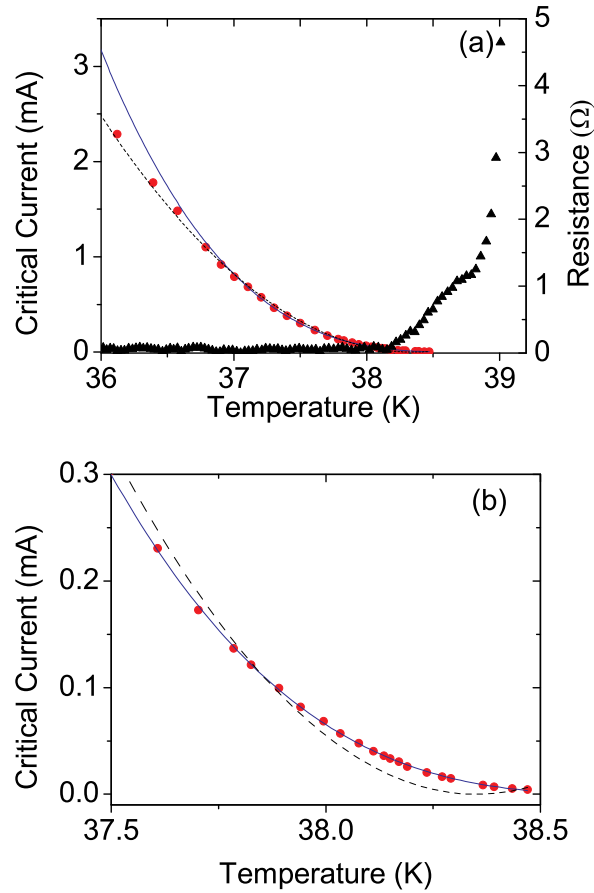


Figure 6.2: (a) Single junction critical current (circles) and resistance (triangles) temperature dependencies. The dashed and solid lines are fits with $I_c \propto (T - T_c)^2$ and $I_c \propto (T - T_c)^3$ respectively. (b) The same data shown for a temperature range near T_c

junctions ($\approx 6K$) fabricated with identical conditions. This indicates that the T_c of $\text{YBa}_2\text{Cu}_3\text{O}_{7-\delta}$ is more sensitive to 200 keV Ne+ ion damage than MgB_2 .

Figure 6.3 shows the $I-V$ characteristics for a 20 junction series array measured at 37.5 K, with and without 12 GHz microwave radiation. A flat giant Shapiro step is visible at 20 times the value of a single junction at the same frequency. This leads us to believe that the spread in $I_c R_n$ is small, however rounding near I_c suggests some spread in I_c . Differential resistance was measured under the same conditions (Figure 6.3(b)). dV/dI reaching zero confirms that the step is flat (e.g. All junctions are locked to the 12 GHz drive signal). These 20 junction results are quite encouraging considering that this is the largest array

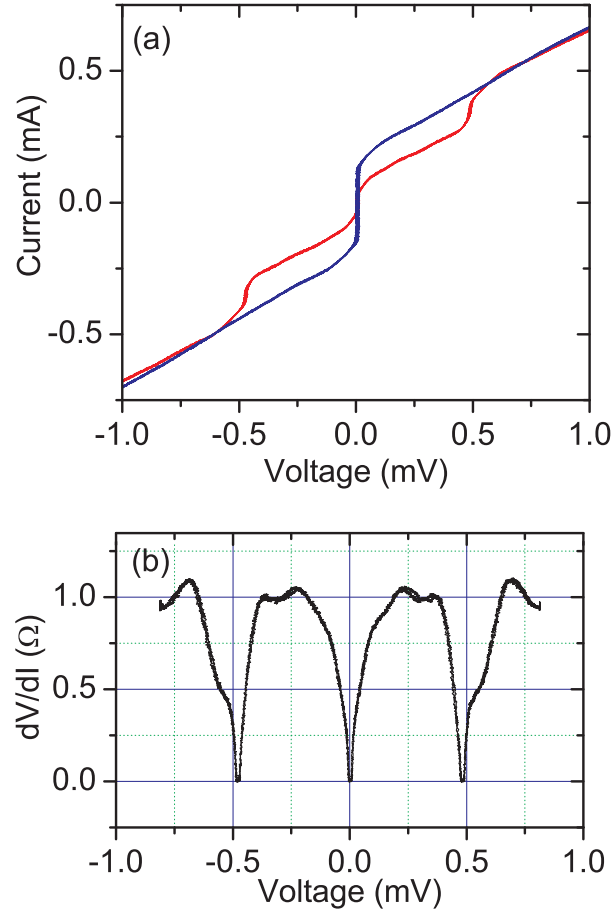


Figure 6.3: (a) $I - V$ Characteristics for a 20 junction array measured at 37.5 K, with and without 12 GHz microwave radiation. (b) Differential resistance vs. voltage measured under the same radiation.

size attempted and one of the first 4 samples fabricated using MgB_2 . It could be a combination of longer coherence length and more uniform material that makes junctions from MgB_2 easier to fabricate opposed to those of $\text{YBa}_2\text{Cu}_3\text{O}_{7-\delta}$.

MgB_2 junctions and junction arrays were fabricated that had a similar critical current dependence as those made from $\text{YBa}_2\text{Cu}_3\text{O}_{7-\delta}$, suggesting a proximity effect SN'S coupling mechanism. The lack of observing a cross-over to flux flow $I - V$ characteristics in these junctions is likely due to the larger coherence length. The quality and properties of MgB_2 make uniform junctions and arrays easier to fabricate than $\text{YBa}_2\text{Cu}_3\text{O}_{7-\delta}$.

Chapter 7

DC Washer SQUID

One of the problems with fabricating quality dc SQUIDS is increasing the Resistance so that the device can be matched to other electronics. An attempt to remedy this was to use a junction array in place of the single junctions in conventional SQUIDS. This was demonstrated using the mask shown in Figure 7.1. 10 slits are written in the implant mask across each arm of the SQUID resulting in 2, 10-junction series arrays connected in parallel. Figure 7.2(a) shows the $I-V$ characteristic for a $\text{NdBa}_2\text{Cu}_3\text{O}_{7-\delta}$ SQUID. The curve is quite rounded even near T_c , which is attributed to critical current non-uniformity. It was later found that the material used for this device was of poor quality. Despite of the non-uniformity this device still functioned as a SQUID. A voltage modulation of $10 \mu\text{V}$ was observed at a dc bias of $115 \mu\text{A}$ (Figure 7.2(b)). The period of modulation is 6.5 mGauss in comparison to the value of 5.5 mGauss calculated from the sample geometry. The 1 mGauss discrepancy is well within the error of the calibration of the magnet used.

This demonstrates a novel technique in using arrays to increase the resistance for improved matching of SQUIDS to other components.

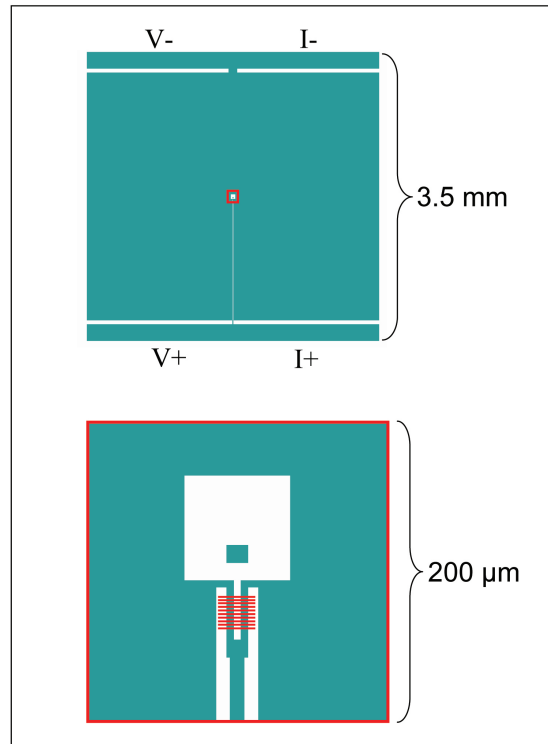


Figure 7.1: Mask used to fabricate DC washer SQUIDs. The zoomed region shows the two arms of the SQUID the lines crossing them represent the EBL defined slits in the tri-layer mask to define the junctions. The square in the hole of the washer is an alignment mark which is exposed during EBL and damaged with the junctions so that it does not superconduct.

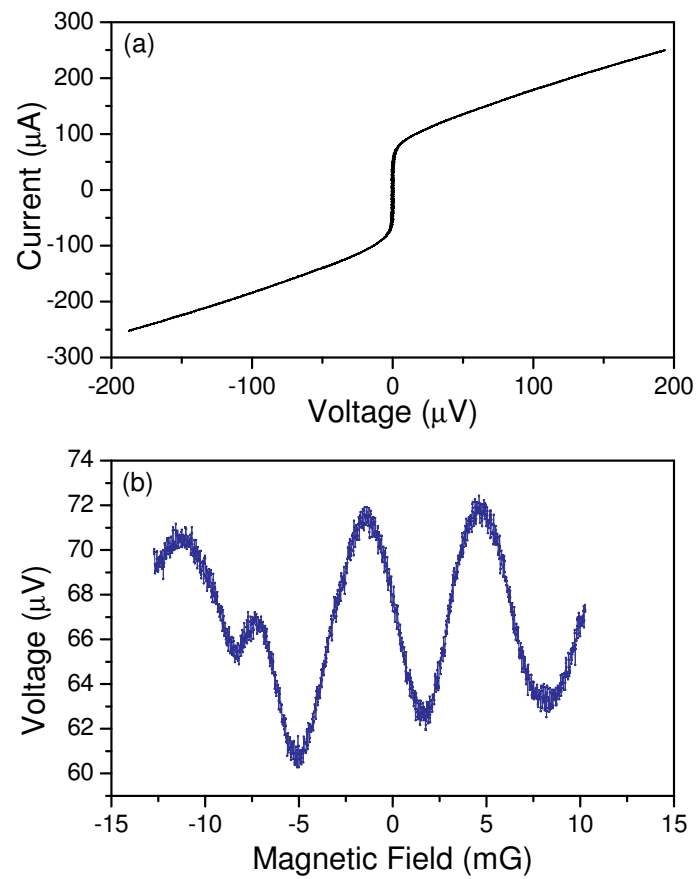


Figure 7.2: (a) I - V characteristic of a dc SQUID fabricated from two 10-junction series arrays connected in parallel. (b) Modulation of the voltage at $115 \mu A$ in magnetic field.

Chapter 8

Conclusion

In conclusion Josephson junctions fabricated from electron beam lithography and ion damage were fabricated to study their physics of operation and to improve uniformity. The uniqueness of these junctions in comparison to other types is that they are fabricated in the plane of a single film with no interfaces between different materials. This and that the barrier is a section of reduced T_c superconductor makes the physics of these junction unique. Future experiments should explore the effect the barrier length has on the flux-flow cross over as well as study the Fraunhofer patterns at low temperatures to look for evidence of a non-sinusoidal current-phase relation.

Series arrays of 10 junctions for $\text{YBa}_2\text{Cu}_3\text{O}_{7-\delta}$ and 20 for MgB_2 had uniform junction parameters and exhibited flat Shapiro steps which makes them suitable for waveform generators, oscillators and voltage standards. Further process refinements, namely EBL and the incorporation of the junctions into a co-planar waveguide could substantially increase the number of uniform junctions that can be produced.

Future work will be to incorporate these junctions into a SQIF antenna device. This device is less sensitive to parameter spreads. Successful SQIFS have been fabricated with parameter spreads as large as 30%. However SQIFs require junctions with large $I_c R_n$ products of the order of hundreds of microvolts. This will

be challenging but could be possible by increasing the film thickness, decreasing the slit size in the mask, increasing the damage, and optimizing the anneal.

As the size and price of cryo-coolers gets smaller in the years to come there will be a growing demand for an HTS Josephson technology from the defense, communications and medical industries. Although this technology currently can not provide large $I_c R_n$ products at this time, it has many advantages over competing technologies. With a few innovations in materials and/or lithography, ion damage Josephson junctions may be able to meet this demand.

Bibliography

- [1] B.D. Josephson, Phys. Lett. **1**, 251 (1962).
- [2] B.D. Josephson, Adv. Phys. **14**, 419 (1964).
- [3] B.D. Josephson, Rev. Mod. Phys **36**, 216 (1964).
- [4] P. W. Anderson and J. M. Rowell, Phys. Rev. Lett. **10**, 230 (1963).
- [5] R. C. Jaklevic, J. Lambe, A. H. Silver, and J. E. Mercereau, Phys. Rev. Lett. **7**, 159 (1964).
- [6] C. A. Hamilton, C. J. Burroughs, and S. P. Benz, IEEE. Trans. Appl. Supercond. **7**, 3756 (1997).
- [7] K. Likharev and V. Semonov, IEEE. Trans. Appl. Supercond. **1**, 3 (1991).
- [8] A. S. Katz, Ph.D. thesis, The University of California San Diego, 1998.
- [9] H.K. Onnes, Akad. van Wetenschappen **14**, 113 (1911).
- [10] W. Meissner and R. Ochsenfeld, Naturwissenschaften **21**, 787 (1933).
- [11] F. London and H. London, Proc. Roy. Soc. **71** (1935).
- [12] V. L. Ginzburg and L. D. Landau, Zh. Eksperim. i Teor. Fiz. **20**, 1064 (1950).
- [13] J. Bardeen, L. N. Cooper, and J. R. Schrieffer, Phys. Rev. **108**, 1175 (1957).
- [14] M. Tinkham, *Introduction to Superconductivity*, 2nd ed. (McGraw-Hill, New York, 1996).
- [15] A. A. Abrikosov, Zh. Eksperim. i Teor. Fiz. **32**, 1442 (1957).
- [16] K.K. Likharev, *Dynamics of Josephson Junctions and Circuits* (Gordon and Breach, Amsterdam, 1996).
- [17] W. C. Stewart, Appl. Phys. Lett. **12**, 277 (1968).
- [18] D.E. McCumber, J. Appl. Phys. **39**, 3113 (1968).

- [19] S. Shapiro, Phys. Rev. Lett. **11**, 80 (1963).
- [20] T. Van Duzer and C. W. Turner, *Superconductive Devices and Circuits* (Prentice Hall, New Jersey, 1999).
- [21] Y. Taur, P. L. Richards, and F. Auracher, in *Low temperature Physics LT-13*, edited by K. D. Timmerhaus, W. J. Osullivan, and E. F. Hammel (Plenum Press, New York, 1974), pp. 276–280.
- [22] S. K. Tolpygo and M. Gurvitch, Appl. Phys. Lett. **69**, 3914 (1996).
- [23] P.G. deGennes, Rev. Mod. Phys **36**, 225 (1964).
- [24] R. Barth *et al.*, Microelectr. Eng. **30**, 407 (1996).
- [25] A. S. Katz, A. G. Sun, S. I. Woods, and R. C. Dynes, Appl. Phys. Lett. **72**, 2032 (1998).
- [26] J. Clarke, S. M. Freake, M. L. Rappaport, and T. L. Thorp, Sol. Sta. Commun. **11**, 689 (1972).
- [27] A. S. Katz, S. I. Woods, and R. C. Dynes, J. Appl. Phys. **87**, 2978 (2000).
- [28] J. Lukens, in *Superconducting Devices*, edited by S.T. Ruggeriero and D. A. Rudman (Academic Press Inc., New York, 1990).
- [29] S. P. Benz, P. D. Dresselhaus, and C. J. Burrough, IEEE. Trans. Instrum. Meas. **50**, 1513 (2001).
- [30] S. P. Benz and C. A. Hamilton, Appl. Phys. Lett. **68**, 3171 (1996).
- [31] S. P. Benz *et al.*, IEEE. Trans. Appl. Supercond. **8**, 42 (1998).
- [32] J. Oppenlander, T. Trauble, C. Haussler, and N. Schopohl, IEEE. Trans. Appl. Supercond. **11**, 1271 (2001).
- [33] G. Bednorz and K. A. Muller, Z. Phys **189** (1986).
- [34] M. K. Wu *et al.*, Phys. Rev. Lett. **58**, 908 (1987).
- [35] J. Nagamatsu *et al.*, Nature **410**, 63 (2001).
- [36] C. Buzea and T. Yamashita, Supercond. Sci. Technol. **14**, 115 (2001).
- [37] H. J. M. ter Brake and G. F. M. Wiegerinck, Cryogenics **42**, 705 (2002).
- [38] J. M. Poate, R. C. Dynes, and L. R. Testardi, Phys. Rev. Lett. **37**, 1308 (1976).
- [39] A. E. White *et al.*, Phys. Rev. B. **37**, 3755 (1988).
- [40] J. M. Valles *et al.*, Phys. Rev. B. **39**, 11599 (1989).

- [41] R. Gandikota *et al.*, Appl. Phys. Lett. **86**, 012508 (2005).
- [42] E. K. Hollmann, O. G. Vendik, A. G. Zaitsev, and B. T. Melekh, Supercond. Sci. Technol. **7**, 609 (1994).
- [43] S. C. Tidrow *et al.*, IEEE. Trans. Appl. Supercond. **7**, 1766 (1997).
- [44] Theva Dnnschichttechnik GmbH, Rote-Kreuz-Str. 8, D-85737 Ismaning Germany.
- [45] F. Baudenbacher, H. Karl, P. Berberich, and H. Kinder, J. Less Common Met. **164**, 269 (1990).
- [46] W. Prusseit, Technical report, Theva, Theva Dnnschichttechnik GmbH, Rote-Kreuz-Str. 8, D-85737 Ismaning Germany. (unpublished).
- [47] J. Du, S. K. H. Lam, and D. L. Tilbrook, Supercond. Sci. Technol. **14**, 820 (2001).
- [48] R. Gagnon, C. Lupien, and L. Taillefer, Phys. Rev. B. **50**, 3458 (1994).
- [49] Z.K. Liu, D. G. Schlom, Qi Li, and X. X. Xi, Appl. Phys. Lett. **78**, 3678 (2001).
- [50] X. Zeng *et al.*, Nat. Mater. **1**, 1 (2002).
- [51] J. Nabity, JC Nabity Lithography Systems, <http://www.jcnabity.com>.
- [52] C. Hudak, Core Systems, <http://www.coresystems.com>.
- [53] J. F. Zeigler, SRIM-2003, <http://srim.org>.
- [54] Ivan R. Chakarov, Silvaco International, Athena SSuprem4 2D Process Simulator, <http://www.silvaco.com/products/process~simulation/athena.html>.
- [55] V. Ambegaokar and B. I. Halperin, Phys. Rev. Lett. **22**, 1364 .
- [56] O. H. Olsen and M. R. Samuelsen, Phys. Rev. B. **29**, 2803 (1984).
- [57] E. E. Mitchell, C. P. Foley, K. H. Muller, and K. E. Leslie, Physica C. **321**, 219 (1999).
- [58] P. A. Rosenthal *et al.*, Appl. Phys. Lett. **59**, 3482 (1991).
- [59] R. G. Humphries and J. A. Edwards, Physica C. **210**, 42 (1993).
- [60] Nianhua Peng *et al.*, IEEE. Trans. Appl. Supercond. **13**, 889 (2003).
- [61] M. Y. Kupriyanov and F. Lukichev, Sov. J. Low Temp. Phys. **7**, 137 (1981).
- [62] Z. G. Ivanov *et al.*, Sov. J. Low Temp. Phys. **7**, 274 (1981).

- [63] J. B. Hansen and P. E. Lindelof, *Rev. Mod. Phys.* **56**, 431 (1984).
- [64] Discussion with Horst Rogalla.
- [65] Discussion with Sam Benz.
- [66] Discussion with John Talvacchio.
- [67] G. Burnell *et al.*, *Appl. Phys. Lett.* **79**, 3464 (2001).